universität
innsbruck

Implementation and Application of a Controlled-NOT Gate in a Trapped-Ion Quantum Network Node

A master's thesis submitted to the faculty of mathematics, computer science and physics, of the University of Innsbruck in partial fulfillment of the requirements for the degree of

Master of Science (MSc)

carried out at the Institute of Experimental Physics under the supervision of

Assoc. Prof. Dr. Benjamin P. Lanyon

presented by

Tabea Stroinski

April 18, 2024

Abstract

Qubit coherence time is a crucial parameter in a trapped-ion quantum network node. However, fluctuations in the energy difference between the states used to encode a qubit into an ion can be a significant source of decoherence. In order to increase the coherence time of an arbitrary single-qubit state, the state can be encoded into a decoherence-free subspace (DFS) formed by the joint states of two physical qubits, which in our case are two co-trapped ions. As a result, the coherence of the ion-qubit is passively protected from fluctuations that affect the two physical qubits equally. This master's thesis presents experimental results on the realisation of a decoherence-free quantum memory in our experimental setup. To realise the quantum memory, a controlled-NOT (CNOT) gate was required. For the implementation of the CNOT gate, the native gates in our experimental setup were extended to complete a universal set of quantum gates. Before this master's thesis, global rotations of ion-qubits within a multi-ion string and an entangling gate were already available. To complete a universal set of quantum gates, single-ion focused phase rotations were added to the native gates. The CNOT gate was then used to store and retrieve a single-qubit state from a two-qubit DFS. The process of storing and retrieving a qubit in the DFS was fully characterised by quantum process tomography for a storage time of $500\,\mathrm{ms}$, resulting in a process fidelity of $94(6)\%$. The coherence time of the qubit is enhanced by at least one order of magnitude using the DFS encoding, compared to what was previously achieved in our ion trap system.

Contents

1. Introduction

Quantum networks are crucial for the development of quantum technology, providing powerful applications such as distributed computing [1], secure communication through quantum cryptography [2], and high-precision sensing [3]. H. J. Kimble proposed one of the most cited models for a quantum network in 2009, which introduced the concept of the quantum internet [4]. A mature quantum network, spanning cities or even countries, is similar to a classical network in which computational tasks can be performed locally and information is shared across the network. In a quantum network, local matter-based quantum network nodes are used to generate, process and store quantum information. Quantum network nodes are connected by quantum channels with the capability to faithfully transmit qubit states across the network and to establish entanglement between remote locations, requiring the ability to convert stationary qubits to travelling, or often called flying, qubits [5].

Trapped-ions are, among various other quantum platforms such as nitrogen-vacancy (NV) centres [6] or neutral atoms [7], promising candidates for realising quantum networks. Trapped-ions provide long coherence times on the order of milliseconds to seconds [8], precise qubit control [9], and high fidelity quantum gates on registers of tens of ions [10], facilitated by stable lasers. In addition, trapped-ions are especially suitable for quantum network applications since they provide an efficient interface between ion-qubits (stationary qubits) [11, 12] and travelling photons (flying qubits). Notably, recent publications have demonstrated the entanglement of a single ion with a photon converted to the telecom wavelength over a distance of 50 km [13]. Additionally, remote entanglement of ions has been demonstrated over various distances, ranging from one meter [14] to several hundred metres [15]. Protecting the ionic quantum state from decoherence while photons traverse the network necessitates robust quantum memory implementations. Trapped-ion systems offer various approaches to realise a quantum memory. For instance, radio frequency spin-echos can be used to mitigate decoherence [16], or a single-qubit state can be encoded in a decoherence-free subspace formed by entangled states of co-trapped ion [17].

This master's thesis addresses two critical aspects of a quantum network. First, in a mature quantum network it is envisioned that each quantum network node itself should be a universal quantum processor which would allow for the linking of network nodes to scale up to larger quantum processors in a modular way [1]. Secondly, this work focuses on the realisation of a long-lived quantum memory, as quantum memory storage time is a crucial parameter for enhancing the distance of entanglement distribution across the network.

The first goal of this master's thesis is to complete a universal quantum logic gate set [18] in our trapped-ion quantum network node by enabling single-qubit phase rotations via the AC Stark effect. To implement the single-qubit rotations, we use a 393 nm laser

that is focussed on individual ions and can be steered across the ion string in a Paul trap. The optical setup to address individual ions with 393 nm laser light was established within the master's thesis of Marco Canteri [19]. To meet the requirements of a mature quantum network, the ion trap network node must be capable of generating ion-photon entanglement and functioning as a universal quantum processor within a single experiment. In our experimental setup, we use a cavity-mediated bichromatic Raman process to generate ion-photon entanglement [20]. The Raman process requires a detuning of several hundreds of Hertz of the 393 nm laser, while the implementation of single-qubit phase rotations requires a far greater detuning such that the AC Stark effect is dominant. As a result, a new beam path was built to detune laser light at 393 nm laser by -2.6 GHz, enabling single-qubit phase rotations. The universal quantum logic gate set is now complete with the implementation of single-qubit phase rotations in addition to the existing native gates.

The second goal of this work was to realise a decoherence-free quantum memory by using a controlled-NOT (CNOT) gate. The CNOT gate is implemented using the universal gate set that was achieved in the first goal of this thesis. A qubit can be protected from decoherence by encoding it into a decoherence-free subspace (DFS) formed by entan-

gled states of two co-trapped ions. A CNOT gate is used to encode and retrieve a single-qubit state from a DFS. The ultimate goal of future experiments is to store the state of a trapped-ion entangled with a photon by encoding it in a DFS. The implementation of the CNOT gate would thus realise a quantum memory to store ion-photon entanglement.
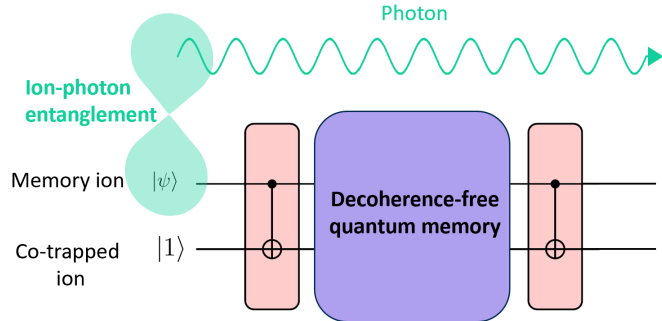
The structure of this thesis is now described. Chapter 2 covers the fundamental concepts of quantum information processing, including the characterisation of quantum states and processes, and the theoretical description of laser-ion interactions with emphasis on the AC Stark effect. The chapter concludes with an introduction to decoherence-free subspaces. Chapter 3 provides an overview of our experimental setup, the trapped-ion quantum network node, focusing on its geometry and implemented gates. Chapter 4 outlines the pre-existing setup for addressing single ions. The chapter then provides a detailed description of the optical setup built in this thesis, including its electronic control and the characterisation of two key parameters. Chapter 5 presents experimental results of the first thesis goal which is the implementation of single-qubit phase rotations via the AC Stark effect to complete a universal gate set. Chapter 6 presents the implementation and characterisation of a CNOT gate using the completed universal gate set, as well as the preparation and characterisation of single-qubit states in a decoherence-free subspace. The process of storing and retrieving a single-qubit state from a DFS is fully characterised by quantum process tomography for a storage time of 500 ms. Finally, Chapter 7 concludes with a summary and outlook for future research directions that builds upon this work.

2. Theoretical foundation

This chapter introduces basic concepts of quantum information processing and atomic physics that enable understanding the experiments presented in this thesis. Experimental studies of quantum information have become an important topic in research, and a large amount of literature has been produced as a result. Therefore, this section only focuses on the required equations for this thesis and does not provide full derivations. For details on each topic, please refer to the references inserted in the main text.

2.1. Quantum states and qubits

Single-qubit states

The fundamental unit of information in quantum information science is the quantum bit, known as the qubit [18]. The state vector of an arbitrary single-qubit state can be expressed by a linear combination of its orthonormal computational basis states $\{|0\rangle, |1\rangle\}$:

$$|\psi\rangle = \alpha |0\rangle + \beta |1\rangle, \tag{2.1}$$

where $\alpha, \beta \in \mathbb{C}$ are complex probability amplitudes satisfying the normalisation condition $|\alpha|^2 + |\beta|^2 = 1$. When measuring the qubit, it is found with a probability of $p_0 = |\alpha|^2$ in the state $|0\rangle$ and with $p_1 = |\beta|^2$ in $|1\rangle$. The normalisation condition ensures that the probabilities sum up to one. Correspondingly, an arbitrary qubit state is a unit vector in a two-dimensional complex vector space known as Hilbert space $\mathcal{H}$. In addition to expressing the qubit's state vector in the computational basis $\{|0\rangle, |1\rangle\}$, the qubit can also be defined in any other orthonormal basis. Two orthonormal bases can be identified by $\{|+\rangle, |-\rangle\}$ and $\{|+i\rangle, |-i\rangle\}$ with

$$|\pm\rangle = \frac{1}{\sqrt{2}}(|0\rangle \pm |1\rangle) \tag{2.2}$$

$$|\pm i\rangle = \frac{1}{\sqrt{2}}(|0\rangle \pm i |1\rangle). \tag{2.3}$$

The state vector of a single-qubit written in spherical coordinates

$$|\psi\rangle = e^{i\gamma}\left(\cos\left(\frac{\theta}{2}\right)|0\rangle + e^{i\phi}\sin\left(\frac{\theta}{2}\right)|1\rangle\right) \tag{2.4}$$

is defined by an angle θ and a phase ϕ. While the angle θ and the phase ϕ define the state of the qubit as a unit length vector on the Bloch sphere, the term $e^{i\gamma}$ is a *global phase* that has no influence on the physical properties of the state of the qubit. This means that for each qubit state there is an infinite class of states for $\gamma \in \mathbb{R}$ that have
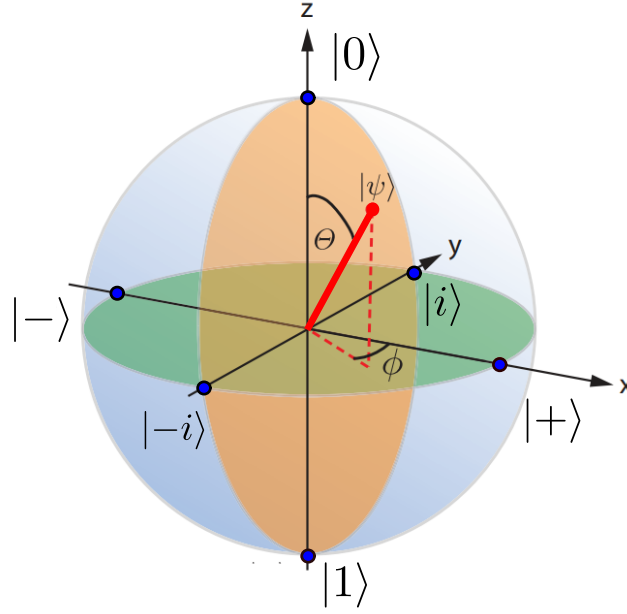
Figure 2.1.: The state vector of a pure qubit state $|\psi\rangle$ defined in Equation 2.4 in spherical coordinates is represented as a unit vector on the surface of the Bloch sphere, indicated in red. The blue dots indicate three pairs of states located at the north- and south pole $\{|0\rangle, |1\rangle\}$ and in the equatorial plane: $\{|+\rangle, |-\rangle\}$ and $\{|i\rangle, |-i\rangle\}$. Each pair forms an orthonormal basis in a two-dimensional Hilbert space $\mathcal{H}$. The figure is taken from Cornelius Hempel's thesis [21] with permission and modified in several aspects.

exactly the same physical properties. The state vector in Equation 2.4 is known as Bloch vector and can be visualised as a point on the surface of the Bloch sphere which is a three-dimensional unit sphere shown in Figure 2.1. A Bloch vector with unit length is a *pure* quantum state.

Two-qubit states

An arbitrary two-qubit state $|\psi\rangle$ in the computational basis $\{|00\rangle, \{|01\rangle, \{|10\rangle, \{|11\rangle\}$

$$|\psi\rangle = \alpha_{00} |00\rangle + \alpha_{01} |01\rangle + \alpha_{10} |10\rangle + \alpha_{11} |11\rangle \tag{2.5}$$

is defined by the complex probability amplitudes α_{ij} with $i, j = 0, 1$ and the normalisation condition $\sum_{ij} |\alpha_{ij}|^2 = 1$. The state is called a pure *product state* if it can be written as the tensor product

$$|\psi\rangle = |\psi_1\rangle \otimes |\psi_2\rangle \in \mathcal{H}_2 \otimes \mathcal{H}_2 \tag{2.6}$$

of two pure states $|\psi_i\rangle \in \mathcal{H}_i$ with $i = 1, 2$ with respective Hilbert spaces $\mathcal{H}_i$. If the state vector $|\psi\rangle$ of the composite quantum system cannot be written as a product state it is said to be *entangled*.

An example of maximally entangled two-qubit states are the Bell states [22]:

$$|\phi^+\rangle = \frac{1}{\sqrt{2}}\big(|00\rangle + |11\rangle\big) \tag{2.7}$$

$$|\phi^-\rangle = \frac{1}{\sqrt{2}}\big(|00\rangle - |11\rangle\big) \tag{2.8}$$

$$|\psi^+\rangle = \frac{1}{\sqrt{2}}\big(|01\rangle + |10\rangle\big) \tag{2.9}$$

$$|\psi^-\rangle = \frac{1}{\sqrt{2}}\big(|01\rangle - |10\rangle\big). \tag{2.10}$$

The Bell states form an orthonormal basis of the four dimensional Hilbert space. The term *maximally entangled* is defined in the following section.

Density matrix representation

A more general representation of the states of quantum bits is given by the *density matrix*

$$\rho = \sum_i p_i |\psi_i\rangle \langle\psi_i|, \tag{2.11}$$

where $\{p_i, |\psi_i\rangle\}$ is an ensemble of pure states with probabilities p_i. The density matrix ρ is a positive-semidefinite Hermitian matrix that has trace equal to one: $\mathrm{tr}(\rho) = 1$. A mixed state satisfies $\mathrm{tr}(\rho^2) < 1$, while a pure state $\rho = |\psi\rangle\langle\psi|$ can be identified by $\mathrm{tr}(\rho^2) = 1$ [18]. The density matrix can be used to calculate various quantities of interest [23] such as the time evolution $\rho(t)$ of a closed quantum system ρ

$$\rho(t) = U(t)\rho U^\dagger(t), \tag{2.12}$$

where $U(t)$ is a time dependent unitary matrix. The expectation value of an observable M is given by

$$\langle M\rangle = \mathrm{tr}(M\rho). \tag{2.13}$$

The *fidelity* F of two quantum states ρ and σ is defined as

$$F(\rho, \sigma) = \big(\mathrm{tr}\sqrt{\rho^{1/2}\sigma\rho^{1/2}}\big)^2 \tag{2.14}$$

and quantifies the overlap between the two states [24]. The fidelity F is defined on the interval $[0, 1]$, where $F = 1$ is obtained for identical states ($\rho = \sigma$) and $F = 0$ for orthogonal states.

We now consider a composite quantum system $\mathcal{H}_1 = A$ and $\mathcal{H}_2 = B$ consisting of two qubits with a joint state ρ^{AB}, then the *reduced density matrix* of the subsystem A is defined by the partial trace [18] over the subsystem B:

$$\rho^A = \mathrm{tr}_B(\rho^{AB}). \tag{2.15}$$

If the reduced density matrix ρ^A of the composite system satisfies $\mathrm{tr}_B(\rho^{AB}) = \mathbb{1}_2/2$, where $\mathbb{1}_2$ is the single-qubit identity matrix, the reduced state is called *maximally mixed*. A state is considered maximally entangled if its reduced density matrix is maximally mixed [25].

2.2. Quantum gates

Quantum gates are fundamental building blocks of quantum circuits enabling quantum computation. A quantum gate U is an unitary transformation $(UU^\dagger = \mathbb{1})$ that maps an input state ρ to an output state ρ', such that

$$\rho' = U\rho U^\dagger. \tag{2.16}$$

A set of quantum gates is considered universal if any unitary evolution of a quantum system can be decomposed into a finite concatenation of quantum gates from the set. It has been proven that a universal (quantum) gate set can be established by combining single-qubit gates, that enable arbitrary rotations of single-qubit states, with a two-qubit entangling gate [5].

Single- and multiple-qubit gates

Gates that manipulate the state of a single-qubit are defined by 2×2 unitary matrices. Considering the Bloch vector representation of a single-qubit $|\psi\rangle$, rotations of the Bloch vector around the axes $\{x, y, z\}$ are defined by the Pauli matrices

$$\sigma_x = \begin{pmatrix} 0 & 1 \\ 1 & 0 \end{pmatrix}, \quad \sigma_y = \begin{pmatrix} 0 & -i \\ i & 0 \end{pmatrix}, \quad \sigma_z = \begin{pmatrix} 1 & 0 \\ 0 & -1 \end{pmatrix}. \tag{2.17}$$

Rotations in the x-y-plane of the Bloch sphere around an axis ϕ by an angle θ are defined by

$$R(\theta, \phi) = \begin{pmatrix} \cos\left(\frac{\theta}{2}\right) & -ie^{-i\phi}\sin\left(\frac{\theta}{2}\right) \\ -ie^{i\phi}\sin\left(\frac{\theta}{2}\right) & \cos\left(\frac{\theta}{2}\right) \end{pmatrix}. \tag{2.18}$$

Rotations around the x- and the y- axis are defined by setting the phase ϕ, yielding

$$R_x(\theta) = R(\theta, \phi = 0) \tag{2.19}$$
$$R_y(\theta) = R(\theta, \phi = \pi/2). \tag{2.20}$$

Rotations around the z-axis by an angle θ can be written as

$$R_z(\theta) = \begin{pmatrix} e^{-i\frac{\theta}{2}} & 0 \\ 0 & e^{i\frac{\theta}{2}} \end{pmatrix}. \tag{2.21}$$

According to Euler's rotation theorem [26], any arbitrary single-qubit rotation can be decomposed into a maximum of three quantum gates of the form $R(\theta, \phi)$ and $R_z(\theta)$.

Two-qubit entangling gates

The controlled-NOT gate, referred to as the CNOT gate, is a two-qubit entangling gate. The gate operation flips the logical state of the target qubit if the control qubit is in

the state $|1\rangle$. The matrix representation of the CNOT gate in the computational basis $\{|00\rangle, |01\rangle, |10\rangle, |11\rangle\}$ is given by

$$U_{\text{CNOT}} = \begin{pmatrix} 1 & 0 & 0 & 0 \\ 0 & 1 & 0 & 0 \\ 0 & 0 & 0 & 1 \\ 0 & 0 & 1 & 0 \end{pmatrix}. \tag{2.22}$$

The CNOT gate applied to an unknown qubit state $|\psi\rangle = \alpha |0\rangle + \beta |1\rangle$ as control qubit and the target qubit in state $|1\rangle$ prepares the entangled state

$$|\psi'\rangle = U_{\text{CNOT}} (|\psi\rangle \otimes |1\rangle) = \alpha |01\rangle + \beta |10\rangle. \tag{2.23}$$

In quantum computation with trapped-ions, the CNOT gate can be implemented using a Mølmer-Sørenson gate [27], known as an MS gate, combined with single-qubit rotations. Section 3.3 provides details on the implementation of the MS gate using trapped-ions, while Section 6.1.1 presents the implementation of the CNOT gate using an MS gate.

2.3. Characterisation of quantum states and processes

Quantum states and quantum processes [18] can be fully characterised by tomography. This section presents a conceptual description of quantum state tomography and quantum process tomography.

Quantum state tomography

Any quantum state is fully determined by its density matrix ρ. *Quantum state tomography* (QST) is a powerful tool in quantum information science that allows to estimate the density matrix of a quantum state from a series of measurements in different bases. A single-qubit density matrix is defined by a 2×2 complex Hermitian matrix. The Pauli operators $\{\sigma_x, \sigma_y, \sigma_z\}$ together with the identity $\sigma_0 = \mathbb{1}_2$ form an orthonormal basis $(\text{tr}(\sigma_i \sigma_j) = \delta_{ij})$, further known as Pauli operator basis $\tilde{P} = \{\sigma_0, \sigma_x, \sigma_y, \sigma_z\}$, for a two-dimensional complex vector space containing all Hermitian 2×2 matrices. Any single-qubit density matrix ρ can therefore be represented by a linear combination of the elements of the Pauli operator basis, yielding

$$\rho = \frac{1}{2} p_\mu \tilde{P}_\mu, \tag{2.24}$$

$$= \frac{\text{tr}(\rho)\sigma_0 + \text{tr}(\sigma_x \rho)\sigma_x + \text{tr}(\sigma_y \rho)\sigma_y + + \text{tr}(\sigma_z \rho)\sigma_z}{2} \tag{2.25}$$

with $\mu \in \{0, x, y, z\}$ and the expectation values $p_\mu = \text{tr}\left(\tilde{P}_\mu \rho\right)$. The expectation value $p_0 = \text{tr}(\sigma_0 \rho) = \text{tr}(\rho)$ equals one by definition of the density matrix. The density matrix can be reconstructed from measuring the three expectation values: p_x, p_y and p_z. To determine each expectation value, projective measurements [18] are performed in the respective Pauli basis. These measurements are repeated for n copies of the quantum state under consideration. The expectation value is given by the statistical average of

the measurement outcomes and can be determined with high confidence for large sample size.

The approach of determining the density matrix ρ of a single-qubit state defined in Equation 2.24 can be extended to a two-qubit system. A two-qubit state is defined by a 4×4 density matrix. An orthonormal operator basis to represent the density matrix, referred to as the two-qubit Pauli operator basis [28], can be found by the tensor product

$$\tilde{P}_{\mu\nu} = \{\sigma_\mu \otimes \sigma_\nu\}, \tag{2.26}$$

with $\mu, \nu \in \{0, x, y, z\}$ such that a two-qubit density matrix is defined as

$$\rho = \frac{1}{4} p_{\mu\nu} \tilde{P}_{\mu\nu} \tag{2.27}$$

$$= \frac{\mathrm{tr}\left(\rho \tilde{P}_{\mu\nu}\right) \tilde{P}_{\mu\nu}}{4}. \tag{2.28}$$

Taking into account three different measurement bases $\{\sigma_x, \sigma_y, \sigma_z\}$ per qubit, for a two-qubit state ($n = 2$), there are $3^n = 9$ measurement bases required to reconstruct the density matrix. As an example, Figure 2.2 shows the absolute values of the density matrix $\rho = |\psi^+\rangle \langle\psi^+|$ of the entangled Bell state $|\psi^+\rangle$ defined in Equation 2.9.

It can be identified if a reconstructed two-qubit state ρ is entangled by calculating the *concurrence* [29]

$$C(\rho) = \max(0, \lambda_1 - \lambda_2 - \lambda_3 - \lambda_4), \tag{2.29}$$

where $\lambda_1, .., \lambda_4$ are the eigenvalues of the Hermitian matrix

$$R = \sqrt{\sqrt{\rho} \tilde{\rho} \sqrt{\rho}}, \tag{2.30}$$

with the spin-flipped state $\tilde{\rho} = (\sigma_y \otimes \sigma_y)\rho^\star(\sigma_y \otimes \sigma_y)$, where $\rho^\star$ is the the complex conjugate of ρ. The concurrence is zero for product states, and it reaches its maximum value when the state under consideration is maximally entangled, such as the Bell states. The concurrence is invariant under local unitary transformations. If the concurrence is larger than zero ($C > 0$) the state is entangled.

Quantum process tomography

Quantum process tomography (QPT) is used to characterise quantum processes. A quantum process can describe the evolution of both closed (unitary evolution) and open quantum systems. This thesis exclusively discusses QPT of quantum gates [18, 30]. The evolution of a quantum state ρ under a quantum process is described in quantum mechanics by a completely trace-preserving linear map ϵ acting on the state space of the density matrix [31]

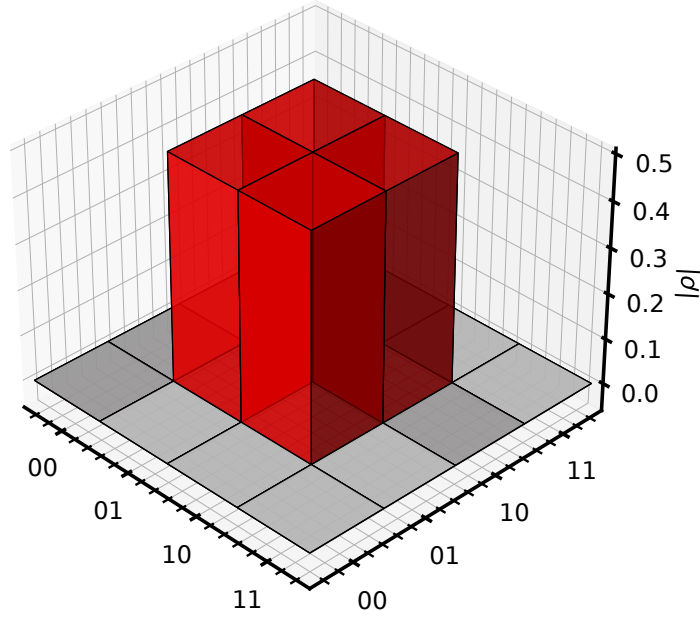$$\rho' = \epsilon(\rho), \tag{2.31}$$

Figure 2.2.: Absolute values of the density matrix $\rho = |\psi^+\rangle \langle \psi^+|$. The state $|\psi^+\rangle$ is defined in Equation 2.9. The imaginary parts of the density matrix are zero.

where ρ' is the output state of the quantum process. The quantum process $\epsilon(\rho)$ can be expressed in the so-called *operator-sum representation*

$$\epsilon(\rho) = \sum_i A_i \rho A_i^\dagger, \qquad (2.32)$$

where A_i are Kraus-operators [32] on the state space of ρ [33]. When considering a quantum process acting on a multiple-qubit system, it is useful to rewrite the Kraus-operators A_i in the Pauli operator basis $\tilde{P}$ [18], such that

$$\epsilon(\rho) = \sum_{mn} \tilde{P}_m \rho \tilde{P}_n^\dagger \chi_{mn}, \qquad (2.33)$$

where χ_{mn} are the elements of the χ-matrix or so-called process matrix that uniquely defines the quantum process under consideration. The process matrix χ can be determined experimentally from tomographic measurements. Tomographic measurements involve feeding a range of linearly independent input states to the quantum process, and then measuring each output state in different bases, equivalent to quantum state tomography.

To perform QPT for an n-qubit process acting on a state ρ with dimension $d = 2^n$, a number of d^2 linearly independent input states $\{\rho_k\}$ with $k = 0, 1, .., d^2$ must be fed into the process. The output states after the process $\{\epsilon(\rho_k)\}$ are measured to calculate the process matrix χ [33]. This means that to perform QPT for a single-qubit process, $d^2 = (2^{n=1})^2 = 4$ input states have to be prepared and measured after the process. For a two-qubit process, $d^2 = (2^{n=2})^2 = 16$ input states are required. Quantum process tomography may lead to unphysical results of the process matrix. Maximum likelihood estimation (MLE) is a common approach to ensure physically meaningful results. MLE is
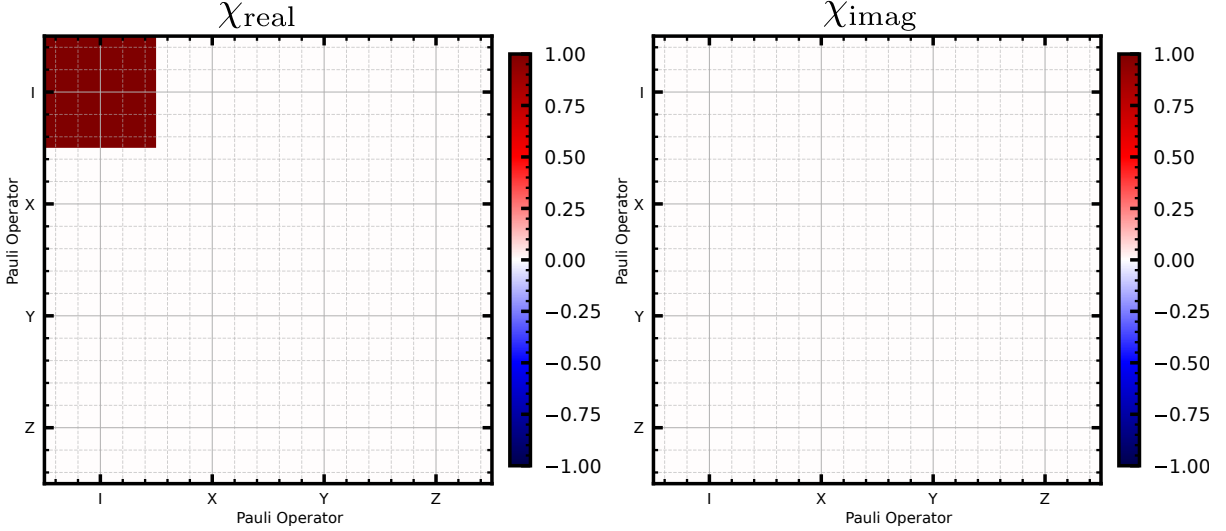
Figure 2.3.: Real (left) and imaginary (right) parts of the process matrix χ of a single-qubit identity process: $\rho' = \epsilon(\rho) = \rho$, in the Pauli operator basis.

also used for quantum state tomography [34]. MLE involves defining a likelihood function that quantifies the probability of obtaining the measured outcomes, given a particular guess for the process matrix χ of a quantum process (or density matrix for QST). The MLE algorithm then optimises the parameters of the process matrix to maximise the likelihood function. This results in the algorithm effectively finding the process matrix that best fits the observed data.

The process fidelity

$$F_p = \text{tr}(\chi_{\text{exp}}\chi_{\text{ideal}}) \tag{2.34}$$

is calculated from the experimentally determined process matrix χ_{exp} and its ideal χ_{ideal}. The process fidelity is directly related to the average gate fidelity. The average gate fidelity $\bar{F}$ is defined as the average state fidelity of the $N = d^2$ output states after the quantum process. The average gate fidelity can be calculated from tomographic data taken during QPT. The density matrices of the output states are reconstructed from the tomographic data to calculate the state fidelity F_i of each output state. The average gate fidelity is then calculated as the average:

$$\bar{F} = \frac{1}{N}\sum_{i=1}^{N} F_i. \tag{2.35}$$

The relation between the process fidelity F_p and the average gate fidelity $\bar{F}$ [35] is given by

$$\bar{F} = \frac{dF_p + 1}{d + 1} \tag{2.36}$$

Figure 2.3 shows the process matrix χ of an identity process as an example.

2.4. Two-level atom interacting with a laser beam

In quantum information processing with trapped-ions, quantum gates are typically implemented by laser pulses applied to the ions. The laser pulses coherently drive transitions between the internal states of the ions. Precise control of the laser frequency, phase and pulse duration enables the implementation of various single- and multiple-qubit gates. The interaction of a bare two-level atom defined by the states $|g\rangle$ (ground state) and $|e\rangle$ (excited state), where $|g\rangle$ and $|e\rangle$ are both eigenstates of the Pauli operator σ_z, with a laser beam coherently changes the excitation probability of $|e\rangle$. The energy

$$H_a = \frac{\hbar\omega_0}{2}\sigma_z \tag{2.37}$$

of the two-level atom is defined by the energy difference $\hbar\omega_0$ between $|g\rangle$ and $|e\rangle$. The perturbation of the two-level system by a laser beam with electrical field $E = E_0 \cos(\omega_l t + \phi_l)$, where ω_l is the laser frequency, close to the resonance frequency ω_0 and ϕ_l is the laser phase, can be described by the Hamiltonian

$$H_l = \hbar\Omega\sigma_x \cos(\omega_l t + \phi_l), \tag{2.38}$$

where Ω is the Rabi frequency. The interaction of the oscillating electrical field of the laser beam with the two-level atom can coherently drive oscillations between the probability amplitudes of the ground- and the excited state at the Rabi frequency Ω. A transformation to an interaction picture and a rotating wave approximation yields the Hamiltonian

$$H_{\text{int}} = \frac{\hbar\Omega}{2}\big(e^{-i(\Delta t + \phi_l)}\sigma_+ + e^{i(\Delta t + \phi_l)}\sigma_-\big), \tag{2.39}$$

where $\Delta = \omega_l - \omega_0$ is the detuning of the laser frequency from the atomic transition.
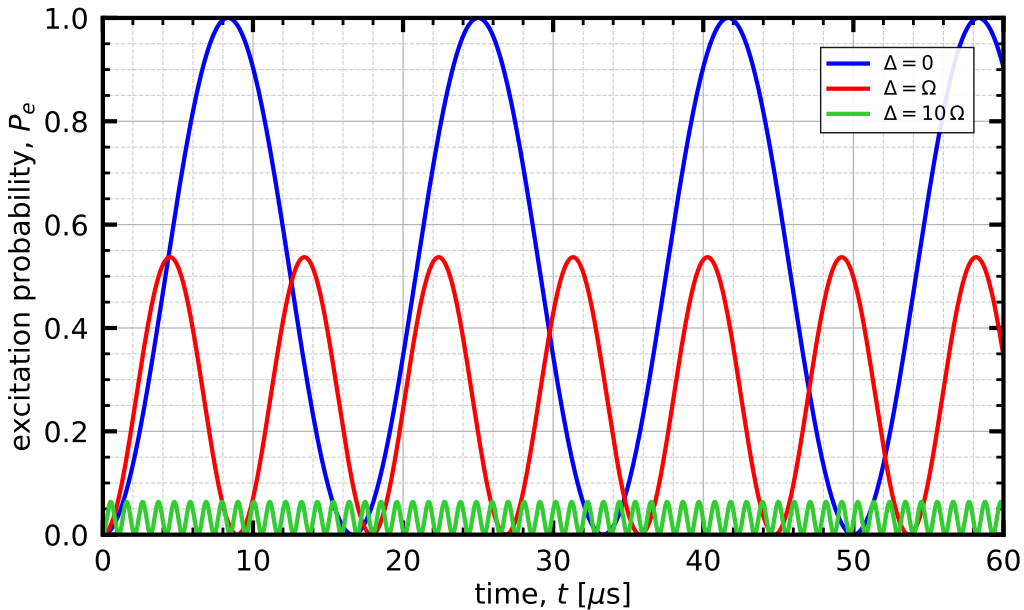

Figure 2.4.: Rabi oscillations for $\Omega = 2\pi \times 60\,\text{kHz}$ of a two-level atom interacting with a resonant laser field $\Delta = 0$ (blue) and an off-resonant laser field for two different detunings $\Delta = \Omega$ (red) and $\Delta = 10\,\Omega$ (green).

Resonant laser field $\Delta = 0$

If the detuning of the laser field is zero: $\Delta = 0$, the unitary evolution of the two-level system

$$U(t) = e^{-i\frac{H_{\text{int}}t}{\hbar}} == \begin{pmatrix} \cos\left(\frac{\Omega t}{2}\right) & -ie^{-i\phi_l}\sin\left(\frac{\Omega t}{2}\right) \\ -ie^{i\phi_l}\sin\left(\frac{\Omega t}{2}\right) & \cos\left(\frac{\Omega t}{2}\right) \end{pmatrix} \tag{2.40}$$

equals Equation 2.18 with the rotation angle $\theta = \Omega t$. Considering the states $|g\rangle$ and $|e\rangle$ of the atom as the computational basis states of a qubit, laser pulses that are resonant with the qubit transition can be used to manipulate the qubit state by rotations in the x-y-plane of the Bloch sphere.

Off-resonant laser field $\Delta \neq 0$

The excitation probability $P_e(t)$ of an atom initially in the ground state after an interaction time t with an off-resonant laser is given by

$$P_e(t) = 1 - |\langle\psi(t)|g\rangle|^2 = \frac{\Omega^2}{\Omega'^2}\sin^2\left(\frac{\Omega't}{2}\right), \tag{2.41}$$

where the effective Rabi frequency is defined as $\Omega' = \sqrt{\Omega^2 + \Delta^2}$. For increasing detuning Δ, the effective Rabi frequency Ω' increases while the oscillation amplitude Ω^2/Ω'^2 decreases, as can be seen in Figure 2.4.

Far detuned laser field $\Delta \gg \Omega$

In the limit of a large detuning $\Delta \gg \Omega$ further referred to as *far detuned* laser field, the excitation probability $P_e(t)$ defined in Equation 2.41 is largely suppressed, as can be seen in Figure 2.4 for $\Delta = 10\Omega$. The energy levels $|g\rangle$ and $|e\rangle$ are constantly shifted by δ_{AC} for the atom-laser interaction time. The energy shift δ_{AC} is known as the AC Stark shift and can be derived from second-order time-independent perturbation theory [36]. The interaction Hamiltonian in the limit of a large detuning is defined as

$$H_{\text{int}}^{\text{AC}} = -\frac{\Delta}{2}\sigma_z + \frac{\Omega}{2}\sigma_x. \tag{2.42}$$

with the eigenvalues $\lambda_\pm = \pm\frac{1}{2}\sqrt{\Delta^2 + \Omega^2}$, The AC Stark shift δ_{AC} is calculated by

$$\delta_{\text{AC}} = \lambda_\pm - \lambda_\pm(\Omega = 0) = \pm\frac{\Omega^2}{4\Delta}, \tag{2.43}$$

and induces a positive or negative shift of the energy levels depending on the sign of the detuning. The AC Stark shift δ_{AC} determines the energy shift of the two individual levels $|g\rangle$ and $|e\rangle$ as shown in Figure 2.5, such that the overall energy shift of the transition is

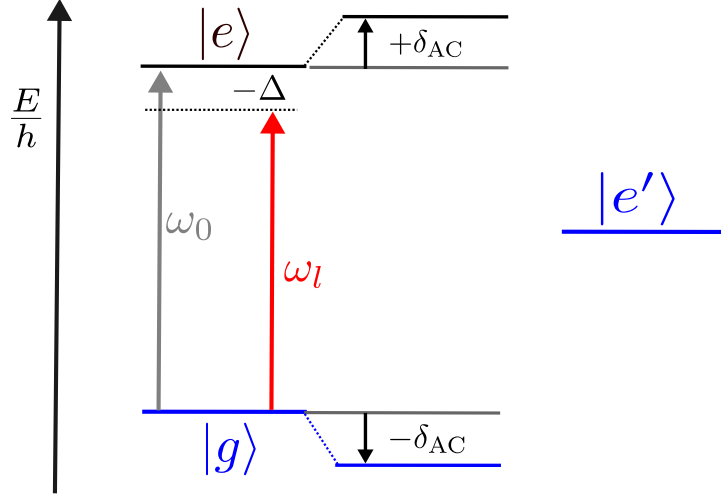$$\Delta_{\text{AC}} = -\frac{\Omega^2}{2\Delta}. \tag{2.44}$$

Figure 2.5.: Energy level shift induced by a laser with frequency ω_l and negative detuning $-\Delta$ with respect to the $|g\rangle$ to $|e\rangle$ transition frequency ω_0. The overall energy shift of the transition $|g\rangle$ to $|e\rangle$ is twice the AC Stark shift δ_{AC} as defined in Equation 2.44. The transition $|g\rangle$ to $|e'\rangle$ (blue) is shifted by half of the overall energy shift.

2.5. A two-qubit decoherence-free subspace for trapped-ions

Quantum information is always subject to decoherence as a quantum system cannot be completely decoupled from the environment. Quantum information can be protected from certain kinds of decoherence by storing it in a *decoherence-free subspace* [37, 38]. In the field of quantum information processing with trapped-ions, collective noise caused by environmental fluctuations coupled to all ion-qubits in a trap equally is a main source of decoherence. This specific type of decoherence is in this thesis referred to as *collective dephasing*. Collective dephasing is usually caused by random fluctuations of the magnetic field and laser frequency in experiments with trapped-ions [39]. The ion-qubits are usually encoded in two long-lived electronic states, so that both magnetic field and laser frequency fluctuations lead to effective fluctuations in the energy splitting of the qubit transition. Decoherence-free states are multi-particle states that are resistant to collective dephasing. Lets consider a quantum system of N qubits where fluctuations in the environment affect all qubits equally. The process of collective dephasing in such a system can be modelled by the transformation

$$|0\rangle_i \rightarrow e^{-i\frac{\phi}{2}} |0\rangle_i \tag{2.45}$$

$$|1\rangle_i \rightarrow e^{i\frac{\phi}{2}} |1\rangle_i , \tag{2.46}$$

where i is an index for qubit i and ϕ is a random phase. The transformation for each individual qubit is simply a rotation around the z-axis of the Bloch sphere given by a matrix according to Equation 2.21

$$R_z(\phi) = \begin{pmatrix} e^{-i\frac{\phi}{2}} & 0 \\ 0 & e^{i\frac{\phi}{2}} \end{pmatrix}. \tag{2.47}$$

In the case in which the phase ϕ fluctuates from shot to shot, the process leads to collective dephasing [40]. Now consider the effect of the transformations on a two-qubit system. The four computational basis states evolve as

$$|00\rangle \to e^{-i\phi} |00\rangle \tag{2.48}$$

$$|01\rangle \to |01\rangle \tag{2.49}$$

$$|10\rangle \to |10\rangle \tag{2.50}$$

$$|11\rangle \to e^{i\phi} |11\rangle \,, \tag{2.51}$$

under collective dephasing. The Bell states $|\psi^{\pm}\rangle = 1/\sqrt{2}(|01\rangle \pm |10\rangle)$ are invariant under the collective dephasing process such that the transformation has no influence on the coherence of the states. A decoherence-free subspace is spanned by the two maximally entangled Bell states $|\psi^{\pm}\rangle$ which form an orthonormal basis for a two-dimensional Hilbert space. Any superposition of $|\psi^{+}\rangle$ and $|\psi^{-}\rangle$ is invariant under the transformation in Equation 2.49 and 2.50. Hence, to protect the information encoded in a single-qubit state $\alpha |0\rangle + \beta |1\rangle$ against collective z-rotations, two physical qubits can be used. When the z-rotation applies equally to both physical qubits, the encoding $|0_L\rangle = |\psi^{+}\rangle$ and $|1_L\rangle = |\psi^{-}\rangle$ leaves the state $|\psi_L\rangle = \alpha |0_L\rangle + \beta |1_L\rangle$ invariant. The considerations show that a single-qubit encoded in a decoherence-free subspace spanned by the entangled states $|\psi^{+}\rangle$ and $|\psi^{-}\rangle$ is protected against z-rotations that are common to both physical qubits.

3. Trapped-ion quantum network node: Existing setup and key techniques

This chapter presents an overview of the experimental setup and key techniques used in the trapped-ion quantum network node employed by our research group. The quantum network node, which is based on ^{40}Ca$^+$ ions, is an existing setup that was not developed as part of this master's thesis. Details on the existing setup can be found in the dissertation by Josef Schupp [41]. Section 3.1 describes the atomic structure of ^{40}Ca$^+$, the physical implementation of the node and the laser systems used. The methods used to initialise and read out ion-qubits are described in Section 3.2. The quantum logic gate set available in the network node is presented in Section 3.3.

3.1. Cavity-integrated ^{40}Ca$^+$ ion trap network node

This section presents the components of the quantum network node. The first part of this section describes the level structure of the ^{40}Ca$^+$ ion and its use in our experiments. Various lasers used to manipulate the trapped-ions are introduced. The following section presents the geometry of the ion trap with an integrated cavity, which is used to generate ion-photon entanglement by a Raman transition.

^{40}Ca$^+$ ion and laser system

Calcium, more specifically the isotope ^{40}Ca, is an alkaline earth atom with two outer valence electrons. When ionised, one of these electrons remains and provides an atomic level scheme that is well suited for the implementation of cooling techniques and quantum gates [45]. A collimated atomic beam of various calcium isotopes is produced by resistively heating a metal tube containing naturally calcium (atomic oven) using a current of typically 3.6 A. The atomic beam travels to the centre of a linear Paul trap, where singly-charged ^{40}Ca$^+$ ions are prepared by an isotope-selective two-photon ionisation process [46] using lasers at 422 nm and 375 nm wavelengths [47].

Figure 3.1 shows the energy levels and transition wavelengths of ^{40}Ca$^+$ that are used for various purposes such as laser cooling, state initialisation and read out as well as qubit manipulation. ^{40}Ca$^+$ has a nuclear spin of zero and therefore no hyperfine structure. The total spin j is defined by the valence electron's orbital angular momentum l and the spin s. In the presence of a magnetic field, the fine structure manifolds in Figure 3.1 split up into Zeeman sub-levels, each denoted by a magnetic quantum number m_j. The external magnetic field in our experimental setup is on the order of 4.22 G [13]. In this thesis, Zeeman states are denoted as: $|n^{2s+1}l_j, m_j\rangle$, where n is the principle quantum number.
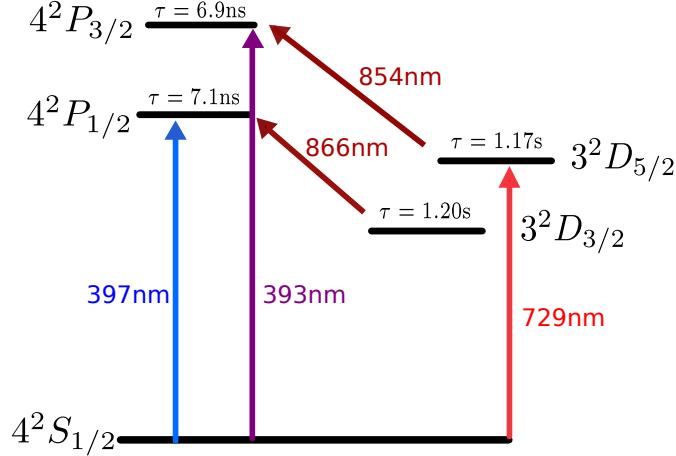
Figure 3.1.: Energy levels with lifetimes τ and transition wavelengths of a ^{40}Ca$^+$ ion that are relevant in our experiments. The numbers are taken from [42–44].

A laser at 397 nm is used for Doppler cooling the ions [48, 49] on the electric dipole transition $4^2S_{1/2}$ to $4^2P_{1/2}$. The qubit is encoded in two Zeeman states: one from the ground state manifold $4^2S_{1/2}$ and one from the metastable excited state manifold $3^2D_{5/2}$, which has a lifetime of $\tau_D = 1.168(1)$ s [43]. For experiments presented in this thesis, the usual choice for the qubit transition is $|0\rangle = |4^2S_{1/2}, m_j = -1/2\rangle$ and $|1\rangle = |3^2D_{5/2}, m_j = -5/2\rangle$. The state of the qubit is manipulated using 729 nm laser light, which couples the qubit states $|0\rangle$ and $|1\rangle$ via the electric quadrupole transition. The state of the qubit can be determined by electron shelving using 397 nm laser light. Electron shelving is explained in Section 3.2. Sideband cooling [50] on the qubit transition at 729 nm prepares the ions in the motional ground state. In the course of sideband cooling, the effective linewidth of the excited state $3^2D_{5/2}$ is artificially shortened utilising a laser at 854 nm to transfer population from $3^2D_{5/2}$ to $4^2S_{1/2}$ via the $4^2P_{3/2}$ transition [51].

In addition, a 393 nm laser, that is referred to as the *Raman laser* in our research group, is available. Laser light at 393 nm is generated from a MSquared Solstis-1600-PSX-R Ti:Sa laser with a fundamental wavelength of 786 nm. The fundamental wavelength is frequency doubled to 393 nm using a MSquared ECD-X external cavity resonant doubler accessory module. Within the master's thesis of Helene Hainzer [52], the laser was locked to an external reference cavity. As a second technique, the laser can be frequency-locked to a wavemeter, which enables frequency control at the level of a few MHz for various experimental purposes. When locked to its cavity, the linewidth was measured by a frequency beat measurement to be smaller than 100 Hz with a drift rate of 202(1) mHz/s [52]. The laser light at 393 nm is used to drive the electric dipole transition from $4^2S_{1/2}$ to $4^2P_{3/2}$. When detuned by several hundreds of MHz from the $4^2S_{1/2}$ to $4^2P_{3/2}$ resonance, the laser light is used to generate ion-photon entanglement by a bichromatic cavity-mediated Raman transition [20]. Within this thesis, few GHz detuned 393 nm laser light will be used the implement single-qubit gates via the AC Stark effect. Table 3.1 gives a schematic overview of the transition wavelengths shown in Figure 3.1 and their experimental purposes.

Name	Wavelength [nm]	Transition	Operation
397-laser	397	$4^2S_{1/2} \leftrightarrow 4^2P_{1/2}$	Doppler cooling, initialisation and read out
854-laser	854	$3^2D_{5/2} \leftrightarrow 4^2P_{3/2}$	repumping
866-laser	866	$3^2D_{3/2} \leftrightarrow 4^2P_{1/2}$	repumping
729-laser	729	$4^2S_{1/2} \leftrightarrow 3^2D_{5/2}$	qubit manipulation, sideband cooling
393(Raman)-laser	393	$4^2S_{1/2} \leftrightarrow 4^2P_{3/2}$	ion-photon entanglement generation, single-qubit gates

Table 3.1.: Laser wavelengths used in the trapped-ion quantum network node for various purposes. Lasers used for photoionisation of ^{40}Ca are not presented.

Cavity-integrated linear Paul trap

Figure 3.2 shows our ion trap system with integrated cavity, including an illustration of the geometric orientation of the lasers indicated in Table 3.1. The figure is taken from Josef Schupp's thesis [41] and edited in several aspects. A linear Paul trap employs a combination of static and radio frequency time-varying electric fields to confine charged particles in three dimensions [53]. The trap confinement is weaker in one direction (axial) than the other (radial) leading to the formation of a linear ion crystal in axial direction. The axial confinement is defined by the axial trap frequency ω_z [53]. The axial confinement in our experiments is typically given by $\omega_z = 2\pi \times 1\,\mathrm{MHz}$. In our specific configuration, the trap is vertically mounted on a sapphire holder. The ion string axis is also in the vertical direction. The trap blades are constructed from titanium and coated with gold. A near-concentric Fabry-Perot optical cavity with a spacing of $20\,\mathrm{mm}$ is integrated in the ion trap vacuum system. The cavity axis is close to being in the horizontal direction, with an angle of $85.9(1)°$ [41] between cavity axis and the string axis. The cavity is locked near-resonance to the $854\,\mathrm{nm}$ transition [52]. The cavity's vacuum field enhances photon emissions on the $854\,\mathrm{nm}$ electric dipole transition for ions positioned at anti-nodes of the vacuum cavity mode [19]. The ion trap and cavity are enclosed in a vacuum chamber shielded by a mu-metal shield to reduce magnetic field fluctuations from the environment to maintain the energy splitting between the energy levels.

The 729-laser can access the vacuum chamber from two directions, indicated as 729-ax and 729-rad in Figure 3.2, where „ax" and „rad" refer to axial and radial orientations. Both 729-laser beams couple to all trapped-ions simultaneously, which is why it is referred to as a global beam. The propagation direction of the 393-laser is indicated on the right side of Figure 3.2. Laser light at $393\,\mathrm{nm}$ is used to address individual ions within the ion string. The 393-laser is thus referred to as the addressing laser. More details about the setup to address single ions is provided in Chapter 4. The objective that is used to focus the addressing beam onto single ions is additionally used to collect the fluorescence photons from electron shelving for state read out (Section 3.2). The photons from electron shelving are imaged on a CCD camera and detected by a photomultiplier tube. Both data are available simultaneously.
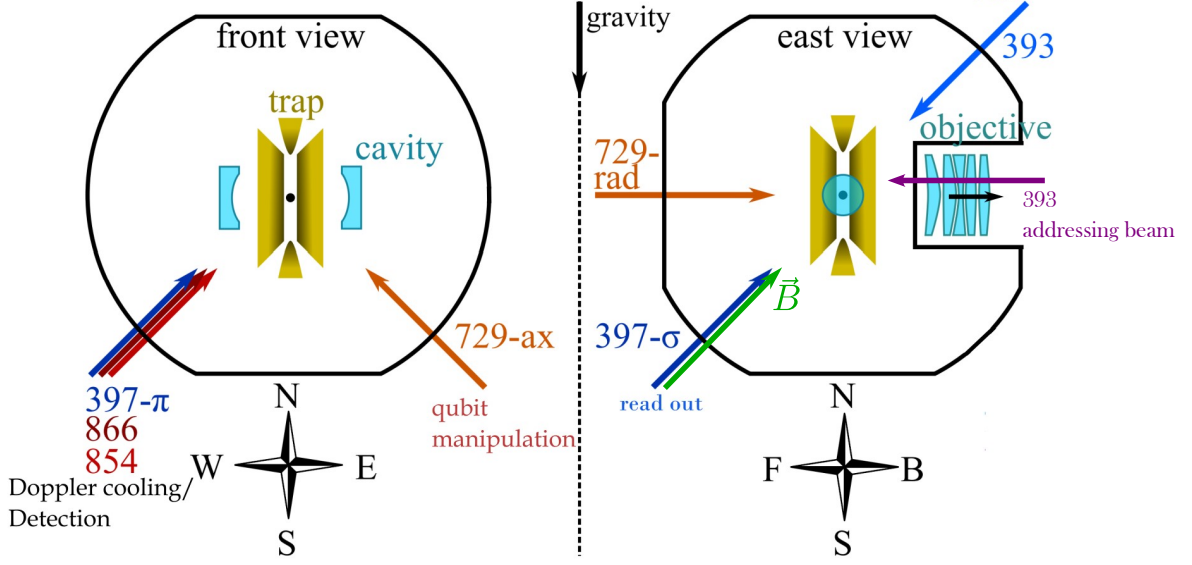
Figure 3.2.: Geometry of various lasers and the cavity-integrated linear Paul trap. The figure is taken from Josef Schupp's PhD thesis [41] with permission of the author and modified in several aspects. Left: Front view of the ion trap with a single ion in the centre. The trap is mounted vertically. The upper and lower gold-coloured electrodes are the end caps of the trap. The optical cavity is mounted with an angle of $85.9(1)°$ [41] with respect to the trap axis. The whole system is integrated into a vacuum chamber. Right: East view of the vacuum chamber. The principle magnetic field axis is shown in green. An objective is indicated that focuses the 393 nm laser to a $1/e^2$ intensity radius of $1.2(2)\,\mu$m [19] and additionally collects the fluorescence signal from electron shelving to read out the ion state as presented in Section 3.2. Both figures, left and right, show the direction of various laser beams with their corresponding polarisations.

3.2. Ion-qubit initialisation and readout

The ability to initialise qubits is a fundamental requirement for universal quantum computation [5]. In the trapped-ion quantum network node, the initialisation of qubits is based on three steps. First, the ions are Doppler cooled. Doppler cooling is performed on the $4^2S_{1/2}$ to $4^2P_{1/2}$ transition using the 397-π beam that is indicated in Figure 3.2 with repumping at 866 nm. The average phonon number $\langle n \rangle$ after Doppler cooling is about $\langle n \rangle \approx 10$ [19] at the typical axial confinement $\omega_z = 2\pi \times 1\,\text{MHz}$. Second, ion-qubits are initialised in a specific Zeeman state of the electronic ground state manifold $|4^2S_{1/2}, m_j = \pm 1/2\rangle$ by optical pumping [54]. The process is depicted in Figure 3.3. To optically pump the $^{40}\text{Ca}^+$ ions to the $|4^2S_{1/2}, m_j = -1/2\rangle$ state, a circularly polarised laser beam at 397 nm is used. The beam is shown in Figure 3.2 and is referred to as the 397-σ beam. The 397-σ beam propagates along the principle magnetic field axis $\vec{B}^1$. The polarisation of the beam is σ^-, therefore only dipole transitions

---

[1]A magnetic field of 4.22G is intentionally applied to lift the degeneracy of the Zeeman sub-levels, while magnetic field fluctuations are suppressed by the mu-metal shield.

from $|4^2S_{1/2}, m_j = +1/2\rangle$ to $|4^2P_{1/2}, m_j = -1/2\rangle$ are possible. The $4^2P_{1/2}$ manifold has a lifetime of $\tau = 7.098(20)\,\text{ns}$ [42], and the state $|4^2P_{1/2}, m_j = -1/2\rangle$ decays preferably to the ground state manifold $4^2S_{1/2}$ with a branching ratio of 93.565(7) % [55]. When the excited state $|4^2P_{1/2}, m_j = -1/2\rangle$ decays to the ground state $|4^2S_{1/2}, m_j = -1/2\rangle$, the 397-$\sigma$ beam no longer affects the state, while the population of $|4^2S_{1/2}, m_j = +1/2\rangle$ is suppressed by the continuous laser excitation. After a sufficiently long illumination time of the ions with the 397-σ beam, which is in our experiment typically a few tens of microseconds, only population in the ground state $|4^2S_{1/2}, m_j = -1/2\rangle$ is expected. The branching ratio from the $4^2P_{1/2}$ to the $3^2D_{3/2}$ manifold is not negligibly small with 6.435(7) % [55]. When using the 397-laser, the 866-laser is always used in addition to pump out or deplete the $3^2D_{3/2}$ manifold. Finally, the motional ground state[2] of the ion is prepared by sideband cooling on the qubit transition $4^2S_{1/2}$ to $3^2D_{5/2}$ using the 729-laser [51]. In our experiments, the average phonon number $\langle n \rangle$ is much smaller than one in each mode when sideband cooling is applied to all three motional modes of a single trapped-ion. A detailed description of ground state cooling can be found in [41].

The method to readout the qubit state of the ions utilised in the trapped-ion quantum network node is known as electron shelving [56, 57]. The process is depicted in Figure 3.3. The ions are illuminated with 397 nm laser light. The beam couples the $4^2S_{1/2}$ and $4^2P_{1/2}$ manifolds. Ions in the ground state manifold are excited to the short lived excited state manifold $4^2P_{1/2}$ and decay with a 93.565(7) % [55] probability back to the ground state manifold, whereby a photon is scattered at 397 nm. A fraction of the scattered photons at 397 nm are collected by a multi-lens objective (Figure 3.2) and detected by a photomultiplier tube and a CCD camera as introduced in Section 3.1. Correspondingly, ions in the ground state $4^2S_{1/2}$ appear as a bright signal on the camera. With the counter probability of 6.435(7) %, the $4^2P_{1/2}$ manifold decays to the metastable $3^2D_{3/2}$ manifold without scattering a photon at 397 nm. In order to repump the electron to the $4^2P_{1/2}$ manifold, the laser at 866 nm is used in parallel with the 397 nm laser. If the ion is in one of the excited states $3^2D_{5/2}$, it does not interact with the 397 nm laser light. In that case, the ions appear to be dark when imaged on the camera. The qubit states encoded in the $4^2S_{1/2}$ and $3^2D_{5/2}$ manifolds are correspondingly known as *bright*- and *dark*- states, respectively. If the fluorescence signal is detected with the PMT, bright and dark states are distinguished by setting a threshold for the number of detected photon counts. Individual ions within an ion string can be spatially distinguished by imaging them on the CCD camera. The probability of measuring the ion in the excited state $3^2D_{5/2}$, which is the dark state, is determined by repeating the entire experimental sequence n-times, where n is the number of cycles. The $3^2D_{5/2}$ excitation probability P_D is defined by: $P_D = m/n$, where m is the number of times dark was found. The standard deviation σ of the probability estimate P_D is given by quantum projection noise [58]:

$$\sigma(P_D) = \sqrt{\frac{P_D(1 - P_D)}{n}}. \tag{3.1}$$

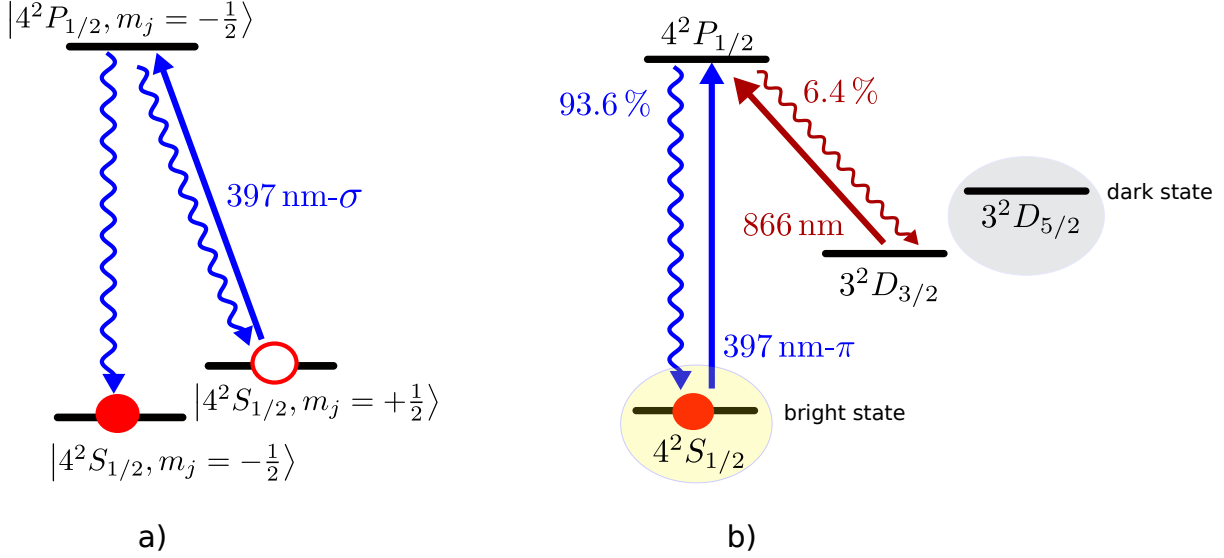[2]A single trapped-ion has three orthogonal motional states.

Figure 3.3.: a) Optical pumping to $|4^2S_{1/2}, m_j = -1/2\rangle$ using the 397-σ beam shown in Figure 3.2. An ion initially in $|4^2S_{1/2}, m_j = +1/2\rangle$ is excited to $|4^2P_{1/2}, m_j = -1/2\rangle$ via a σ^--dipole transition. The excited state decays to either $|4^2S_{1/2}, m_j = -1/2\rangle$ or $|4^2S_{1/2}, m_j = +1/2\rangle$. Population in $|4^2S_{1/2}, m_j = -1/2\rangle$ is unaffected by the laser. Population in $|4^2S_{1/2}, m_j = +1/2\rangle$ can be re-excited again and will eventually be pumped into $|4^2S_{1/2}, m_j = -1/2\rangle$. **b)** Electron shelving used to read out the state of a qubit encoded in $4^2S_{1/2}$ and $3^2D_{5/2}$. An ion initially in the ground state manifold $4^2S_{1/2}$ is excited to the $4^2P_{1/2}$ manifold using the 393-π beam shown in Figure 3.2. The ion state decays with a probability of 93.6 % back to the ground state $4^2S_{1/2}$ and scatters a photon at 397 nm. The state decays with the counter probability of 6.4 % to the $3^2D_{3/2}$ manifold. A laser at 866 nm pumps population from $3^2D_{3/2}$ back to $4^2P_{1/2}$. Scattered photos at 397 nm are collected with an objective and detected (PMT and CCD camera). Ions in the ground state appear as bright states when imaged on the CCD camera. Ions in the excited state $3^2D_{5/2}$ are not affected by the laser and are not visible on the camera image (dark state).

3.3. Native gates

This section presents the set of quantum gates implemented in our experimental setup, referred to as *native gates*. The native gates consist of global, or collective, gates that aim to manipulate the state of all individual ion-qubits of the entire ion-qubit string equally, as well as an entangling Mølmer-Sørenson gate [59], both realised using a broad-focussed 729 nm laser beam. The native gates are completed by single-qubit gates via the AC Stark effect implemented by addressing individual ions within the string with a tightly-focussed laser beam at 393 nm wavelength.

Global (729 nm) and single-qubit (393 nm) gates

The qubit, encoded in two Zeeman states $|S\rangle = |4^2S_{1/2}, m_j\rangle$ and $|D\rangle = |3^2D_{5/2}, m_j\rangle$, is manipulated by 729 nm laser pulses resonant with the qubit transition. Those gates are defined by the unitary matrix in Equation 2.40 and can be written as

$$R(\theta, \phi) = e^{-i\frac{\theta}{2}\left(\cos(\phi)\sum_j \sigma_x^j + \sin(\phi)\sum_j \sigma_y^j\right)}, \tag{3.2}$$

where $\theta = \Omega t$ is the rotation angle containing the Rabi frequency Ω of the qubit transition, ϕ is the laser phase and $\sigma^j_{\{x,y\}}$ are the respective Pauli operators on ion-qubit j. The axial- and radial 729 nm beams illuminate all ions in the trap simultaneously. Gates implemented using 729 nm laser light always apply approximately equally to all trapped-ions. The gates $R(\theta, \phi)$ are referred to as *global gates*[3] in this thesis.

Single-qubit rotations around the z-axis are implemented using the 393-addressing beam depicted in Figure 3.2. The 393 nm laser is locked to the wavemeter and the frequency is set such that it is far detuned $\Delta \gg \Omega$, as defined in Section 2.4, from the $|S\rangle$ to $|P\rangle = 4^2P_{3/2}$ transition. In the far detuned regime, the AC Stark effect is dominant. The laser-ion interaction causes a shift δ_{AC} (Equation 2.43) of the energy levels of the qubit states due to the AC Stark effect for the time t of the laser pulse. The qubit transition $|S\rangle$ to $|D\rangle$ is shifted by $|\delta_{AC}| = \Omega^2/4\Delta$ for the interaction time t, which is half the shift caused by the 393 nm laser on the $|S\rangle$ to $|P\rangle$ transition, as shown in Figure 2.5. The AC Stark shift causes a linear phase evolution of the qubit state over time, resulting in a z-rotation of the state vector on the Bloch sphere according to Equation 2.21. Single-qubit gates via the AC Stark effect can be written as

$$R_z^{(i)}(\theta) = e^{-i\frac{\theta}{2}\sigma_z^{(i)}}, \tag{3.3}$$

where $\theta = \delta_{AC}t$ is the rotation angle and $\sigma_z^{(i)}$ is the respective Pauli matrix on the addressed ion-qubit i.

Two-qubit Mølmer-Sørenson entangling gate at 729 nm

A mulit-qubit entangling gate between trapped-ion qubits sharing a common motional mode can be implemented by a Mølmer-Sørenson (MS) gate [59]. The MS gate was first investigated by K. Mølmer and A. Sørenson in 1999 [59]. A similar scheme for realising a two-qubit CNOT gate between ions was proposed even earlier by J. I. Cirac and P. Zoller [60]. The *Cirac-Zoller* CNOT gate requires the ion string to be prepared in the motional ground state [61]. The MS gate is a convenient choice for implementing entangling operations in trapped-ion information processing because it does not require the ion string to be in the motional ground state. Instead, the gate only requires the *Lamb-Dicke regime* [62], which is achieved in our trapped-ion quantum network node after Doppler cooling the ion string. The gate is used to entangle the electronic states of the ion-qubits by coupling the ions through a vibrational degree of freedom of the ion-crystal [63]. In this thesis only two-qubit entangling gates are relevant. This section provides a simplified description of the implementation of the MS gate in the trapped-ion quantum network node. For detailed theoretical and experimental descriptions of the MS gate, please refer to the cited references.

The two qubit MS gate is realised in our experimental setup by illuminating the ions with a bichromatic laser field [64] at 729 nm that couples equally to the two ion-qubits in the string. The bichromatic light field implements an effective spin-spin interaction. The two tones, ω_1 and ω_2, of the bichromatic light field are detuned by δ from the first red- and blue motional sidebands, respectively, of one motional mode of the two-ion string at

---

[3]The term global rotations or global pulses is also used.

frequency ω_m, such that

$$\omega_1 = \omega_0 - (\omega_m + \delta), \quad \text{red sideband} \tag{3.4}$$

$$\omega_2 = \omega_0 + (\omega_m + \delta), \quad \text{blue sideband}, \tag{3.5}$$

where ω_0 is the qubit transition frequency at $729\,\text{nm}$. The interaction of the bichromatic light field with a two-ion string is defined by the Hamiltonian [61]

$$H_{\text{MS}}(t) = \hbar\eta\Omega(a^\dagger e^{-i\delta t} - a e^{i\delta t})S_x, \tag{3.6}$$

where Ω is the Rabi frequency of the qubit transition, η is the Lamb-Dicke parameter describing the coupling between laser and motional mode, a and $a^\dagger$ are phonon annihilation and creation operators and $S_x = \sigma_x \otimes \mathbb{1} + \mathbb{1} \otimes \sigma_x$ is the global spin operator. The system evolves as a quantum harmonic oscillator that is off-resonantly driven by interaction with the bichromatic laser field in a way that is spin-dependent. The Hamiltonian can be analytically integrated to derive the unitary evolution induced by the interaction in Equation 3.6, yielding

$$U_{\text{MS}}(t) = D(\alpha(t)S_x)e^{-i\phi(t)S_x^2}, \tag{3.7}$$

where $\phi(t) = \left(\frac{\eta\Omega}{\delta}\right)^2(\delta t - \sin(\delta t))$ is the geometric phase and $\alpha(t) = i\frac{\Omega}{\delta}(1 - e^{i\delta t})$ is the displacement amplitude. The displacement operator D is defined as

$$D(\alpha) = e^{\alpha a^\dagger - \alpha^* a}. \tag{3.8}$$

For a gate time[4] $t_{\text{gate}} = 2\pi/\delta$ and the Rabi frequency $\Omega = \delta/(4\eta)$, the gate operation reads

$$U_{\text{MS}} = e^{-i\frac{\pi}{8}S_x^2}, \tag{3.9}$$

and prepares a maximally entangled Bell state [64].

In our group the MS gate is typically implemented on the axial centre of mass mode of the ion trap using the axial 729-beam shown in Figure 3.2. The value of the detuning δ is typically chosen to be around $10\,\text{kHz}$, plus minus a few kHz. Following the recent stabilisation of the ion trap's radial modes by Johannes Helgert as part of his master's thesis [65], the gate can now also be implemented on a radial motional mode. For experiments in this thesis, we only use the axial MS gate.

Conclusion

In conclusion, we are able to implement a two-qubit entangling gate using the MS gate at $729\,\text{nm}$, as well as arbitrary single-qubit gates that are decomposed in global rotations using $729\,\text{nm}$ laser light resonant to the qubit transition $|S\rangle$ to $|D\rangle$ and single-qubit rotations around the z-axis using $393\,\text{nm}$ laser light far detuned from the $|S\rangle$ to $|P\rangle$ transition. Those native gates form a universal gate set. While in principle, single-qubit gates via the AC Stark effect can be implemented for any detuning larger than zero,

---

[4]The displacement operator vanishes for t_{gate}.

smaller detunings increase the likelihood of exciting the $|P\rangle$ state. This can result in population of the $|P\rangle$ state decaying to various states in the calcium ions. Therefore, single-qubit gates implemented with smaller detuning result in lower gate fidelity. In the trapped-ion quantum network node, ion-photon entanglement is generated using 393 nm laser light that is detuned from the $|S\rangle$ to $|P\rangle$ transition [20]. The beam used for ion-photon entanglement generation is the only beam in the experiment that is focussed on single ions. The 393 nm addressing beam necessarily needs to be used to implement single-qubit gates. However, the detuning of about 400 MHz required for ion-photon entanglement generation is too small to implement single-qubit gates via the AC Stark effect with high fidelity due to scattering. In order to have both, a universal gate set and ion-photon entanglement generation, available in the trapped-ion quantum network node, a new beam path was built as part of this thesis to detune the 393 nm laser by a sufficiently high amount so that the AC Stark effect is dominant when single-ions are addressed with the detuned 393 nm laser light.

4. Setup and characterisation of a -2.6 GHz detuned 393 nm beam path

Section 4.1 reviews the single-ion addressing setup at 393 nm built by Marco Canteri within his master's project [19]. The addressing setup has primarily been used to generate ion-photon entanglement by a Raman process. As part of this master's thesis, a new optical setup was built to generate a 2.6 GHz detuned 393 nm laser signal. The light path was superimposed on the existing single-ion focussed beam path, making it available for addressing single ions within an ion string to realise single-qubit gates via the AC Stark effect. The realisation of single-qubit gates via the AC Stark effect completes a universal gate set in our setup together with global gates and an MS gate at 729 nm while retaining the ability to generate ion-photon entanglement. As a result, the trapped-ion quantum network node functions as a universal quantum processor with the capability to distribute entanglement over long distances.

4.1. Existing addressing setup

This section summarises the essential parts of the single-ion addressing setup built into the quantum network node. The setup was built by Marco Canteri and a detailed description can be found in his master's thesis [19]. The 393-laser is tightly focussed on the ions with a $1/e^2$ intensity radius of $1.2(2)\,\mu\text{m}$ [66]. The ion separation of two neighbouring ions in a two ion string at the typical confinement, i.e. an axial centre-of-mass frequency $\omega_z = 2\pi \times 1$ MHz, is approximately $5.7\,\mu\text{m}$. The tight focus allows to address individual ions within an ion string with negligible crosstalk. The tight focus is achieved using a multi-lens objective with a numerical aperture of 0.29. The optical axis of the objective is positioned perpendicular to the ion string axis and at a 45-degree angle to the quantisation axis which is indicated in Figure 3.2. The polarisation of the laser beam at 393 nm is linear and orientated perpendicular to the quantisation axis. The beam can be steered by an acousto-optic deflector (AOD) along the ion string on a microsecond timescale [19]. In particular, the -1st diffraction order of the AOD is used to address individual ions, which adds a detuning of -130 MHz to the light signal deflected by the AOD. The aim of this work is to establish a new beam path that detunes the 393 nm laser by -2.6 GHz and to use the existing addressing setup to address single ions with the new beam. As a result, 393 nm laser light with two significantly different detunings can be applied to individual ions in the string. The addressing setup includes several frequency shifting component: acousto-optic modulators and the AOD [19]. This results in a detuning difference of $\delta = -2.3$ GHz by adding up all frequency shifting components in the two beam paths at the position of the ion between the two addressing paths. For many experiments presented in this work, the 393 nm laser is frequency locked on a wavemeter to a detuning of -400 MHz from the

$4^2S_{1/2}$ to $4^2P_{3/2}$ transition to implement a Raman process. Accordingly, the far detuned beam is detuned by $\Delta = -2.3\,\mathrm{GHz} - 400\,\mathrm{MHz} = -2.7\,\mathrm{GHz}$.

4.2. Far detuned 393-beam setup for single-qubit gates

Section 4.2.1 describes the optical setup used to detune 393 nm laser light by -2.6 GHz. The setup design is based on a double and a single pass AOM, which are operated with RF signals at their carrier frequency. The control electronics for providing the RF signals are presented in Section 4.2.2.

4.2.1. Optical setup

Figure 4.1 shows the optical setup used to detune 393 nm laser light by -2.6 GHz. Light is taken from the output of the 393-laser and transmitted through a 10 m polarisation maintaining fibre to the optical table where the setup is located. The light is then coupled back to free space and subsequently into a 1.0(1) m large mode area photonic crystal fibre[1] (PCF). The PCF allows for higher power than standard single mode fibres without nonlinear effects or material damage, while ensuring single-mode operation [2]. A fibre collimator[3] is used to couple the light to free space from the PCF. The collimator has a focal length f of 12 mm. For the following discussion, we introduce a $1/e^2$ beam intensity diameter of the laser beam $\varnothing$. The effective numerical aperture of the PCF at 400 nm is 0.033 [68] which is expected to result in a collimated beam diameter of $\varnothing = 792\,\mu\mathrm{m}$. A diameter $\varnothing = 667(5)\,\mu\mathrm{m}$ was measured using a beam profiler.

After passing a half-wave plate[4] and a polarising beam splitter (PBS), the light goes through AOM A[5] in double pass. AOM A has a carrier frequency $f_c = 1\,\mathrm{GHz}$ which provides a detuning of -2 GHz of the -1st diffraction order in double pass configuration. The AOM's data sheet is linked in Appendix A.1. To achieve a beam diameter that does not exceed the size of the active aperture of AOM A (75 μm) and allow for full transmission of light trough the AOM, a telescope configuration of two lenses[6],lens A and B, each with focal length $f = 10\,\mathrm{cm}$, is used. The expected beam diameter at the focus of lens A is 63 μm. A measured value of $\varnothing = 69.7(6)\,\mu\mathrm{m}$ was obtained using a beam profiler. AOM A is positioned at the expected focal point 10 cm away from lens A. The alignment of AOM A is adjusted to optimise the diffraction efficiency of the -1st diffraction order. This diffraction order is chosen for optimisation as the beam is ultimately deflected by the AOD of the existing addressing setup. As stated in Section 4.1, the AOD is also optimised for the -1st diffraction order. Consequently, deflecting the far detuned 393-beam with the AOD increases the detuning by -130 MHz. If we had selected the +1st

---

[1] NKT Photonics, LMA-PM-10-UV

[2] To reduce fibre losses in future experiments, we plan to move the setup closer to the 393-laser table. We want to use a single short PCF to pick off the light from the laser that is sent to the setup, instead of using two fibres (one polarisation-maintaining and one photonic crystal fibre).

[3] Schäfer+Kirschhoff [67], 60FC-M12-33

[4] All wave plates used in the setup are from the company CeNing Optics.

[5] Brimrose, TEF-1000-300-393
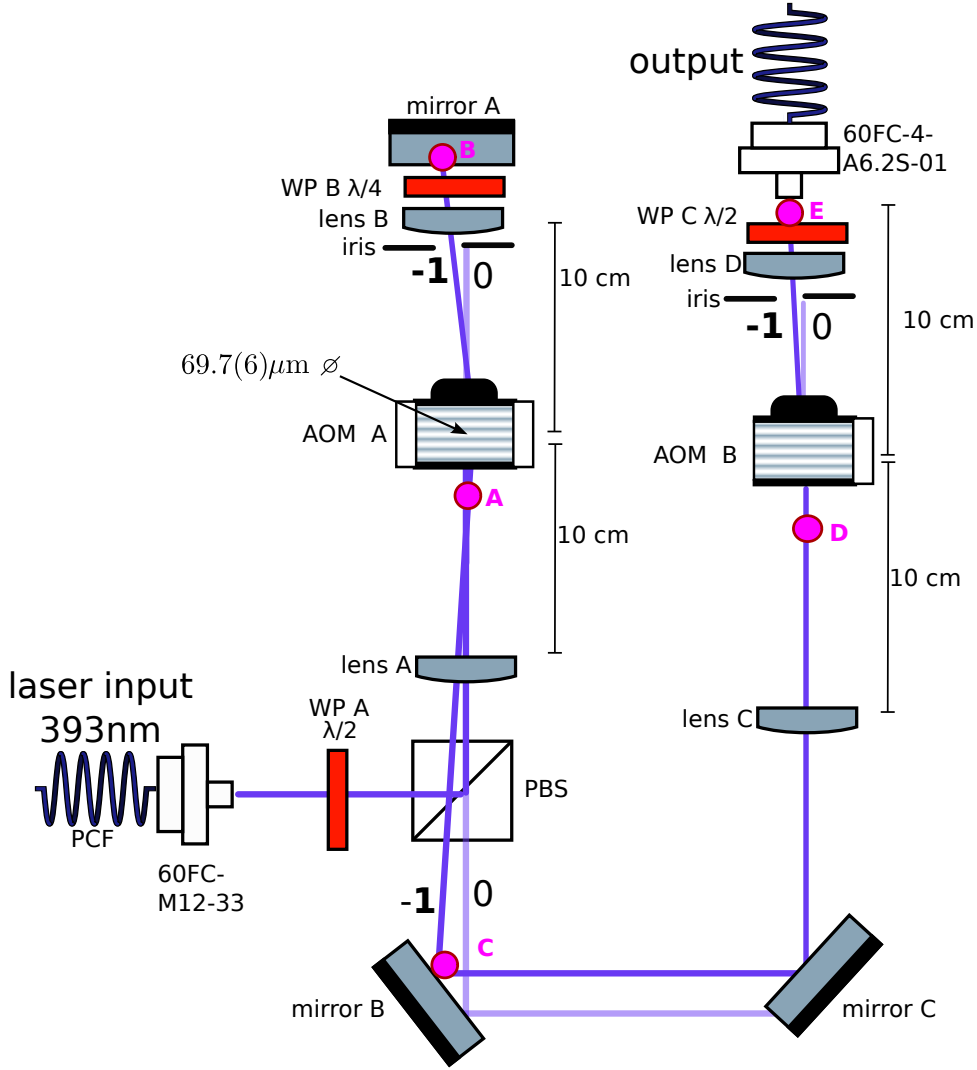
[6] Both Thorlabs, LA1509-A

Figure 4.1.: AOM network for the far detuned setup - Laser light at 393 nm is fed into the optical setup by a photonic crystal fibre (PCF) and coupled to free space with a fibre collimator. AOM A with a carrier frequency $f_c = 1$ GHz is in double pass. AMO B with $f_c = 600$ MHz is in single pass. Data sheets of the AOMs are in Appendix A.1. The signal output is detuned by -2.6 GHz and coupled to a fibre. Wave plates are labelled with WP A, B, C (CeNing Optics) and the corresponding delay $\lambda/2$ or $\lambda/4$. Lens A-D (Thorlabs) have a focal length of $f = 10$ cm. The distance between the lenses is indicated. The $1/e^2$ beam diameter $\varnothing$ at the focal point of lens A is indicated. Pink dots labelled A-E indicate detection points that are used in experiments presented in Section 4.3.1.

diffraction order, the detuning generated in the presented setup would decrease due to the deflection of the AOD. According to the manufacturer's data sheet (Appendix A.1) the expected diffraction efficiency of AOM A is $\sim 40, \%$ (where the $\sim$ symbol is used by the manufacturer). In the experiment, a maximum diffraction efficiency of $59(2)\,\%$ for the -1st diffraction order in single pass was achieved. In the double pass configuration of AOM A, the 0th diffraction order is blocked using an iris. The -1st diffraction order is reflected back by a mirror. The quarter-wave plate converts the incident linearly polarised light into circular polarisation. Reflection on the mirror changes the direction

of rotation of the circularly polarised light. Transmission through the quarter-wave plate on the return path after reflection causes the polarisation to become orthogonal linearly polarised in relation to the outward path. The -1st diffraction order after the second pass through AOM A is reflected from two mirrors to AOM B, which is set up in single-pass configuration. The carrier frequency of AOM B[7] is $f_c = 600$ MHz. It has the same active aperture of $75\,\mu$m as AOM A. A telescope configuration with the same two lenses is used to focus the light into the AOM. The predicted diffraction efficiency is $\sim$ 40-50 % (data sheet A.1). In the experiment, a maximum diffraction efficiency of 45(5) % was achieved. The output signal detuned by -2.6 GHz is coupled into a fibre[8]. After re-coupling to free space on another optical table, the beam is superimposed with a second light signal from the 393 nm laser on a PBS. Finally, both light signals are coupled into a fibre and directed to the addressing setup in the mu-metal chamber.

Both AOMs used in this study have a specified power damage threshold of 1 W radio-frequency (RF) input power. Our experience working with the AOMs has shown that these devices are highly sensitive to the power threshold. The AOM utilises a piezoelectric transducer to generate acoustic waves that prepare an optical grating in a crystal. It is important to avoid exceeding the power threshold, as this can result in burning of an electrode in the piezoelectric transducer. Therefore, it is crucial to operate both AOMs with a stable RF signal to avoid damage caused by exceeding the power threshold. Section 4.3.1 specifies the RF frequency of the AOMs used in operation in order to avoid damage. Additional damage to the AOMs can be caused by electrostatic discharge when touching the AOMS. A wrist band should be worn for grounding when aligning the AOMs.

4.2.2. Control electronics

This section presents the control electronics used to operate the two AOMs depicted in Figure 4.1. Two RF signals, one at 1 GHz and one at 600 MHz, are generated to operate the AOMs at their carrier frequencies f_c. Two AD9915 [69] direct-digital synthesizers (DDS) are used[9]. The two DDS units are further referred to as DDS 1 and DDS 2. A rack-mountable power supply is used to power the DDS units. The DDS units are controlled by a Raspberry Pi[10]. The Raspberry Pi provides a graphical user interface to control the frequency and power of the DDS output. The graphical user interface is accessible via a LAN network connection to the Raspberry Pi. Upon opening the user interface, users are advised not to change the frequency of the DDS units when connected to the AOMs. This is because the output power is highly sensitive to frequency changes, which may result in the unintentional exceeding of the AOMs' power threshold. The DDS units produce a sinusoidal waveform up to 1 GHz frequency from a 2.5 GHz clock signal. The clock signal is generated using a phase-locked-loop (PLL) that takes the input from a function generator at 10 MHz. The clock output is split to operate both DDS units. AOM A requires a 1 GHz RF-signal. However, the output power of the DDS 1 at 1 GHz is

---

[7]Brimrose, TEF-600-400-393

[8]Schäfer+Kirschhoff, 60FC-4-A6.2S-01

[9]The devices were built by Wolfgang Kuen and Kilian Prokop from the electronics workshop at the Institute of Experimental Physics (UIBK).

[10]Information is provided within the Institute of Experimental Physics on the GitLab page: RaspberryPiUni.

insufficiently large. The frequency of DDS 1 is set to 500 MHz and a frequency doubler[11] is used to generate a 1 GHz signal with sufficient power. The frequency doubler generates sidebands on the frequency spectrum. An additional band pass filter[12] is used to remove the sidebands. AOM B is operated by setting the frequency of DDS 2 to 600 MHz. A transistor-transistor logic signal (TTL) is sent to DDS 2, triggering an internal attenuator that switches off the DDS. The TTL signal is controlled in our experimental control software known as TrICS[13]. The output signals of both DDS units are amplified with two rack-mountable amplifiers[14]. The amplification is set so that the output power is approximately half of the maximum RF power permitted for the AOMs. The resulting output power is approximately 0.5 W.
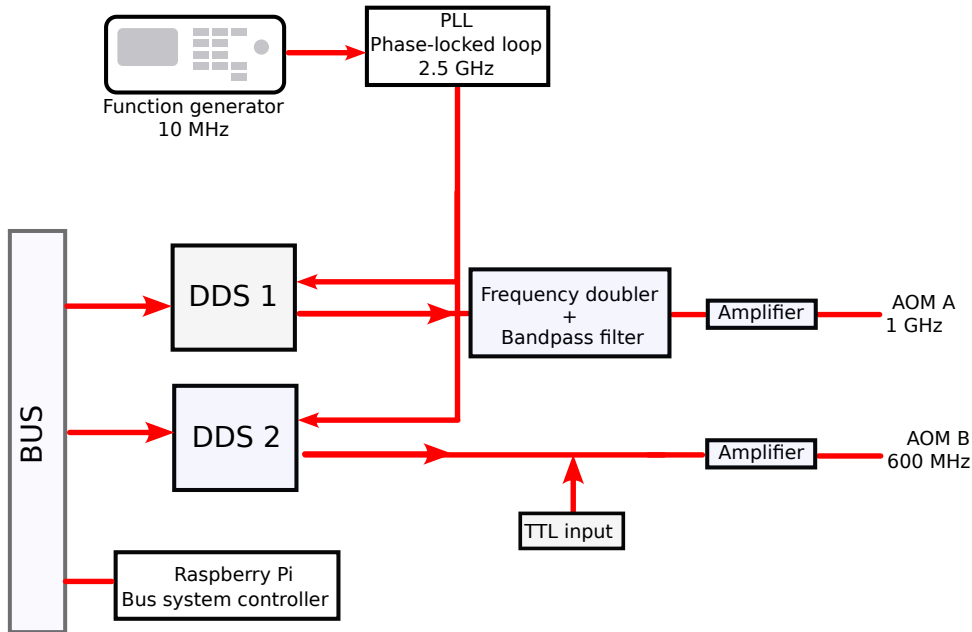

Figure 4.2.: Electronic control system to generate the RF signal for AOM A and AOM B in the optical setup presented in Figure 4.1. The propagation directions of the signals are indicated with arrows.

4.3. Characterisation

This section characterises two key parameters of the optical setup in Figure 4.1: the efficiency as a function of the RF power and the optical power stability. In Section 4.3.1, the characteristic curves of the AOMs are shown in a first experiment. The characteristic curves are defined by the diffraction efficiency of the -1st diffraction order of the AOMs as a function of the RF power. In a second experiment, we characterise the total efficiency of the setup as a function of the RF power sent equally to both AOMs. In the experiment

---

[11]Mini-Circuits, FK-5, 10-1000 MHz

[12]Mini-Circuits, ZX75BP-1135-S+, 900-1370 MHz

[13]Custom software that was developed by students from the Quantum Optics and Spectroscopy group under the supervision of Rainer Blatt.

[14]The amplifiers are built by the electronics workshop.

in Section 4.3.2, the optical power stability of repeated 100 μs-long light pulses at 393 nm generated in the far detuned setup is analysed.

4.3.1. Efficiency

The diffraction efficiency η of an AOM is defined as

$$\eta = \frac{I}{I_0}, \tag{4.1}$$

where I is the optical power of the -1st diffraction order and I_0 is the total optical power (all diffraction orders) transmitted through the AOM. The RF power of the individual RF sources for AOM A and AOM B can be varied in the graphical user interface of the Raspberry Pi. The optical power is measured with a power meter[15]. An iris is used when selecting the -1st diffraction order. Figure 4.4 shows the diffraction efficiency η as a function of the RF power for both AOMs individually. The diffraction efficiency saturates at an RF power greater 0.4 W for both AOMs operated in single pass. In the experiments conducted in this work, the RF powers of both AOMs were set to $0.5 - 0.6$ W.
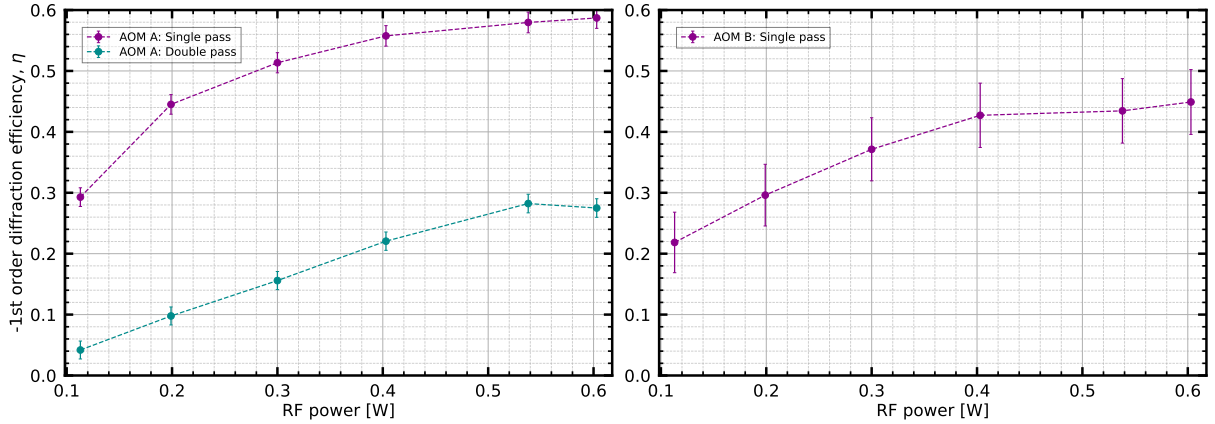

Figure 4.3.: -1st order diffraction efficiency of the AOMs in the far detuned setup shown in Figure 4.1 as a function of RF power. The diffraction efficiency is defined in Equation 4.1. Two curves are shown for AOM A, representing the diffraction efficiency in single-pass, calculated from the optical power I_0 at detection point A and I at detection point B in Figure 4.1, and double-pass configuration, detection points A and C. The diffraction efficiency of AOM B is calculated from the optical power I_0 at the detection point D and I at the detection point E in Figure 4.1.

In a second experiment, the total efficiency of the setup was measured as a function of the RF power applied equally to both AOMs. The total efficiency is defined by Equation 4.1, where I_0 is the input power of the setup, i.e. the light power after the first fibre collimator in Figure 4.1, and I is the optical power at the output. The total efficiency is mainly determined by losses at the two AOMs, but also by losses at the optical elements such as lenses and wave plates. The RF power was set to a maximum of 0.6 W to avoid exceeding the damage threshold (1 W) of the AOMs. Figure 4.4 shows the result. The maximally achieved total efficiency is 0.13(2).
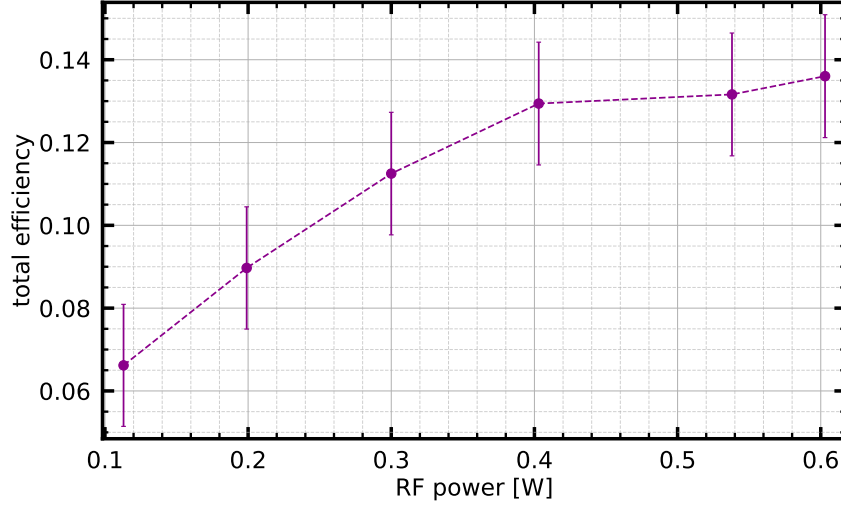
---

[15]Thorlabs, PM100D

Figure 4.4.: Total efficiency of the far detuned setup in Figure 4.1 calculated from the optical power I_0 and I at the detection points A and E according to Equation 4.1, as a function of RF power. The RF power is applied equally to both AOMs in the setup.

4.3.2. Optical power stability

The optical power stability of 393 nm laser light generated with the far detuned setup shown in Figure 4.1 was measured by sending successive 100 μs-long light pulses with an average time separation of 2 s to a photodiode[16] located in the mu-metal shield. The photodiode output was recorded on an oscilloscope to provide the time traces of the light pulses. The voltage V measured with the oscilloscope is converted to light power P by

$$P = \frac{V}{R(\lambda) \cdot TG \cdot SF}, \tag{4.2}$$

where $R(\lambda) = 0.075 \text{A/W}$ is the responsivity of the photodiode, $TG = 4.75 \cdot 10^5$ is the Transimpedance Gain and SF is the Scale Factor that is defined as

$$SF = \frac{R_{\text{load}}}{R_{\text{load}} + R_s} \tag{4.3}$$

with the load resistor $R_{\text{load}} = 1 \text{M}\Omega$ and the series resistor $R_s = 50\,\Omega$. The load resistor R_{load} is applied manually to the output of the photodiode, while the series resistor R_s is built into the photodiode. All relevant parameters for the conversion are taken from the manual of the photodiode [70].

An example time trace of a single recorded pulse is presented in Figure 4.5. Zooming in on a 1 μs time scale shows that the power signal is modulated at a high frequency of around 7 MHz. In order to compare the optical powers in different pulses, we calculate the average optical power for each pulse within the time window $t = [35, 175]\,\mu$s. For the uncertainty in that value, we use the average value of the background noise, taken as the average value outside the defined time window $35\,\mu$s $> t > 175\,\mu$s. The analysis is performed on all measured light pulses and presented in Figure 4.6. The light pulses were
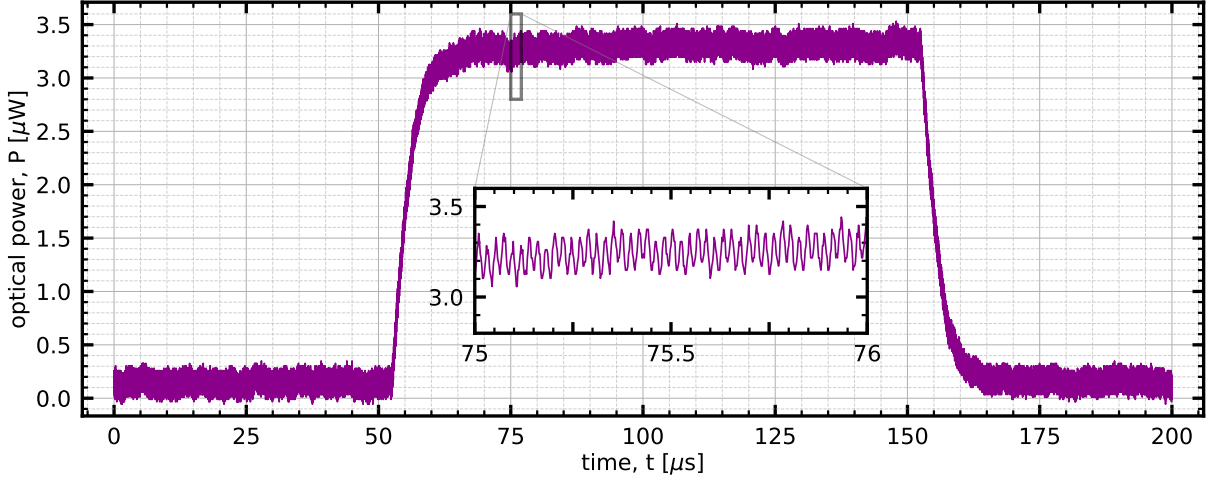
---

[16]Thorlabs, PDA36A-EC

Figure 4.5.: Time trace of a 100 μs-long light pulse of the far detuned 393-beam. The signal is detected with a photodiode and recorded on an oscilloscope. The voltage measured with the oscilloscope is converted to optical power by Equation 4.2. In addition to the full time trace, a zoom is shown in a time window of one microsecond $75\,\mu$s $< t < 76\,\mu$s.

repeated continuously. However, some data were excluded from the analysis because they were stored when no light signal was recorded due to incorrect triggering of the oscilloscope. Therefore, the time interval between two consecutive light pulses is not constant. The average optical power over all light pulses is $2.39\,\mu$W. The standard deviation of the average is $0.01\,\mu$W. The data exhibits a dynamical structure, indicating slow power fluctuations. The data is not entirely consistent with randomly fluctuating powers. For example, in the time window $30\,$s $< t < 40\,$s the data is consistent with a drop in power by around half of a percent. Nevertheless, significant fluctuations on the order of 0.5-1 % are evident over $100\,$s of the experiment.
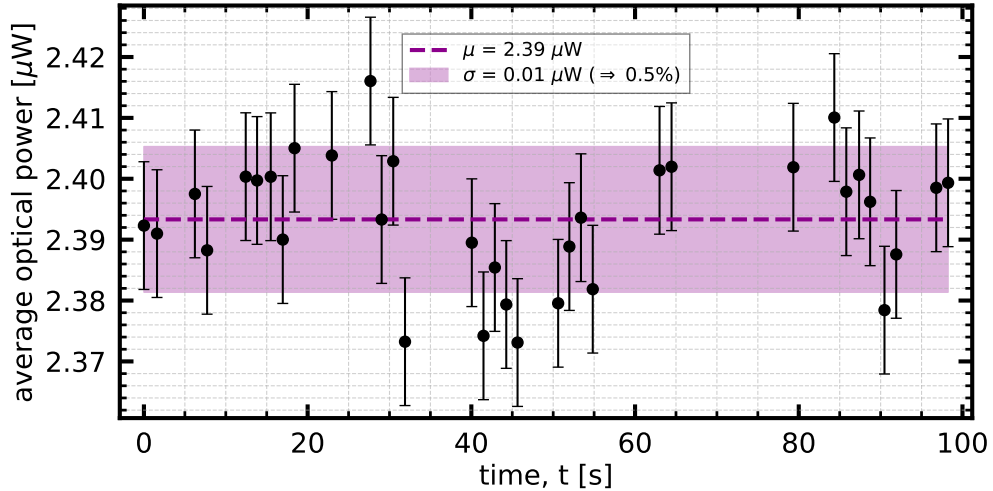
Figure 4.6.: Average optical power (black dots with error bars) of 34 light pulses, each $100\,\mu$s long, of 393 nm laser light generated in the far detuned setup shown in Figure 4.1 and measured on a photodiode inside the mu-metal shield. The main text explains how errors are assigned. The average μ of the data is represented by a purple dashed line, while the purple shaded area indicates the standard deviation σ corresponding to $\sigma/\mu = 0.5\,\%$ of the average.

31

5. Realising single-qubit gates via the AC Stark effect

This chapter presents the results of experiments in which the far detuned 393-beam is used to manipulate individual ions within an ion string. Section 5.1 presents the measurement of AC Stark flops observed on a single-ion within a four-ion string. The implementation of this experiment relies on Ramsey spectroscopy to probe the AC Stark shift on an ion-qubit i that was introduced in Equation 3.3. The primary focus of Section 5.1 it to present our understanding of the sources of imperfections that lead to damping of the AC Stark flops. This understanding is developed by comparing the data to various models. Section 5.2 provides an in-depth study of the fidelity with which we can perform a single-qubit z-flip $R_z^{(i)}(\theta = \pi)$ on an ion-qubit i and its limitations. The main focus of the analysis is to determine the contributions of the known error sources to the infidelity. Finally, the results are summarised.

5.1. Measurement of AC Stark flops

This section presents the first results from applying the far detuned 393-beam to an ion string. Specifically, the goal was to observe AC Stark flops on a single-ion in a chain. The results for this experiment are presented in Section 5.1.1. The data are first compared with Model 1 in Section 5.1.2 which includes dephasing due to spontaneous scattering. Then, two other models, Model 2 in Section 5.1.3 and Model 3 in Section 5.1.4, are presented and also compared with the data. In addition to spontaneous scattering, these models take into account intensity and also phase fluctuations of the lasers used at $393\,\mathrm{nm}$ and $729\,\mathrm{nm}$, respectively.

5.1.1. Experimental details and results

In this experiment, four $^{40}\mathrm{Ca}^+$ ions were trapped with an axial confinement[1] of $\omega_z = 2\pi \times 360\,\mathrm{kHz}$. The following Zeeman states were used to encode the logical states of a qubit: $|S\rangle = |4^2S_{1/2}, m_j = -1/2\rangle$ (ground state) and $|D\rangle = |3^2D_{5/2}, m_j = -5/2\rangle$ (excited state). The radial $729\,\mathrm{nm}$ beam, that is shown in Figure 3.2, is used to probe the transition. First, we perform $5\,\mathrm{ms}$ of Doppler cooling. Then, the ions are initialised by $80\,\mu\mathrm{s}$ of optical pumping (Figure 3.3) in the ground state $|S\rangle$. The pulse sequence executed after ion-qubit initialisation is presented in Figure 5.1. A first global $729\,\mathrm{nm}$ pulse $R(\theta = \pi/2, \phi = 0)$ as defined in Equation 3.2 prepares an equal superposition of the qubit states. Next, within

---

[1] We use the shuttling board in this experiment to apply $160\,\mathrm{V}$ to the DC electrodes of the trap. Information on the shuttling board is currently only available on the group's internal Labblog website.
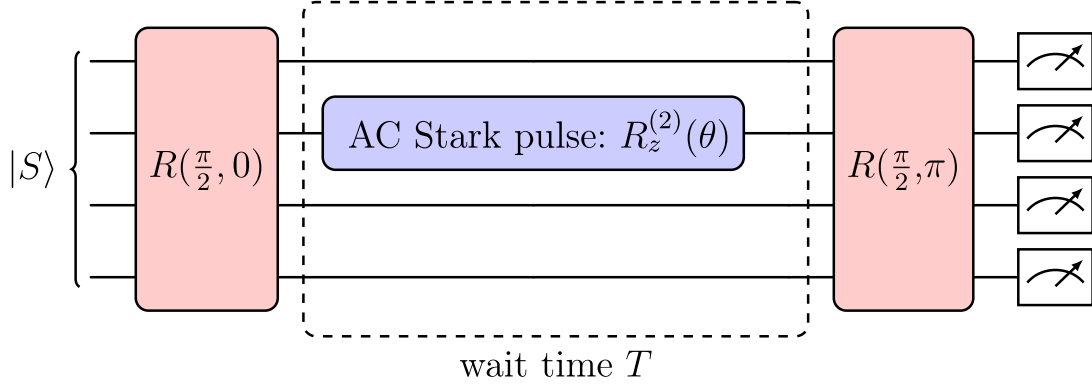
Figure 5.1.: Pulse sequence to implement AC Stark flops on the second ion out of a four-ion string. All ions are initially prepared in $|S\rangle = |4^2S_{1/2}, m_j = -1/2\rangle$. Global rotations $R(\theta, \phi)$ are defined in Equation 3.2. The AC Stark pulse $R_z^{(2)}(\theta)$ is defined in Equation 3.3. Global rotations are implemented with 729 nm laser light, and AC Stark pulses with 393 nm laser light generated in the setup shown in Figure 4.1. The wait time T between the two global 729 nm pulses is fixed to 200 μs. The logic state of each ion-qubit is measured at the end of the sequence.

a fixed wait time of $T = 200\,\mu$s, a single-ion (ion 2) is addressed with the far detuned 393-beam implementing an AC Stark pulse $R_z^{(2)}(\theta)$ on ion-qubit 2 as defined in Equation 3.3. The 393-beam is detuned by $\Delta = -2.7\,$GHz from the $4^2S_{1/2}$ to $4^2P_{3/2}$ transition as explained in Section 4.2. Next, a second global 729 nm pulse $R(\theta = \pi/2, \phi = \pi)$ maps the information of the acquired phase in each ion-qubit to the probability distribution of the electron occupation between the $|S\rangle$ and $|D\rangle$ states. After the pulse sequence shown in Figure 5.1, electron shelving is performed. The fluorescence is recorded on the CCD camera, allowing the logic state of each ion-qubit to be determined after the execution of each pulse sequence (one cycle). Over 100 repeated cycles, the $|D\rangle$ state excitation probability is estimated. Errors are assigned to probabilities according to the quantum projection noise defined in Equation 3.1. The length τ of the AC Stark pulse, as well as its Rabi frequency Ω and the detuning Δ, determine the effective population transfer from $|S\rangle$ to $|D\rangle$ within the sequence. The $3^2D_{5/2}$ excitation probability P_D to find the addressed ion in the $|D\rangle$ state is given by

$$P_D = \frac{1}{2}(1 + \cos(\theta)), \tag{5.1}$$

where the rotation angle $\theta = \delta_{AC}\tau$ is defined by the AC Stark shift δ_{AC} in Equation 2.43, and the AC Stark pulse length τ.

The black data points in Figure 5.2 show the measured excitation probability P_D for the addressed ion (ion 2) within the four-ion string as a function of the AC Stark pulse length τ. Damping of the oscillation amplitude is clearly evident from the data. Figure 5.3 shows the excitation probability on the remaining unaddressed three ions trapped in the same experiment. The data of the unaddressed ions shown in Figure 5.3 is further discussed in Section 5.1.4.
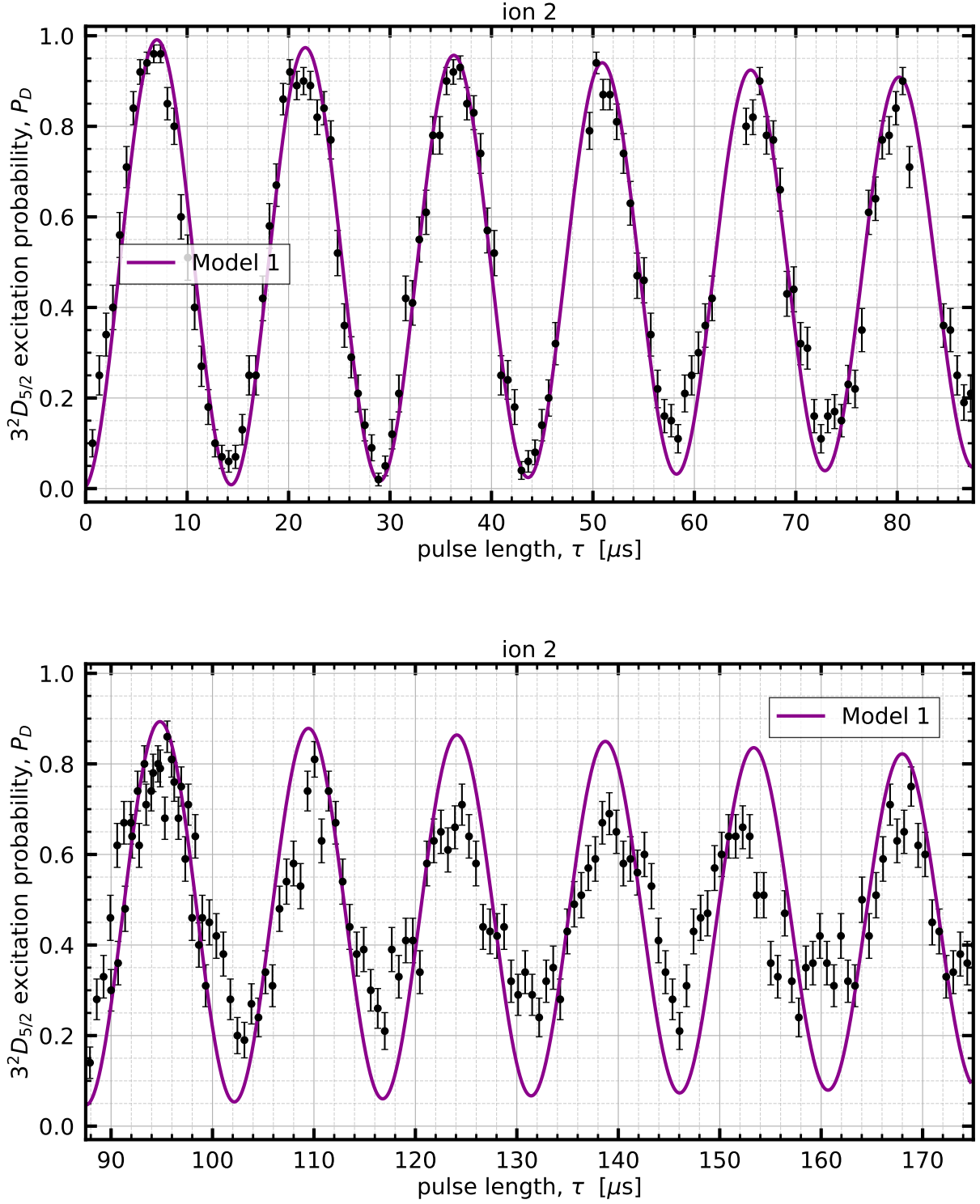
Figure 5.2.: AC Stark flops on ion 2 out of a four-ion string. Black points with error bars show data. The purple line shows Model 1, which is introduced in Section 5.1.2. Error bars on the excitation probability P_D are given by quantum projection noise according to Equation 3.1 for 100 cycles. Data points that are known to be due to ion-string melting events are not shown in the figure. The bottom panel shows a continuation in time of the top panel.
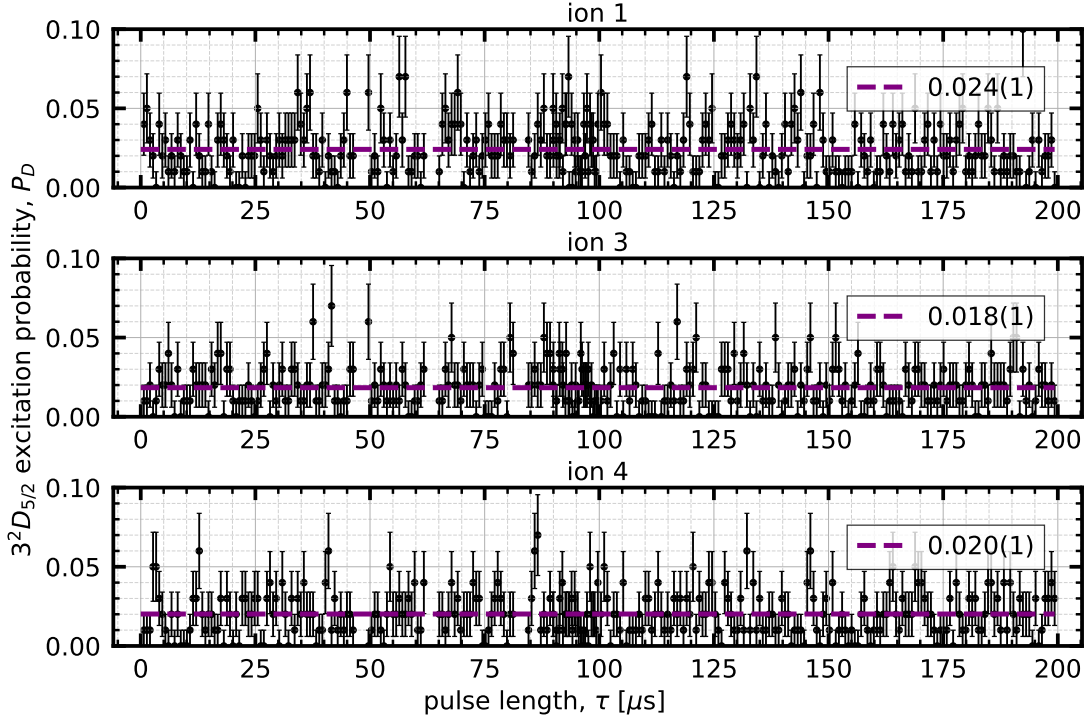
Figure 5.3.: Excitation probability of three unaddressed ions in a four-ion string. Data in this figure and Figure 5.2 are from the same experimental run. The dashed lines show the average excitation probability with standard error. The data is further discussed in Section 5.1.4.

5.1.2. Model 1 and comparison with data

To understand how spontaneous scattering from the $|P\rangle$ state affects the data presented in Figure 5.2, a theoretical model referred to as Model 1 is developed and compared with the data. In particular, the goal is to develop an understanding of the contribution of spontaneous scattering to the damping observed in the AC Stark flops. Model 1 is based on a five-level representation of a $^{40}\mathrm{Ca}^+$ ion that is illuminated by the far detuned 393 nm laser light.

Modelling spontaneous scattering in a five-level atom interacting with a laser field

AC Stark flops were measured as a result of the interaction of far detuned 393 nm laser light generated in the setup shown in Figure 4.1. The time dynamics of the AC Stark flops are affected by spontaneous scattering, if the ion is unintentionally excited to the $4^2P_{3/2}$ manifold. Scattering from that manifold results in damping of AC Stark flops. Section 2.4 provides the mathematical description of a two-level atom interacting with a far detuned laser field, which leads to AC Stark shifts. Here, the two-level model is extended to a five-level model. Figure 5.4 shows the fine structure of the $4^2S_{1/2}$, $4^2P_{3/2}$ and $3^2D_{5/2}$ manifolds of $^{40}\mathrm{Ca}^+$ which are especially relevant to simulate the experiment presented in Section 5.1.1. In the experiment, the initial state is $|S\rangle = |4^2S_{1/2}, m_j = -1/2\rangle$. During a 393 nm laser pulse, which ideally only induces an AC Stark shift of the energy levels, the electron can be excited to the $4^2P_{3/2}$ manifold leading to the spontaneous emission of a photon. The far detuned 393-beam is set to be linearly polarised and perpendicular to

35

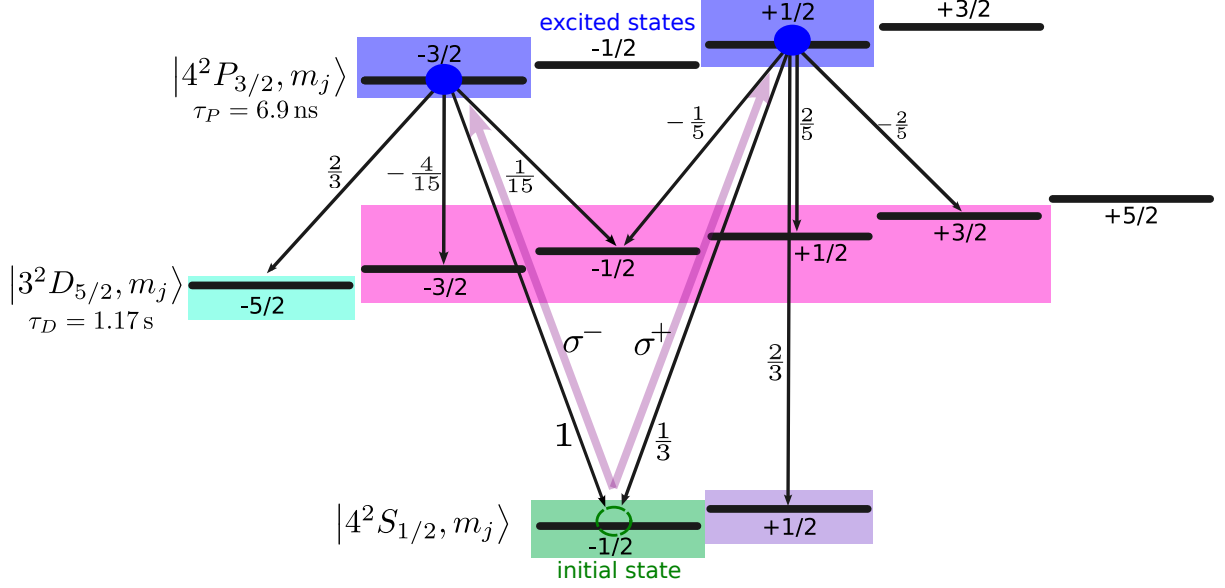## 5. Realising single-qubit gates via the AC Stark effect

Figure 5.4.: Zeeman states of the $4^2S_{1/2}$, $4^2P_{3/2}$ and $3^2D_{5/2}$ manifolds in a ^{40}Ca$^+$ ion. The magnetic quantum numbers m_j are shown below or above the corresponding state (solid black line). The lifetime of the $4^2P_{3/2}$ and the $3^2D_{5/2}$ manifold is indicated with τ_P [42] and τ_D [43], respectively. The initial state of the electron is $|4^2S_{1/2}, m_j = -1/2\rangle$ (green). A 393 nm laser drives σ^+- and σ^--dipole transitions (purple arrows). The decay channels indicated as black arrows together with the squared values of the Clebsch-Gordon coefficients show all possible paths of the first spontaneous decay from the two excited states (dark blue). Some Zeeman states of the fine structure shown here are merged, resulting in five artificial states. Merged states are colour-coded.

the magnetic field axis in our experimental setup. In this configuration, the laser can only drive σ^+- and σ^--dipole transitions. Accordingly, only transitions with $\Delta m_j = -1, +1$ are possible. From the initial state $|S\rangle$, possible excited states of the $4^2P_{3/2}$ manifold are therefore $|4^2P_{3/2}, m_j = -3/2\rangle$ and $|4^2P_{3/2}, m_j = +1/2\rangle$. Both of these excited states can decay to the $4^2S_{1/2}$, $3^2D_{3/2}$ (not indicated in Figure 5.4) and $3^2D_{5/2}$ manifolds. The decay rate to the $3^2D_{3/2}$ manifold is one order of magnitude smaller than the other decay channels which is why it is neglected in Figure 5.4 and the model, leaving only decay to the $4^2S_{1/2}$ and $3^2D_{5/2}$ manifolds. The possible decay channels for the first spontaneous emission event after a single excitation to one of the two excited states together with the squared values of the Clebsch-Gordon coefficients are shown in Figure 5.4. The Clebsch-Gordon coefficients are also summarised in Table 5.1. Only the first spontaneous emission event is taken into account. Subsequent further excitation events are neglected.

The 12-level system presented in the Figure 5.4 can be reduced to a five-level system by grouping related Zeeman states. The qubit is encoded in the $|S\rangle = |4^2S_{1/2}, m_j = -1/2\rangle$ and $|D\rangle = |3^2D_{5/2}, m_j = -5/2\rangle$ states and these are held as two unique states in the five-level model. As a third state, the two possible excited Zeeman states $|4^2P_{3/2}, m_j = +1/2\rangle$ and $|4^2P_{3/2}, m_j = -3/2\rangle$ are grouped into one artificial state $|P\rangle$. A fourth state is given by $|S'\rangle = |4^2S_{1/2}, m_j = +1/2\rangle$, which, when populated after a spontaneous emission event, yields a bright fluorescing image on the CCD camera during electron shelving readout. Finally, the sum of all other pink Zeeman states in the $3^2D_{5/2}$ manifold shown

in Figure 5.4 are grouped into the state $|D'\rangle$. When $|D'\rangle$ is populated, the ion appears dark during electron shelving. Those five merged states are indicated colour-coded in Figure 5.4: $|S\rangle$ green, $|S'\rangle$ purple, $|P\rangle$ dark blue, $|D\rangle$ cyan and $|D'\rangle$ pink.
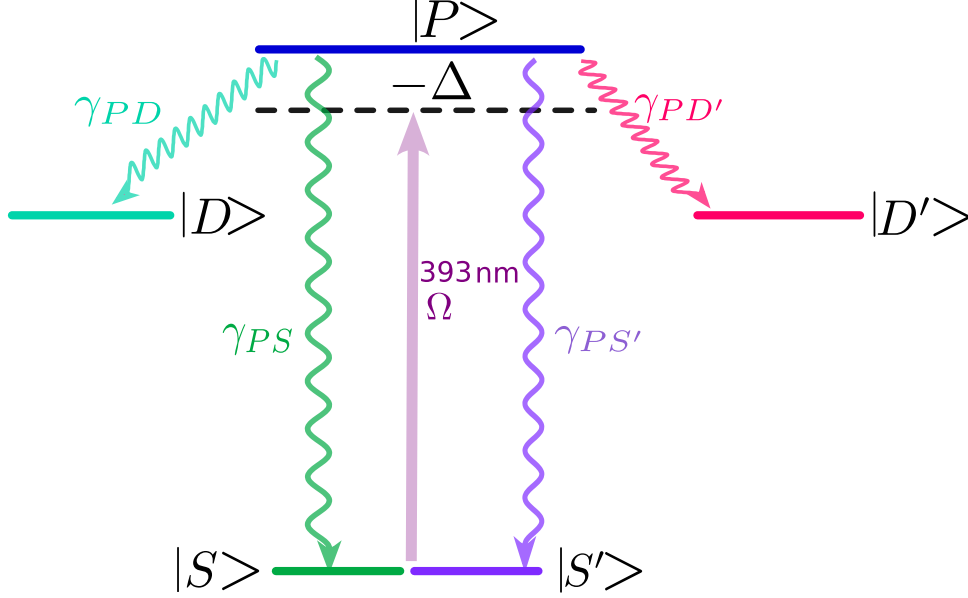

Figure 5.5.: Decay channels from the short-lived state $|P\rangle$. The five states $|S\rangle$, $|S'\rangle$, $|P\rangle$, $|D\rangle$ and $|D'\rangle$ are defined in the main text with reference to Figure 5.4. The scattering rates γ_{ij}, where i denotes the initial state and j the final state of the transition, are defined in Equations 5.2 to 5.5.

Figure 5.5 shows a diagram of the five-level system described in the previous paragraphs in which a driving laser detuned by $-\Delta$ from the $|S\rangle$ to $|P\rangle$ transition frequency off-resonantly excites the short-lived $|P\rangle$ state. The coupling strength of the $|S\rangle$ to $|P\rangle$ transition is defined by the Rabi frequency Ω. The scattering rates from the excited state $|P\rangle$ are indicated in Figure 5.5 as γ_{ij}, where i denotes the initial state and j the final state of the transitions. The individual scattering rates are calculated from the total scattering rate of the $4^2P_{3/2}$ manifold, using branching ratios r_{ij} and Clebsch-Gordon coefficients $G_{m_j}^{m_i}$. The indices m_i and m_j denote the magnetic quantum number of the states i and j. The scattering rates are calculated as

$$\gamma_{PS} = \gamma_P \times r_{P_{3/2}S_{1/2}} \times \left[(G_{-1/2}^{-3/2})^2 + (G_{-1/2}^{+1/2})^2 \right] \tag{5.2}$$

$$\gamma_{PS'} = \gamma_P \times r_{P_{3/2}S_{1/2}} \times (G_{+1/2}^{+1/2})^2 \tag{5.3}$$

$$\gamma_{PD} = \gamma_P \times r_{P_{3/2}D_{5/2}} \times (G_{-5/2}^{-3/2})^2 \tag{5.4}$$

$$\gamma_{PD'} = \gamma_P \times r_{P_{3/2}D_{5/2}} \times \left[(G_{-3/2}^{-3/2})^2 + (G_{-1/2}^{-3/2})^2 + (G_{-1/2}^{+1/2})^2 + (G_{+1/2}^{+1/2})^2 + (G_{+3/2}^{+1/2})^2 \right], \tag{5.5}$$

where $\gamma_P = 1/2\tau_P = 2\pi \times 11.49(3)$ MHz is the total scattering rate of the $4^2P_{3/2}$ manifold with $\tau_P = 6.924(19)$ ns [42], $r_{P_{3/2}S_{1/2}} = 0.9347(3)$ and $r_{P_{3/2}D_{5/2}} = 0.0587(2)$ [71] are branching rations. For these parameters the scattering rates are

$$(\gamma_{PS}, \gamma_{PS'}, \gamma_{PD}, \gamma_{PD'}) = 2\pi \times (7.160(19), 3.580(9), 0.2248(6), 0.4496(12)) \text{ MHz}. \tag{5.6}$$

Transition	Clebsch-Gordon coefficient
$\lvert 4^2 P_{3/2}, +\frac{1}{2} \rangle \leftrightarrow \lvert 4^2 S_{1/2}, +\frac{1}{2} \rangle$	$G^{+1/2}_{+1/2} = \sqrt{\frac{2}{3}}$
$\lvert 4^2 P_{3/2}, +\frac{1}{2} \rangle \leftrightarrow \lvert 4^2 S_{1/2}, -\frac{1}{2} \rangle$	$G^{+1/2}_{-1/2} = \sqrt{\frac{1}{3}}$
$\lvert 4^2 P_{3/2}, -\frac{3}{2} \rangle \leftrightarrow \lvert 4^2 S_{1/2}, -\frac{1}{2} \rangle$	$G^{-3/2}_{-1/2} = 1$
$\lvert 4^2 P_{3/2}, +\frac{1}{2} \rangle \leftrightarrow \lvert 3^2 D_{5/2}, +\frac{3}{2} \rangle$	$G^{+1/2}_{+3/2} = -\sqrt{\frac{2}{5}}$
$\lvert 4^2 P_{3/2}, +\frac{1}{2} \rangle \leftrightarrow \lvert 3^2 D_{5/2}, +\frac{1}{2} \rangle$	$G^{+1/2}_{+1/2} = \sqrt{\frac{2}{5}}$
$\lvert 4^2 P_{3/2}, +\frac{1}{2} \rangle \leftrightarrow \lvert 3^2 D_{5/2}, -\frac{1}{2} \rangle$	$G^{+1/2}_{-1/2} = -\sqrt{\frac{1}{5}}$
$\lvert 4^2 P_{3/2}, -\frac{3}{2} \rangle \leftrightarrow \lvert 3^2 D_{5/2}, -\frac{1}{2} \rangle$	$G^{-3/2}_{-1/2} = \sqrt{\frac{1}{15}}$
$\lvert 4^2 P_{3/2}, -\frac{3}{2} \rangle \leftrightarrow \lvert 3^2 D_{5/2}, -\frac{3}{2} \rangle$	$G^{-1/2}_{-3/2} = -\sqrt{\frac{4}{15}}$
$\lvert 4^2 P_{3/2}, -\frac{3}{2} \rangle \leftrightarrow \lvert 3^2 D_{5/2}, -\frac{5}{2} \rangle$	$G^{-1/2}_{-5/2} = \sqrt{\frac{2}{3}}$

Table 5.1.: Clebsch-Gordon coefficients of various transitions in ^{40}Ca$^+$. The entries contain the coefficients for the decay channels indicated in Figure 5.4.

Now a mathematical description of the time evolution of the 5-level system presented in Figure 5.5 is given. The coherent evolution of the system is defined by a Hamiltonian H. Decoherence due to spontaneous scattering is included by the master equation formalism. The master equation in Lindblad form is given by

$$\frac{\mathrm{d}\rho_0}{\mathrm{d}t} = -\frac{i}{\hbar}[H, \rho_0] + \sum_k [2 L_k \rho L_k^\dagger - \{L_k^\dagger L_k, \rho_0\}], \qquad (5.7)$$

where t is the time that the ion is illuminated by the laser, ρ_0 is the density matrix of the atomic state at $t = 0$. The Lindblad operators L_k describe the scattering of a photon, with the ion undergoing a transition from state $\lvert i \rangle$ to $\lvert j \rangle$, by the operator $L_k = \sqrt{2\gamma_{ij}}\sigma_{ij}$ which contains the atomic lowering operator $\sigma_{ij} = \lvert i \rangle \langle j \rvert$ and the scattering rate γ_{ij}. For the five-level system there are four Lindblad operators, one for each decay channel presented in Figure 5.5. The Hamiltonian is defined according to Equation 2.42 in a five-dimensional Hilbert space: $\lvert S \rangle = (1, 0, 0, 0, 0)$, $\lvert P \rangle = (0, 1, 0, 0, 0)$, $\lvert D \rangle = (0, 0, 1, 0, 0)$, $\lvert D' \rangle = (0, 0, 0, 1, 0)$, $\lvert S' \rangle = (0, 0, 0, 0, 1)$, yielding

$$H = -\frac{\Delta}{2}\big(\lvert S \rangle \langle S \rvert - \lvert P \rangle \langle P \rvert\big) + \frac{\Omega}{2}\big(\lvert S \rangle \langle P \rvert + \lvert P \rangle \langle S \rvert\big) \qquad (5.8)$$

where Ω is the Rabi frequency on resonance of the $\lvert S \rangle$ to $\lvert P \rangle$ transition and Δ is the detuning with respect to the transition.

Simulation methods

The simulation predicts the excitation probability P_D of the addressed ion for various AC Stark pulse lengths τ. The simulations presented in this thesis are written in Python specifically using the Python library QuTip [72] to implement quantum operations.

5. Realising single-qubit gates via the AC Stark effect

The first step in the Python simulation is to define the five-dimensional Hilbert space of the five-level system as well as all required operators and parameters. The quantum states $|S\rangle, |S'\rangle, |P\rangle, |D\rangle$ and $|D'\rangle$ are defined individually. The operators in the experimental sequence shown in Figure 5.1 are defined as follows. A 5×5 unitary matrix $R(\theta, \phi)$ is defined as a function of a given angle θ and a phase ϕ. The matrix represents the global rotations presented in Equation 3.2, involving the qubit states $|S\rangle$ and $|D\rangle$, that are implemented with the 729-laser in the lab. The explicit global rotations, $R(\pi/2, 0)$ and $R(\pi/2, \pi)$, are defined using this matrix. Then the main system parameters are defined. These parameters are the total scattering rate of the $3^2P_{3/2}$ manifold γ_P, the Rabi frequency Ω and the detuning Δ of the AC Stark pulses at 393 nm. While γ_P is given from literature [42], Ω and Δ are measured directly. The detuning Δ is measured via spectroscopy[2] of the $|S\rangle$ to $|P\rangle$ transition, before conducting the actual experiment (measurement of AC Stark flops), yielding $\Delta = -2.74(1)\,\text{GHz}$. The Rabi frequency Ω is calibrated from the data that is shown in Figure 5.2. Specifically, a sine function is fitted to the data to determine the frequency of the flops which is the AC Stark shift. The AC Stark shift δ_{AC} is used to calculate the Rabi frequency Ω using Equation 2.43. A detailed description of the Rabi frequency calibration method is presented in Appendix B.1. The obtained value is $\Omega = 68.6(2)\,\text{GHz}$. As a next step, the Clebsch-Gordon coefficients presented in Table 5.1 and branching ratios, that are defined in the main text, are defined. The individual scattering rates $(\gamma_{PS}, \gamma_{PS'}, \gamma_{PD}, \gamma_{PD'})$ can then be defined yielding the Lindblad operators L_k with $k = 0, 1, 2, 3$

$$L_0 = \sqrt{\gamma_{PS}}\,|P\rangle\langle S| \tag{5.9}$$

$$L_1 = \sqrt{\gamma_{PS'}}\,|P\rangle\langle S'| \tag{5.10}$$

$$L_2 = \sqrt{\gamma_{PD}}\,|P\rangle\langle D| \tag{5.11}$$

$$L_3 = \sqrt{\gamma_{PD'}}\,|P\rangle\langle D'|. \tag{5.12}$$

The subsequent implementation of the simulation consists of four steps.

1. **Initialisation**: The initial state

$$\rho_0 = \frac{1}{2}\big(\,|S\rangle\langle S| + |S\rangle\langle D| + |D\rangle\langle S| + |D\rangle\langle D|\,\big) \tag{5.13}$$

is prepared by applying the global rotation $R(\pi/2, 0)$ to $|S\rangle$. The generalised definition of the matrix for global rotations leaves the freedom to consider an imperfect preparation of the state ρ_0 if required.

2. **Time evolution**: To model an AC Stark pulse $R_z^{(i)}(\theta = \delta_{\text{AC}}\tau_i)$ on ion-qubit i with a pulse length τ_i, the time evolved state $\rho(\tau_i)$ that is determined by Equation 5.7 with ρ_0 and $t = \tau_i$ is calculated utilising the Python module *mesolve* of QuTip [73]. The module function evolves the density matrix ρ_0 (Equation 5.13) under a master equation defined in Equation 5.7 for a given time τ_i. The output of the

---

[2]An ion is continuously illuminated with the far detuned laser beam. The excitation probability P_D is continuously recorded. The frequency lock of the 393 nm laser on the wavemeter is adjusted to maximise the excitation probability. The maximum is found when the laser is on resonance with the $|S\rangle$ to $|P\rangle$ transition due to scattering to the $3^2D_{5/2}$ manifold. The difference in frequency between the far detuned and resonance cases measured with the wavemeter determines the detuning Δ used in the simulations.

function is the density matrix $\rho(\tau_i)$ representing the quantum state in Sequence 5.1 immediately after the AC Stark pulse. A time array $\tau_i \in [0, 175]\,\mu$s with a total of 3000 evenly spaced entries is defined in the simulation and fed to the *mesolve* function. The resulting states, density matrices $\rho(\tau_i)$ that depend on the AC Stark pulse length τ_i, are stored in a list.

3. **Mapping**: The second global pulse $R(\pi/2, \pi)$ is applied to the density matrices $\rho(\tau_i)$ in the list. The final result of density matrices, denoted as $\rho_f(\tau_i)$, are stored.

4. **Expectation value calculation**: The expectation value

$$P_D(\tau_i) = \text{tr}(|D\rangle \langle D| \rho_f(\tau_i)) \tag{5.14}$$

of the operator $|D\rangle \langle D|$ for the final states $\rho_f(\tau_i)$ is calculated yielding the excitation probability $P_D(\tau_i)$.

Comparison with data

The data in Figure 5.2 shows a non-vanishing excitation probability P_D at $\tau = 0$. This indicates that the second global 729 nm pulse does not completely reverse the first global 729 nm pulse in the experimental sequence (Figure 5.1). The simulation starts with an excitation probability of zero. To ensure a meaningful comparison between the data and simulation, the simulation result is shifted on the time axis to align with the data's starting value of excitation probability. A parameter τ_0 determines the time shift and is calibrated by fitting the function in Equation B.1 to the data in Figure 5.2 (Appendix B.1). The result of the simulation $P_D(\tau_i - \tau_0)$ is plotted in Figure 5.2 with a purple line labelled *Model 1*. Comparison of the data and the model clearly shows that Model 1 does not fully capture the damping observed in the data. The damping rate measured is considerably faster than what is predicted by Model 1.

5.1.3. Model 2: 393-intensity fluctuations and comparison with data

Section 4.3.2 provides evidence for intensity fluctuations of sequentially repeated light pulses generated in the far detuned setup (Figure 4.1). Model 1 is now extended to account for intensity fluctuations of the AC Stark pulses at 393 nm, further known as 393-intensity fluctuations. The extended model is known as *Model 2*. Model 2 includes both spontaneous scattering in a five-level system and 393-intensity fluctuations. This section first provides more details on our use of the experiment presented in Section 4.3.2 to provide an estimate of the intensity fluctuations of the AC Stark pulses. The estimate is used to model the data in Figure 5.2. Secondly, a detailed description of embedding intensity fluctuations of AC Stark pulses in Model 1 is presented.

Estimation of 393-intensity fluctuations

In Section 4.3.2 the distribution of optical power measured with a photodiode in 34 repeated 393 nm laser pulses was presented. In this section, we'll refer to that experiment as the 34-pulse experiment. Specifically, the optical power of 34 100 μs-long light pulses of the far detuned 393-beam with an average time separation of 2 s was measured, yielding a

percentage fluctuation of $\delta I/I = 0.5\,\%$, where I is the average optical power over all pulses and δI is the standard deviation. In the experiment to measure AC Stark flops, referred to as the four-ion experiment, each cycle is repeated 100 times to obtain one data point. Similar to the 34-pulse experiment, light pulses of a variable length τ, which are here the AC Stark pulses, are sequentially repeated. A first conclusion is that therefore intensity fluctuations observed in the 34-pulse experiment also arise in the four-ion experiment.

What is different in the two experiments is, first, that the AC Stark pulse length in the four-ion experiment is varied in time. This means that, strictly speaking, only a single data point, namely the one for $\tau = 100\,\mu$s in Figure 5.2, represents an experiment that is comparable to the 34-pulse experiment. Secondly, the time scale of both experiments differs. The average time separation of the pulses in the 34-pulse experiment is about 2 s. The time for each cycle in the four-ion experiment is mainly determined by the Doppler cooling length of 5 ms and the electron shelving time of 5 ms, i.e. each cycle takes about 10 ms. The time scale over which the pulses are repeated in the four-ion experiment is thus two orders of magnitude smaller than in the 34-pulse experiment. The intensity fluctuations in the four-ion experiment could be significantly different to those in the 34-pulse experiment. Model 2 uses the value of $\delta I/I = 0.5\,\%$ fluctuations from the 34-pulse experiment as a reference. The intensity fluctuations appear in the simulation as fluctuations of the Rabi frequency. The Rabi frequency scales as $\Omega \propto \sqrt{I}$. The fractional error in the Rabi frequency $\delta\Omega/\Omega$ can be estimated as

$$\frac{\delta\Omega}{\Omega} = \frac{\delta I}{2I} = 0.25\,\%. \tag{5.15}$$

Simulation methods: Embedding 393-intensity fluctuations in Model 1

The implementation of Model 1 presented in Section 5.1.2 is retained but is extended to include intensity fluctuations between different AC Stark pulses. In Model 2, to include intensity fluctuations, the intensity of the AC Stark pulse for a fixed pulse length τ_i is allowed to fluctuate from cycle to cycle. Intensity fluctuations of the AC Stark pulses are modelled by Rabi frequency fluctuations. The main parameters that are defined in the beginning of the simulation as described in Section 5.1.2 need to be modified. All other definitions and parameters are equivalent to those of Model 1, except for the Rabi frequency Ω. Intensity fluctuations are modelled as having a Gaussian distribution over the experimental cycles. Specifically, a list of 50 Gaussian distributed Rabi frequency samples is generated with an average $\Omega = 68.6(2)$ GHz and a standard deviation $\delta\Omega = 0.0025 \cdot \Omega$. The list is denoted as $\{\Omega_j\}$. Then the four steps of the Model 1 simulation presented in Section 5.1.2 are modified. The first step remains unchanged. In the second step , the qubit state $\rho(\tau_i)$ after the AC Stark pulse is calculated and stored in a list. The intensity fluctuations are incorporated into this step as follows.

2.1 **Time evolution including 393-intensity fluctuations**: An empty list to store the time evolved quantum states is generated. A loop that iterates over the list of 50 Rabi frequencies $\{\Omega_j\}$ is created. Each loop consists of the following steps.

    a) A Hamiltonian H_j according to Equation 5.8 is defined for the present Rabi frequency Ω_j.

    b) Equation 5.7 is solved with ρ_0, H_j and L_k for a time array $\tau_i \in [0, 175]\,\mu$s.

c) The resulting states $\rho_j(\tau_i)$, corresponding to the current Rabi frequency sample Ω_j, are stored in a list.

After the loop completes, the states obtained for different Rabi frequency samples are averaged, yielding the state

$$\overline{\rho}(\tau_i) = \frac{1}{50} \sum_{j=1}^{50} \rho_j(\tau_i). \tag{5.16}$$

The averaged state is stored in a list $\{\overline{\rho}(\tau_i)\}$.

Each averaged state $\overline{\rho}(\tau_i)$ out of the list is subsequently subject to 3. and 4. of Section 5.1.2, yielding the average excitation probability $P_D(\tau_i)$.

Comparison with data

Figure 5.6 compares the measured and simulated excitation probability using Model 2. Two different values for the intensity fluctuations are presented which are: $\delta\Omega/\Omega = 0.25\,\%$ and $\delta\Omega/\Omega = 1\,\%$. For $\delta\Omega/\Omega = 0.25\,\%$, which is the value obtained from the 34-pulse experiment, the damping rate of the model is not as strong as that of the data. A value of $\delta\Omega/\Omega = 1\,\%$ is qualitatively found to offer a closer match to the data. The damping rate in the data is qualitatively well described by a $1\,\%$ standard deviation of the Rabi frequency from cycle to cycle.
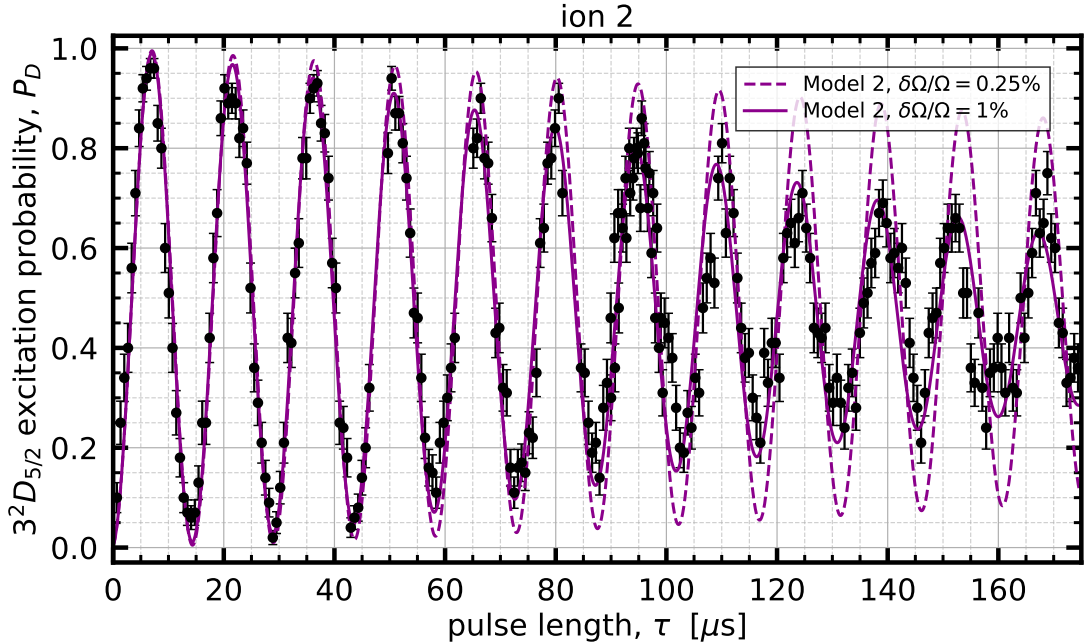

Figure 5.6.: AC Stark flops on ion 2 of a four-ion string and Model 2. The experimental data is the same as in Figure 5.2. Two instances of Model 2 are shown that differ by the strength of intensity fluctuations as captured by the parameter $\delta\Omega/\Omega$ defined in the main text in Section 5.1.3.

5.1.4. Model 3: 729-phase fluctuations and comparison with data

Figure 5.3 shows the excitation probability of the unaddressed ions in the experiment presented in Section 5.1.1. The data shows that the unaddressed ions have a significant excitation probability, although they should ideally have none. One possible cause are phase imperfections of the global 729 nm pulses used at the beginning and the end of the experimental sequence in Figure 5.1. Indeed, in many other experiments not presented in this thesis, we see that such excitation is present due to imperfections in the 729 nm laser pulses alone. This section presents how Model 2 is extended to account for this effect. The final model known as Model 3 now includes spontaneous scattering, 393-intensity fluctuations and 729-phase fluctuations. This section first explains how the experimental data of the unaddressed ions can be used to estimate the amount of phase fluctuations captured by the parameter $\delta\phi/\phi$. Secondly, it is described how phase fluctuations of the 729-laser are embedded in Model 2 to obtain Model 3. Finally, the predictions of Model 3 are compared to the data of the addressed ion.

Estimation of 729-phase fluctuations

The data shown in Figure 5.3 shows the non-vanishing excitation of unaddressed ions in the experiment in Section 5.1.1. The average excitation probability over the number of data points with standard error is presented in the legend of Figure 5.3. The values all agree within one standard deviation. The overall average over the three ions is given by $\bar{P}_D = 0.021(1)$. This non-vanishing excitation probability deviates from an idealised expectation: $P_D = 0$. The conditions under which the excitation probability of the unaddressed ions would completely vanish in the experiment must be carefully defined. The AC Stark pulse must only interact with the addressed ion, i.e. there must be no excitation probability for unaddressed ions due to an addressing error of the AC Stark pulse[3]. No addressing error is evident in Figure 5.3, because the excitation probability for each of the three ions is approximately constant depending on τ. In the case of an addressing error, the excitation probability would increase with the length of the AC Stark pulses. Finally, the phase difference between the first global pulse ϕ_1 and the second global pulse ϕ_2 must be exactly: $\Delta\phi = \phi_2 - \phi_1 = \pi$. If the phase of the 729-laser fluctuates within the time interval between the two global 729 nm pulses, this condition is no longer fulfilled and the state of the ion can no longer return to the initial state. The result is a non-vanishing excitation probability of the unaddressed ions. The magnitude of phase fluctuations depends on the time scale of the time interval between the two global pulses[4]. The excitation probability of unaddressed ions in Figure 5.3 is here modelled solely by phase fluctuations of the 729 nm laser. The amount by which the 729 nm laser would have to fluctuate to be consistent with the data from the unaddressed ions in Figure 5.3 is calculated. The calculation is presented in Appendix B.2. The phase difference between the two global 729 nm pulses in the sequence is modelled to fluctuate with a Gaussian

---

[3]In the master's thesis of Marco Canteri [19], no addressing errors were observed when using the addressing beam at 393 nm.

[4]We have seen in other experiments, that the excitation probability of unaddressed ions depends on the wait time T between the two global pulses at 729 nm in the sequence shown in Figure 5.1.

distribution with an average ϕ and a standard deviation $\delta\phi$. The calculation yields:

$$\frac{\delta\phi}{\phi} = 9.4\,\%. \tag{5.17}$$

Simulation methods: Embedding 729-phase fluctuations in Model 2

Model 3 is an extension of Model 2, now including spontaneous scattering in a 5-level system, 393-intensity fluctuations of $\delta\Omega/\Omega = 1\,\%$ and 729-phase fluctuations of $\delta\phi/\phi = 9.4\,\%$. The steps 1. to 3. are equivalent to those in Model 2 presented in Section 5.1.3. The fourth step is modified as now described.

4.1 **Mapping including 729-phase fluctuations**: A loop that iterates over the list of states $\{\bar{\rho}(\tau_i)\}$ is created. Each loop consists of the following steps.

    a) The current state $\bar{\rho}(\tau_i)$ (Equation 5.16) is retrieved from the list $\{\bar{\rho}(\tau_i)\}$.

    b) A random set of Gaussian phase values $\{\phi_k\}$, $k = 0, 1, ..., 100$, with an average of $\phi = \pi$ and a standard deviation of $\delta\phi = 0.094 \cdot \phi$ is generated. Then an inner loop that iterates over the random phase values is created. Each inner loop consists of the following steps.

        i. A global rotation $R(\pi/2, \phi_k)$ containing the current phase value is constructed.

        ii. The global rotation is applied to the current state $\bar{\rho}(\tau_i)$ of the main loop yielding $\bar{\rho}(\tau_i)_k$.

        iii. The expectation value $P_D(\tau_i)_k$ is calculated for the state $\bar{\rho}(\tau_i)_k$ according to Equation 5.14. The value is stored.

    c) After the inner loop completes, the expectation values obtained for the phase samples are averaged, yielding

$$\overline{P_D}(\tau_i) = \frac{1}{100}\sum_{k=1}^{100} P_D(\tau_i)_k. \tag{5.18}$$

The averaged expectation values are stored in a list $\{\overline{P_D}(\tau_i)\}$.

Comparison with data

Figure 5.7 compares the data to Model 2 and Model 3. According to Model 3, 729-phase fluctuations do not affect the damping rate of the AC Stark flops, but they do cause an overall reduction of contrast

$$c = \frac{\max(P_D) - \min(P_D)}{\max(P_D) + \min(P_D)}, \tag{5.19}$$

regardless of the length of the AC Stark pulse. The contrast that is predicted by Model 3 is compressed by a constant fraction of $2\,\%$ compared to Model 2. Model 3 aligns more closely with the data than Model 2.
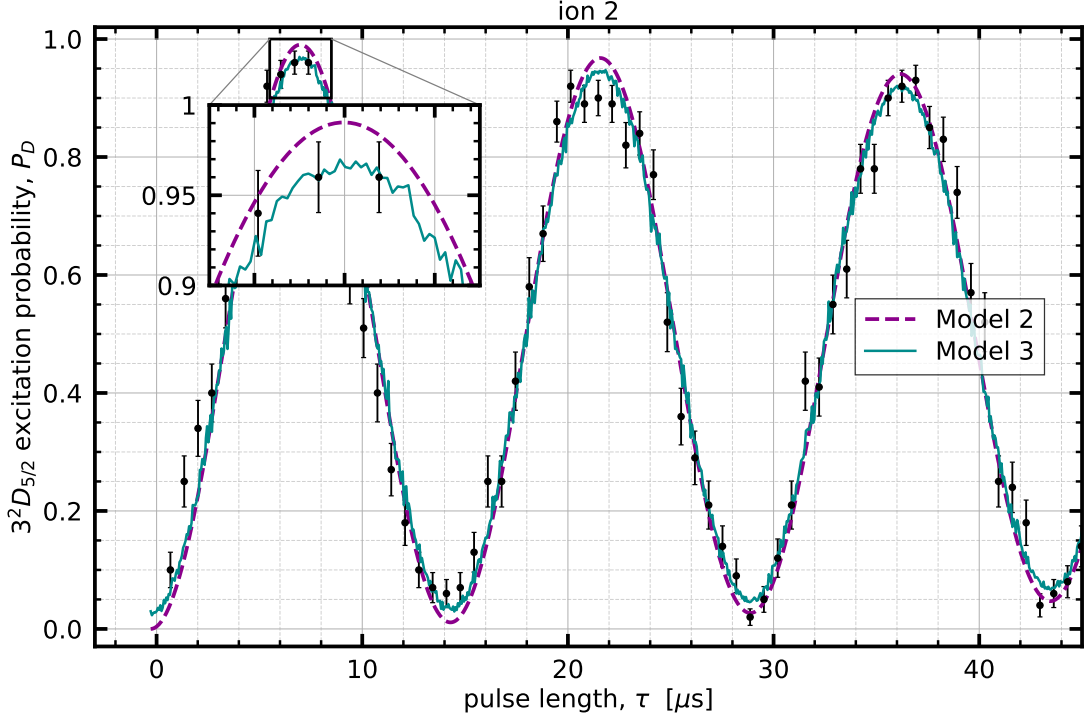
Figure 5.7.: First three AC Stark flops on ion 2 of a four-ion string together with Model 2 and 3. The experimental data is the same as in Figure 5.2. Model 2 (Section 5.1.3) with 1 % 393-intensity fluctuations is indicated as dashed purple line. Model 3 (Section 5.1.4) with 9.4 % 729-phase fluctuations is shown as cyan line.

5.2. Characterisation of single-qubit z-flip

The goal of this section is to partially quantify the fidelity of a *single-qubit z-flip.* In this work, a single-qubit z-flip on ion-qubit i is partially characterised by assessing its ability to rotate the state $|+\rangle$ (Equation 2.2) around the z-axis of the Bloch sphere by an angle π: $R_z^{(i)}(\theta = \pi)$ (Equation 3.3). Ideally this rotation results in the state $|-\rangle$ (Equation 2.2). If the single-qubit z-flip is embedded in a Ramsey experiment

$$R_z = R\left(\frac{\pi}{2}, 0\right) R_z^{(i)}(\theta = \pi) R\left(\frac{\pi}{2}, \pi\right) \tag{5.20}$$

as in the sequence shown in Figure 5.2 for measuring AC Stark flops, a z-flip can be identified with a flip of the qubit state from $|S\rangle$ to $|D\rangle$. When measuring AC Stark flops a z-flip occurs when the excitation probability changes from its minimum, ideally 0, to its maximum, ideally 1. A first z-flip in the data is therefore recognised by the peak of the first flop. The fidelity of a z-flip, further labelled F_z, can be partially quantified by measuring the maximum excitation probability of the first AC Stark flop. If the observed amplitude deviates from 1, this can be partly attributed to an imperfect z-flip in the sequence. The amplitude characterises the z-flip only partially, as other imperfections in the experimental sequence, such as imperfect global rotations at 729 nm, also lead to a deviation of the amplitude from the ideal. The characterisation of the z-flip fidelity is a rough estimate and does not provide the gate fidelity by definition, which would

require a complete method for characterising the gate fidelity, such as quantum process tomography or randomised benchmarking [74]. Nevertheless, key sources of imperfections can be identified. In this experiment, particular attention is paid to the z-flip fidelity F_z at a detuning of $-2.7\,\mathrm{GHz}$, as this detuning will usually be set in future experiments to implement single-qubit gates (see Section 4.1). We are interested in characterising the z-flip fidelity, since this kind of gate occurs in the sequence of a CNOT gate. The implementation of which is an essential part of this thesis. The aim is to estimate the extent to which the fidelity of the CNOT gate will be limited by the z-flip implemented using the far detuned beam path at $393\,\mathrm{nm}$, that was built as part of this master's thesis.

Experimental details for measuring the z-flip fidelity F_z are presented in Section 5.2.1. Section 5.2.2 describes the calibration of input parameters for Model 3 to predict the z-flip fidelity for the present experiment. Section 5.2.1 compares the data to Model 3 and discusses various sources of infidelity.

5.2.1. Measurement of single-qubit z-flip fidelity

The trapping parameters and pulse sequence are identical to that of the experiment in Section 5.1.1 with the following exceptions. First, the third ion (ion 3) is addressed with the AC Stark pulse (previously it was ion 2). Second, the wait time T between the two global rotations is set to $50\,\mu\mathrm{s}$ (previously T was $200\,\mu\mathrm{s}$). In the experiment, the $3^2D_{5/2}$ excitation probability P_D is measured as a function of the AC Stark pulse length τ. Special emphasis is placed on determining the amplitude of the first AC Stark flop, as the amplitude partially quantifies the z-flip fidelity F_z. The pulse length τ is scanned to take enough data points around the first flop. The entire experiment is repeated for five detunings:

$$\Delta = \{-0.40(1), -1.00(1), -2.70(1), -6.00(1), -9.00(1)\}\,\mathrm{GHz}.$$

The detuning is changed by locking the $393\,\mathrm{nm}$ laser on the wavemeter. The intensity of the $393\,\mathrm{nm}$ laser light is adjusted so that the frequency of the AC Stark flops is approximately constant for all detunings. AC Stark flops are measured for this purpose. When the detuning is changed from Δ_1 to Δ_2, the data of the AC Stark flops for Δ_1 are superimposed with the current data for Δ_2. The intensity of the laser signal is adjusted until the two oscillation curves overlap by eye.

Figure 5.8 shows the result of P_D as a function of τ for the addressed ion (ion 3) of the four-ion string at a detuning of $\Delta = -2.7\,\mathrm{GHz}$. Errors are assigned to probabilities according to quantum projection noise (Equation 3.1) and indicated as error bars. Irregular data points were removed as they were known to correspond to events where the ion string melted, leading to irregularities in the data point spacing. The z-flip fidelity F_z is determined by fitting the experimental data with a squared sine function

$$P_D(\tau) = F_z \cdot \sin^2(\delta_{\mathrm{AC}}\tau - \tau_0), \tag{5.21}$$

where δ_{AC} is the frequency of the sine function, which is associated with the AC Stark shift, τ_0 is an offset, and F_z is the amplitude of the sine function. The parameters are determined by fitting the experimental data utilising the Python module *cure_fit* of SciPy. The module allows to set limits for the free parameters and to include the
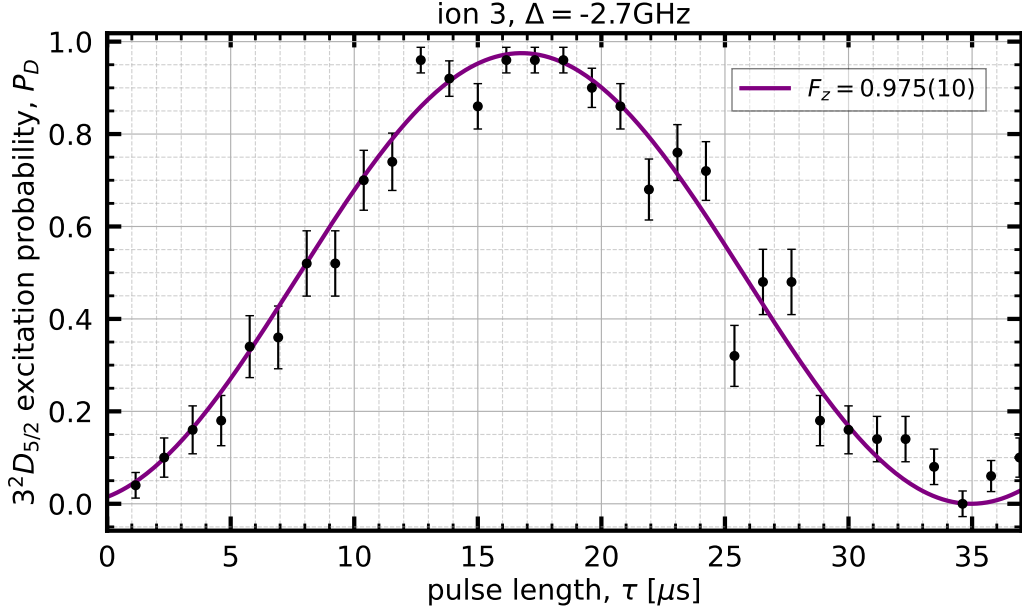
Figure 5.8.: The first AC Stark flop of ion 3 within a four-ion string using the sequence shown in Figure 5.1 with a wait time of $T = 50\,\mu$s. The detuning of the AC Stark pulses is $\Delta = -2.70(1)\,$GHz. Black shapes show data points with error bars. The purple line shows the fit function defined in Equation 5.21. The fit parameters are $F_z = 0.975(10)$, $\delta_{\mathrm{AC}} = 86(1)\,$kHz and $\tau_0 = -0.12(3)$.

statistical uncertainties of the data in order to estimate the uncertainties of the free parameters. The fidelity F_z is limited to 1 for the fitting procedure to ensure physically meaningful results. The errors assigned to probabilities in Figure 5.8 are included in the fitting procedure. For a detuning of $-2.7\,$GHz a fidelity of $F_z = 0.975(10)$ is obtained. The single-qubit z-flip fidelity F_z is determined using this method not only for the data shown here, but for all five detunings. Results are presented in Section 5.2.3.

5.2.2. Calibration: Model 3 applied to z-flips

The next section, which is Section 5.2.3, presents a comparison between the data and the results predicted by Model 3 for the z-flip fidelity. The input parameters, namely Rabi frequency Ω, 393-intensity fluctuations $\delta\Omega/\Omega$, and 729-phase fluctuations $\delta\phi/\delta$, are now defined.

Rabi frequency Ω

Model 3 requires the Rabi frequency Ω as input parameter which is calculated from the detuning Δ and the AC Stark shift δ_{AC} according to Equation 2.43. The selected detunings $\{\Delta_i\} = \{-0.40(1), -1.00(1), -2.70(1), -6.00(1), -9.00(1)\}\,$GHz are known from the wavemeter lock of the 393 nm laser. The first AC Stark flop is measured for each detuning Δ_i as explained in Section 5.2.1. For each of these measurements, the AC Stark shift

$$\delta_{\mathrm{AC}} = \{\delta_{\mathrm{AC},i}\} = \{75(1), 79(1), 86(1), 86(1), 91(1)\}\ \mathrm{kHz} \tag{5.22}$$

is determined by fitting the function in Equation 5.21 to the data. The Rabi frequency Ω_i is determined for each data set according to Equation 2.43, yielding

$$\Omega_i = \{16.2(3), 25.6(2), 43.8(1), 64.6(1), 81.4(1)\} \text{ MHz.} \qquad (5.23)$$

The uncertainties are calculated by error propagation from the uncertainties of the fit parameter $\delta_{\text{AC},i}$. The detuning values are treated as exact.

393-intensity fluctuations $\delta\Omega/\Omega$

In Section 5.1.3 is was shown that including 1% intensity fluctuations in the $393\,\text{nm}$ laser pulses (AC Stark pulses) in the model yielded predictions that are broadly consistent with the data, as presented in Figure 5.6. The same value $\delta\Omega/\Omega = 1\%$ is therefore used here.

729-phase fluctuations $\delta\phi/\phi$

To estimate the 729-phase fluctuations that apply globally to all data sets for the fixed wait time of $T = 50\,\mu\text{s}$, an additional experiment is conducted. In this experiment, the sequence shown in Figure 5.1 is successively repeated for a wait time $T = 50\,\mu\text{s}$ (instead of $T = 200\,\mu\text{s}$). The AC Stark pulse on ion 3 which led to the data in Figure 5.8 is excluded. As such, the effect of the two global $729\,\text{nm}$ pulses in the sequence can be isolated and
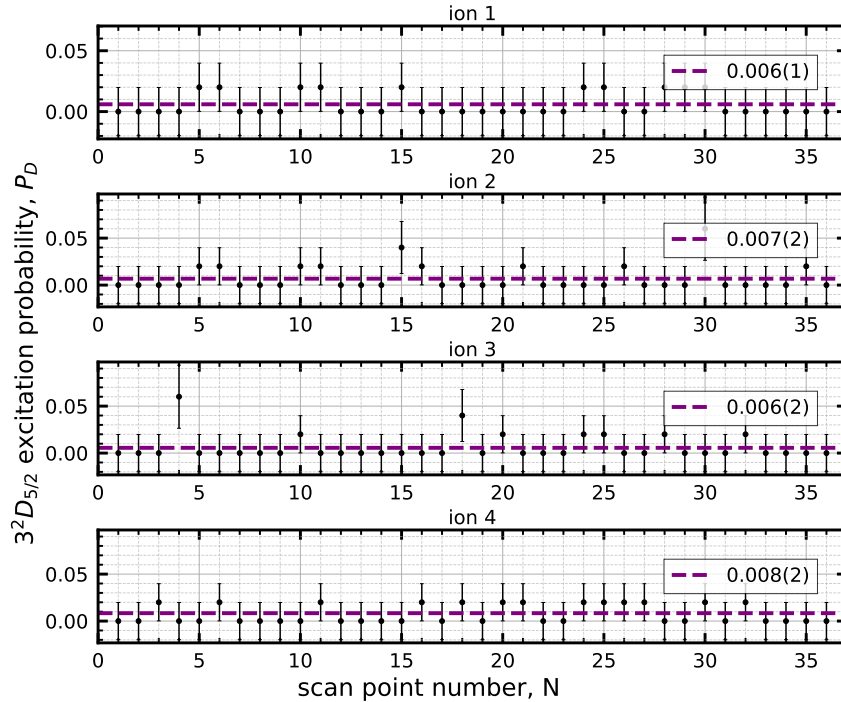

Figure 5.9.: Experimental data using the sequence shown in Figure 5.1 for a wait time $T = 50\,\mu\text{s}$ excluding the AC pulse. The excitation probabilities of the four ions are shown separately as a function of the scan point number. For each scan point the sequence is repeated 100 times (cycles). Dashed purple lines show the average excitation probability. The average with standard error is shown in the legend.

thus also the magnitude of the 729-phase fluctuations can be determined. The data of this experiment is shown in Figure 5.9. The figure shows the excitation probability P_D as a function of the scan point number N. Each scan point results from the repetition and subsequent averaging of the sequence over 100 cycles. The average excitations on all four ions individually are statistically consistent. The average excitation probability over the data of all four ions is $\bar{P}_D = 0.0068(2)$[5]. It is calculated by following the approach in Appendix B.2 that 729-phase fluctuations with $\delta\phi/\phi = 5.3\,\%$ are statistically consistent[6] with the data in Figure 5.9. These phase fluctuations are different from the value found in Section 5.1.4, which is expected, since the experiment here has a $50\,\mu$s wait time between the two global pulses at $729\,$nm, compared to the $200\,\mu$s in the previous experiment.

5.2.3. Comparison of Model 3 with data

Using the input parameters defined in the previous section, Model 3 is used to predict the measured single-qubit z-flip fidelity F_z. To develop some understanding of the relative contribution of the different error sources to infidelity, Figure 5.10 compares the data with various predictions of the model.
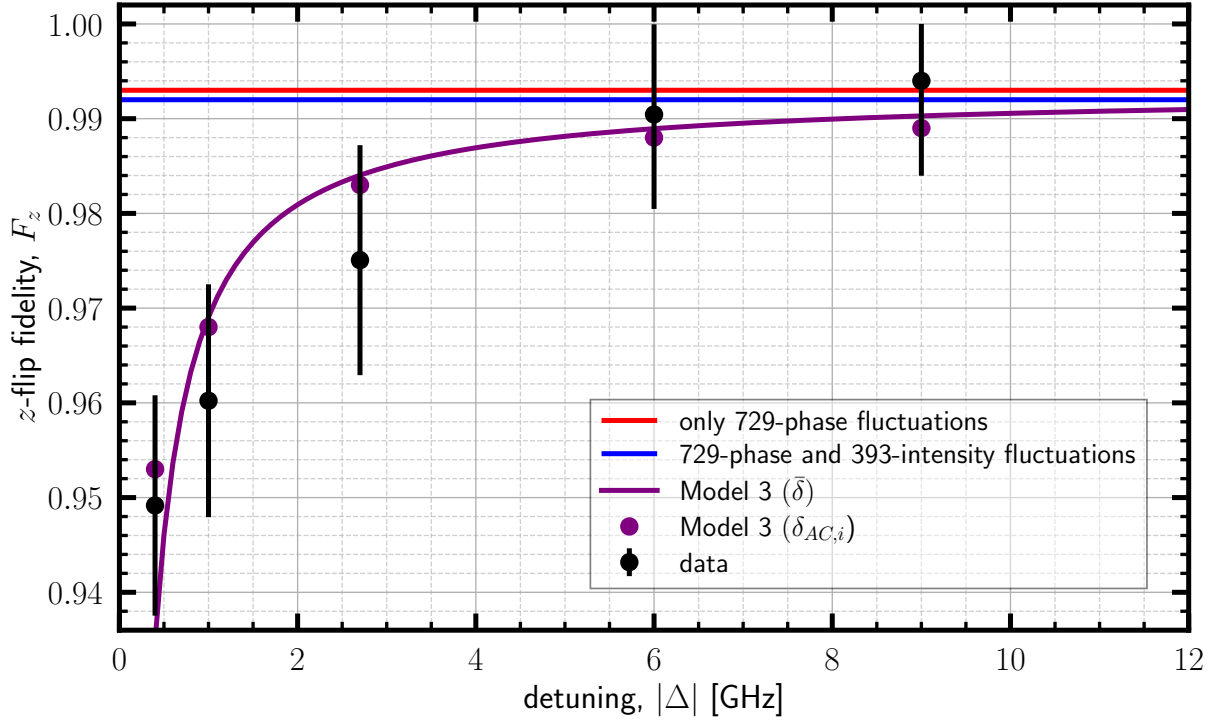

Figure 5.10.: Single-qubit z-flip fidelity as a function of detuning. Black dots with error bars show data points. Lines and purple dots show the prediction of Model 3 under various conditions, in which different error sources are set to zero as explained in the main text. Details on the input parameters for Model 3 are presented in Section 5.2.2.

---

[5]Ideally the excitation probability of each ion should be zero.
[6]Phase fluctuations of $\delta\phi/\phi = 5.3\,\%$ lead to an excitation probability of $P_D = 0.0068$.

The purple dots in Figure 5.10 show the prediction of the full Model 3 for the AC Stark shifts $\delta_{\mathrm{AC},i}$ defined by the detunings Δ_i, Rabi frequencies Ω_i, $\delta\Omega/\Omega = 1\,\%$ and $\delta\phi/\phi = 5.3\,\%$, as described in Section 5.2.2. The full model successfully predicts the change in F_z as a function of the detuning Δ of the 393 nm laser from the $4^2S_{1/2}$ to $4^2P_{3/2}$ transition. Since the only part of the model that depends on the detuning is the 5-level spontaneous scattering, I conclude that the 5-level system accurately describes the scattering dynamics. The experiment approximately maintained a constant frequency of AC Stark flops, which is the AC Stark shift (Equation 5.21), by adjusting the intensity of the AC Stark pulses for all detunings. The purple line shows the prediction of Model 3 using a detuning-independent AC-Stark shift of $\bar{\delta} = 83(1)\,\mathrm{kHz}$ equal to the average AC Stark shift over all detunings (average of the values in Equation 5.22). The average AC Stark shift is used to calculate the Rabi frequency $\Omega = \sqrt{4|\Delta|\bar{\delta}}$ over different detunings. These Rabi frequencies are then used as input parameters in the model. The purple line serves as a guide to understand how the fidelity scales with detunings that were not measured in the experiment. The average AC Stark shift $\bar{\delta}$ is further used to introduce two additional theory lines, which are now described.

The blue line in Figure 5.10 shows the prediction of Model 3 (using the average AC Stark shift) under the assumption that there is no spontaneous scattering, i.e. the master equation defined in Equation 5.7 used in the simulation is reduced to its coherent part. 393-intensity fluctuations and 729-phase fluctuations are still included. It can be seen that 393-intensity fluctuations and 729-phase fluctuations together impose a constant infidelity that limits F_z. In Figure 5.10, the red line represents Model 3 (average AC Stark shift), which only includes 729-phase fluctuations. To achieve this, the simulation turns off intensity fluctuations by setting $\delta\Omega$ to zero. The comparison of the three theory lines shows that intensity fluctuations make the smallest contribution to infidelity. Phase fluctuations set an upper limit of the fidelity. The infidelity due to spontaneous scattering strongly depends on the detuning.

Understanding the absolute value and various sources of infidelity to F_z at a detuning of $\Delta = -2.7\,\mathrm{GHz}$ is particularly important in this work. This detuning will typically be used in future experiments implementing single-qubit gates via the AC Stark effect to achieve ion-photon entanglement generation and a universal gate set in our experimental setup (see Section 4.1). The measured single-qubit z-flip fidelity at a detuning of $-2.7\,\mathrm{GHz}$ is $F_z = 0.975(10)$. The value is statistically consistent with the prediction of Model 3, which is $F_z = 0.983$ (purple dots, Figure 5.10). The predicted infidelity is 0.017, calculated as $1 - 0.983$. The infidelity predicted by the model is determined in approximately equal parts by spontaneous scattering (0.009) and 729-phase fluctuations (0.007).

5.3. Summary

AC Stark flops on a single-ion out of a four-ion string were measured using the new far detuned 393 nm beam generate in the setup shown in Figure 4.1. Various models with increasing complexity were developed to explain the imperfections in the data. A model of spontaneous scattering in a five-level system alone was not sufficient to explain the damping rate observed in the data of AC Stark flops. Next, the model was extended to include intensity fluctuations of the AC Stark pulses. Specifically a model of Gaus-

sian distributed fluctuations of 1% in the Rabi frequency was introduced. The extended model that includes both spontaneous scattering and intensity fluctuations qualitatively agrees with the observed damping rate. However, the model predicted a higher amplitude of the first AC Stark flop. In the data, the first AC Stark flop was identified with the implementation of a single-qubit z-flip. The z-flip is of particular interest for implementing a CNOT gate using our native gates. We therefore extended our model to also include another known error source namely phase fluctuations in the 729 nm laser. The prediction of the model shows that phase fluctuations reduce the contrast of the AC Stark flops by a constant fraction. The full model, which includes spontaneous scattering, intensity fluctuations of the AC Stark pulses at 393 nm, and phase fluctuations of the 729 nm laser, aligns best with the AC Stark flop data. Finally, in a second experiment the single-qubit z-flip fidelity F_z was measured as a function of detuning and compared to the prediction of the model. At a detuning of -2.7 GHz of the AC Stark pulses the fidelity was determined from experimental data, yielding $F_z = 0.975(10)$. The fidelity is predicted by the model, yielding $F_z = 0.983$, which is statistically consistent with the data. Approximately half of the infidelity is caused by 729-phase fluctuations, while the other half is due to spontaneous scattering at the particular detuning. Intensity fluctuations of the AC Stark pulses contribute only a negligible fraction to the infidelity.

6. Realisation of a CNOT gate and a long-lived quantum memory

Chapter 5 of this master's thesis has demonstrated that the new setup for generating a -2.6 GHz detuned beam path at 393 nm can be used to implement single-ion focussed phase rotations via the AC Stark effect. Single-ion phase rotations at 393 nm, combined with the global rotations and the MS gate at 729 nm presented in Chapter 3, complete a universal gate set in our trapped-ion quantum network node. This chapter presents the results of the second goal of this thesis, which is the implementation and application of a CNOT gate using the universal gate set. Section 6.1 presents the gate sequence of the CNOT gate and an overview of the common experimental settings for the four experiments presented in Sections 6.2 to 6.5. Section 6.2 presents the measurement of a logical truth table to demonstrate that the gate sequence presented in Section 6.1 implements a CNOT gate. The truth table fidelity is calculated to provide justification. Section 6.3 characterises the CNOT gate fidelity by quantum process tomography (QPT). The CNOT gate can be used to map a qubit encoded in one physical ion, into a decoherence-free subspace (DFS) formed by entangled states of two ion-qubits. One state in the DFS is the maximally entangled Bell state $|\psi^+\rangle$. In Section 6.4, the lifetime of the Bell state $|\psi^+\rangle$ is investigated by measuring its fidelity decay as a function of time. It is further demonstrated that encoding the Bell state $|\psi^+\rangle$ in the ground state manifold $4^2S_{1/2}$ significantly increases its lifetime. In Section 6.5, the process of storing and retrieving a single-qubit state from a DFS formed by entangled states encoded in the ground state manifold is characterised by QPT for a storage time of 500 ms.

6.1. Implementation of the CNOT gate

Section 6.1.1 presents the gate sequence used to implement a CNOT gate using the universal gate set available in our ion trap system. Section 6.1.2 defines the common experimental details used for the experiments throughout the chapter.

6.1.1. Gate sequence

A new algebra is introduced to clearly represent the CNOT gate sequence. The algebra refers to a notation for global rotations around the x-axis labelled $R_x(\theta)$, and for single-qubit y-rotations $R_y^{(i)}(\theta)$ on ion-qubit i with corresponding rotation angle θ. Global rotations around the x-axis are defined in Equation 2.19, which is reproduced here

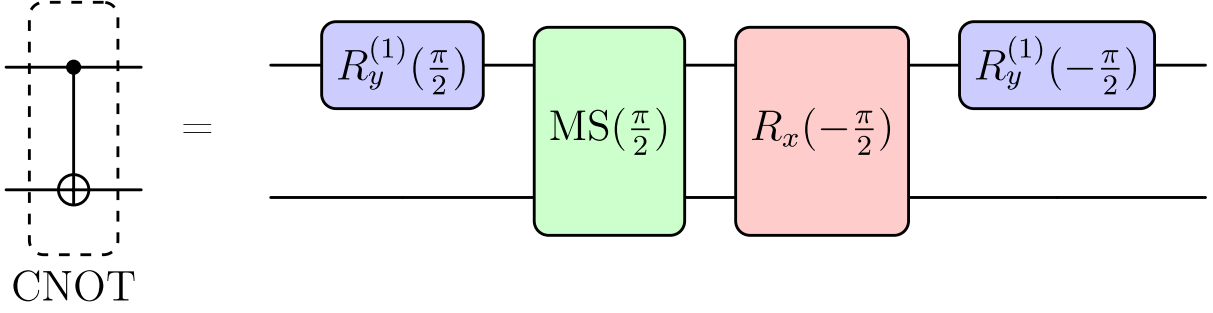$$R_x(\theta) = R(\theta, \phi = 0). \tag{6.1}$$

Figure 6.1.: CNOT gate sequence consisting of single-qubit rotations around the y-axis of the Bloch sphere $R_y^{(1)}$ (Equation 6.2) of the control qubit, global rotations of control and target qubit around the x-axis of the Bloch sphere R_x (Equation 6.1), and a Mølmer-Sørenson gate MS (Equation 3.7).

These global rotations are implemented using 729 nm laser light with a laser phase of $\phi = 0$. Single-qubit y-rotations $R_y^{(i)}(\theta)$ on ion-qubit i in a string are realised with the following sequence of three pulses:

$$R_y^{(i)}(\theta) = R\left(-\frac{\pi}{4}, \frac{\pi}{2}\right) R_z^{(i)}(\pi) R\left(\frac{\pi}{4}, \frac{\pi}{2}\right), \tag{6.2}$$

where $R_z^{(i)}(\pi)$ is a single-qubit z-flip that was introduced in Section 5.2 as an AC Stark pulse (Equation 3.3) at 393 nm on ion-qubit i. Figure 6.1 shows the CNOT gate sequence decomposed in our universal gate set.

6.1.2. Experimental details

In this section, essential experimental details applicable to the experiments discussed in Sections 6.2, 6.3, 6.4 and 6.5 are presented. The section is divided into three parts: Experimental system, Calibration and Experimental procedure, which each provide a schematic overview of the experimental tasks involved in working with the CNOT gate.

Experimental system

The experimental system consists of a string of two ^{40}Ca$^+$ ions. The ions are trapped with an axial confinement of $\omega_z = 2\pi \times 1$ MHz. The physical qubit is encoded in the two Zeeman states $|S\rangle = |4^2S_{1/2}, m_j = -1/2\rangle$ and $|D\rangle = |3^2D_{5/2}, m_j = -5/2\rangle$. The logical qubit states $|0\rangle$ and $|1\rangle$ are identified with $|S\rangle$ and $|D\rangle$, respectively. Global rotations $R(\theta, \phi)$ and the MS gate are implemented using the axial 729-beam that is shown in Figure 3.2. Single-qubit gates are implemented using AC Stark pulses at 393 nm generated in the optical setup presented in Figure 4.1. In the beginning of each experiment, the ions are initialised in the ground state $|S\rangle$ by optical pumping. Doppler cooling and subsequent sideband cooling prepares the ion string in the motional ground state of the axial centre-of-mass mode. Final state detection is performed using electron shelving.

Calibration

Setting up the CNOT gate requires precise calibration of several parameters. For the global rotation $R_x(\pi/2)$ around the x-axis the $\pi/2$-time ($t_{\pi/2}$) must be calibrated. The $\pi/2$-time defines the interaction time of the 729 nm laser with the ions in the string that is required to achieve a rotation angle $\theta = \Omega \cdot t_{\pi/2} = \pi/2$, where Ω is the Rabi frequency of the qubit transition. Within the calibration procedure, the $\pi/2$-time is first roughly estimated by measuring Rabi flops on the qubit transition. Then, four consecutive $\pi/2$-pulses are applied to the ions while scanning the $\pi/2$-time around the value obtained from a simple sinusoidal fit to the Rabi flops. The excitation probability P_D of the state $|D\rangle$ on both ions is determined by electron shelving. The result is a measurement of P_D as a function of $t_{\pi/2}$. After four consecutive $\pi/2$-pulses, P_D is ideally zero. The $\pi/2$-time results from a fit to find the minimum of the obtained curve.

Since the single-qubit y-rotation $R_y^{(1)}(\pi/2)$ includes global rotations $R(\pm\pi/4, \pi/2)$, the $\pi/4$-time ($t_{\pi/4}$) must be calibrated. The calibration is achieved trough a similar procedure, but with eight consecutive $\pi/4$ pulses while scanning the time. In addition, the single-qubit y-rotation includes a single-qubit z-flip $R_z^{(i)}(\pi)$, implemented by an AC Stark pulse generated in the setup presented in Section 4.2. The rotation angle $\theta = \delta_{\mathrm{AC}} t_\pi^{(i)} = \pi$ is defined by the AC Stark shift δ_{AC} and the AC Stark pulse length $t_\pi^{(i)}$ referred to as the addressed π-time. The addressed π-time is initially estimated by measuring AC Stark flops and calibrated more precisely by using the sequence presented in Figure 5.1 with two consecutive AC Stark pulses of length $\tau = t_\pi^{(i)}$ while scanning τ. The wait time between the global pulses in the sequence is not fixed for this experiment. The wait time is equal to the length of the two consecutive AC Stark pulses. This means that the pulses in the sequence are all applied directly one after the other. The value is again found at the minimum of the resulting curve. Precise calibration of the global $\pi/2$- and $\pi/4$-times, as well as the addressed π-time, is important to ensure high-fidelity gates in the CNOT-sequence presented in Figure 6.1. Due to potential magnetic field and laser fluctuations, re-calibration of π-times is necessary over extended experimental duration.

A central component of the CNOT gate is the entangling MS gate. The calibration of the gate [75] is complex and a detailed description of the entire procedure does not fit within the scope of this master's thesis. In the experiments presented here, the MS gate is setup with 7.5 kHz detuning from the motional sidebands and no centre-line detuning [76]. The gate time is 123 μs.

Experimental procedure

All experiments in Section 6.2, 6.3, 6.4 and 6.5 are structured in the same way. Rotations are applied to both qubits to prepare a two-qubit input state $|c, t\rangle$, where $|c\rangle$ is the control qubit and $|t\rangle$ is the target qubit of the CNOT gate. The target qubit $|t\rangle$ is flipped, if the control qubit $|c\rangle$ is in the logical eigenstate $|1\rangle = |D\rangle$. In each experiment, specific input states are chosen depending on the purpose of the experiment. Finally, the logical output states of the two individual ions are determined by electron shelving readout. The fluorescence light of the ions is simultaneously imaged onto the PMT and the CCD camera. Electron shelving enables projective measurements in the computational basis $\{|0\rangle, |1\rangle\}$. However, for quantum process and state tomography, it is required to measure

the expectation values of all three Pauli operators, $\sigma_i = (\sigma_x, \sigma_y, \sigma_z)$, as explained in Section 2.3. The expectation values of σ_x and σ_y are measured by applying global rotations to the qubits before electron shelving that map the eigenvectors of σ_x and σ_y to those of σ_z:

$$\sigma_z = R\left(\frac{\pi}{2}, \pi\right) \sigma_y R^\dagger \left(\frac{\pi}{2}, \pi\right) \tag{6.3}$$

$$\sigma_z = R\left(\frac{\pi}{2}, \frac{3\pi}{2}\right) \sigma_x R^\dagger \left(\frac{\pi}{2}, \frac{3\pi}{2}\right). \tag{6.4}$$

Each subsequent section in this chapter, which introduces a new experiment, commences with specific details not covered here.

6.2. Measurement of the logical truth table

In order to verify that the gate sequence shown in Figure 6.1 implements a CNOT gate (Equation 2.22), a logical truth table is measured. In the experiment, the CNOT gate is applied to each computational basis state: $|c, t\rangle = \{|00\rangle, |01\rangle, |10\rangle, |11\rangle\}$, where $|0\rangle = |4^2 S_{1/2}, m_j = -1/2\rangle$ and $|1\rangle = |D\rangle = |3^2 D_{5/2}, m_j = -5/2\rangle$. Over $N = 100$ cycles the logical states of the two individual output ion-qubits are determined using the PMT signal. For each measurement cycle, each ion-qubit is either found in the bright state, 0, or the dark state, 1. The result, bright or dark ion, is stored in a 2×100 matrix, which contains a binary representation (0,1) of the states of the ion-qubits. Then the conditional probabilities

$$p_{ij} = \frac{n_{ij}}{N} \tag{6.5}$$

are determined, where i is the logical state of ion 1, j that of ion 2 and n_{ij} is the number of events in which ion 1 is in i and ion 2 is in j within N cycles. The analysis is repeated for all four input states, i.e. for each input state four conditional probabilities $\{p_{00}, p_{01}, p_{10}, p_{11}\}$ representing the population of the four computational basis states after the CNOT gate are determined.

The upper truth table in Figure 6.2 shows the measured population of all computational basis states after applying the CNOT gate to each of the computational basis states. The lower truth table in Figure 6.2 shows the ideal. The truth table fidelity [77] of the measured truth table U_{exp} with the ideal U_{ideal}

$$F = \frac{1}{4} \operatorname{tr}(U_{\mathrm{exp}} U_{\mathrm{ideal}}) = 87.5(3)\% \tag{6.6}$$

reveals the average performance of the CNOT gate when applied to the computational basis states. The infidelity is determined by the infidelity of the gate sequence as well as State Preparation and Measurement (SPAM) errors. No systematic study of the SPAM errors was carried out in this work. A discussion on errors is presented in Section 6.3.
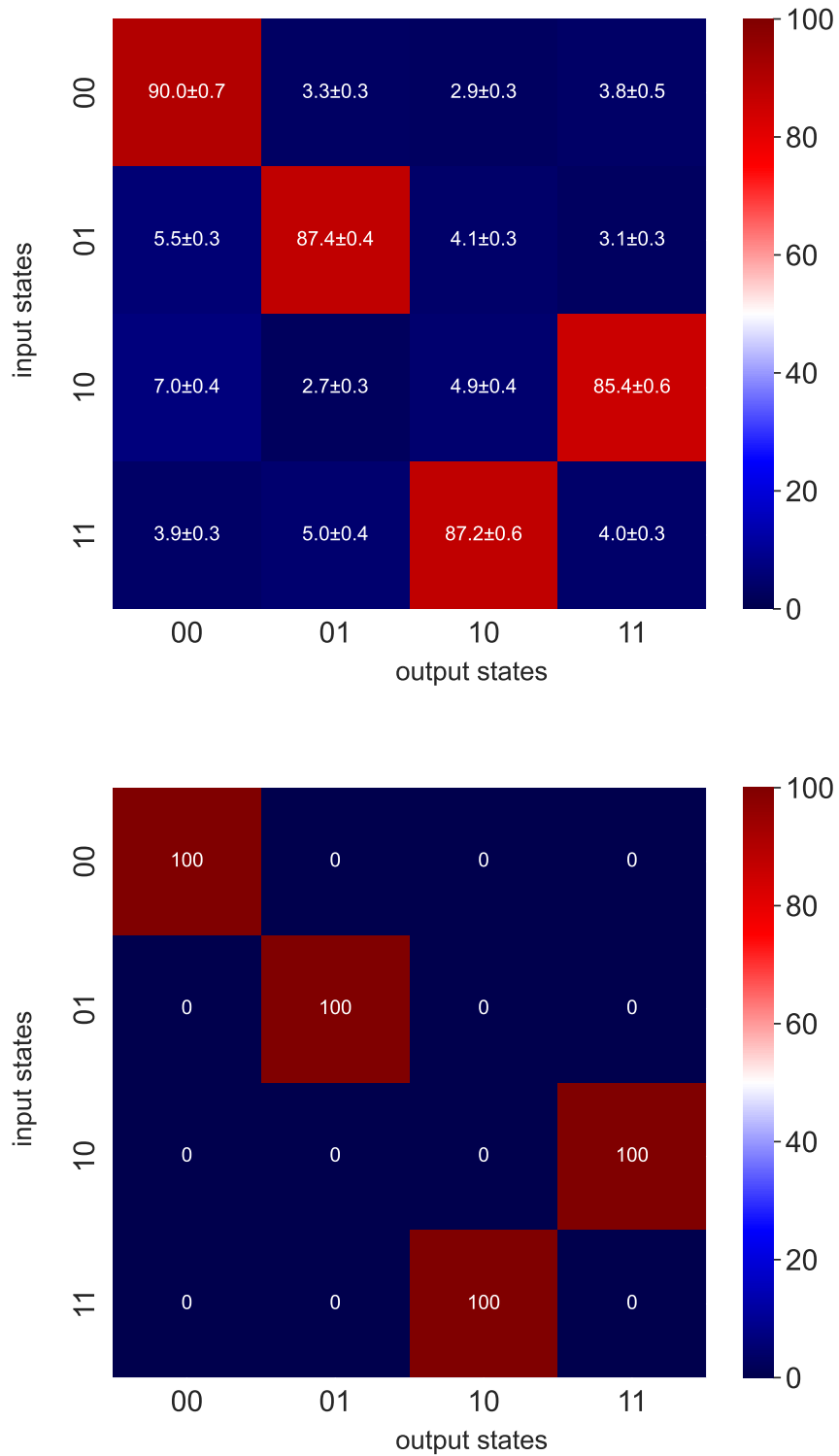
Figure 6.2.: Top: Measured truth table U_{exp} of the CNOT gate. Table entries show the population of the computational basis states after the CNOT gate as defined in Equation 6.5 including statistical errors. Bottom: Ideal truth table U_{ideal} of the CNOT gate.

6.3. Process tomography of the CNOT gate

This experiment fully characterises the CNOT gate implemented by the gate sequence shown in Figure 6.1 by quantum process tomography (QPT). Section 2.3 provides an overview of the concept of QPT, which is necessary to understand the experimental results presented here. The analysis code[1] for QPT is written in Python and uses the functions of the open source library *Forest Benchmarking* [78] for QPT. The maximum likelihood approach for QPT [79] is used to calculate the process matrix χ. To quantify the gate performance, the process fidelity F_p (Equation 2.34) and the average gate fidelity $\bar{F}$ (Equation 2.35) are calculated.

6.3.1. Experimental details

Figure 6.3 shows the experimental sequence that is used for QPT of the CNOT gate. The state $|c\rangle$ is the control qubit, and $|t\rangle$ the target qubit. QPT of the CNOT gate requires to feed in 16 linearly independent logical input states to the gate as introduced in Section 2.3. The input states $|c, t\rangle$ used in the experiment are presented in Table 6.1. Each two-qubit output state is determined by QST, which requires measurements in nine different product bases (Section 2.3) yielding $16 \cdot 3^2 = 144$ individual expectation values. Each basis measurement $\sigma_i \sigma_j$ with $i, j \in \{x, y, z\}$ is repeated 120 times and averaged for all 16 input states. The data is used to calculate the process matrix and to reconstruct the density matrices of the output states.
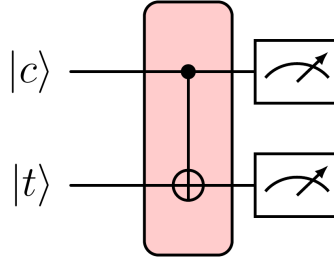

Figure 6.3.: Experimental sequence for QPT of the CNOT gate. The control qubit is denoted as $|c\rangle$, the target qubit as $|t\rangle$. The CNOT gate is applied to 16 linearly independent input states $|c, t\rangle$ summarised in Table 6.1. The output state is measured in nine different bases.

$|DD\rangle$	$|DS\rangle$	$|D+i\rangle$	$|D+\rangle$
$|SS\rangle$	$|SD\rangle$	$|S+i\rangle$	$|S+\rangle$
$|+D\rangle$	$|+S\rangle$	$|++\rangle$	$|+-i\rangle$
$|+iD\rangle$	$|+iS\rangle$	$|+i+\rangle$	$|+i+i\rangle$

Table 6.1.: Input states $|c, t\rangle$ used for QPT of the CNOT gate. The states $|+\rangle$ and $|\pm i\rangle$ are defined in Section 2.1.

---

[1]The code was developed by James Bate with input from Tabea Stroinski in connection with this master's project. The code is not publicly available.

6.3.2. Result: Process and average gate fidelity

Figure 6.4 shows the measured process matrix of the CNOT gate. Figure 6.5 shows the ideal process matrix. The process fidelity according to Equation 2.34 with the ideal process matrix is $F_p = 0.76(2)$. The error of the process fidelity is calculated using Monte Carlo simulation of the data. The state fidelity between each ideal output state ρ after the CNOT gate and the measured reconstructed state σ is calculated according to Equation 2.14. Errors of the state fidelity are again calculated using Monte Carlo simulation of the data. The average gate fidelity $\bar{F}$ is calculated as the average output state fidelity over the topographically completed set of input states as defined in Equation 2.35, yielding $\bar{F} = 0.88(2)$ with standard deviation.
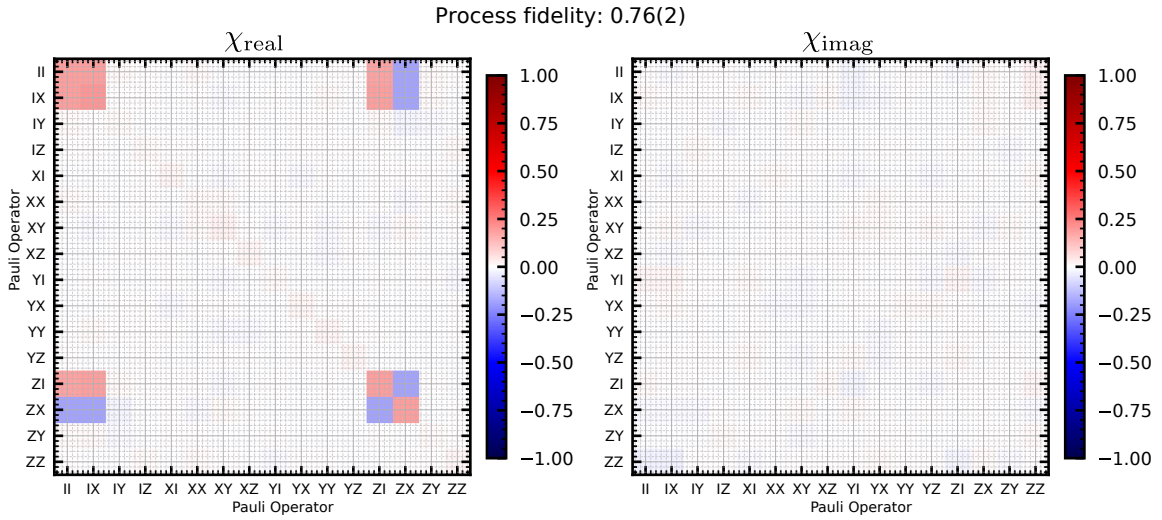

Figure 6.4.: Measured process matrix of the CNOT gate. The real parts χ_{real} of the process matrix are shown on the left, imaginary parts χ_{imag} on the right. The absolute values of the imaginary parts are all less than 0.026.
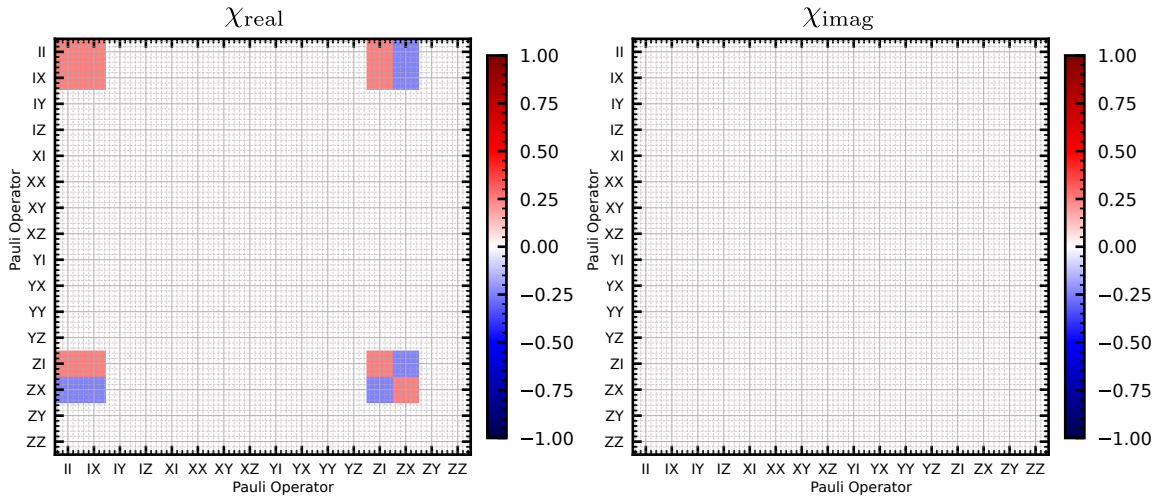

Figure 6.5.: Ideal process matrix of the CNOT gate. The real parts χ_{real} are shown on the left. The imaginary parts χ_{imag} shown on the right are zero.

The infidelity of the CNOT gate is attributed to imperfections of the individual gates in the CNOT gate sequence shown in Figure 6.1. The main contributions to infidelity are single-qubit rotations and the MS gate. Recall the decomposition of the single-qubit y-rotation that is included in the CNOT gate sequence:

$$R_y^{(i)}(\theta) = R\left(-\frac{\pi}{4}, \frac{\pi}{2}\right) R_z^{(i)}(\pi) R\left(\frac{\pi}{4}, \frac{\pi}{2}\right). \tag{6.7}$$

The gate is defined by a single-qubit z-flip $R_z^{(i)}(\pi)$ on ion-qubit i, implemented using laser light at 393 nm that is detuned by -2.7 GHz from the $4^2S_{1/2}$ to $4^2P_{3/2}$ transition, that is enclosed by two global rotations at 729 nm. In Section 5.2, a single-qubit z-flip was partially characterised by embedding the gate in a Ramsey experiment to map the phase rotation to populations in the qubit states (Equation 5.20). It was measured that the fidelity of the single-qubit z-flip is 0.975(10). The measured fidelity can serve as an estimate for the fidelity of the single-qubit y-rotation in the CNOT gate. This is because the gate characterised in Section 5.2 is similar to the single-qubit y-rotation, with the exception that the two global rotations contain different angles and phases. The fidelity of the single-qubit y-rotation is limited by spontaneous scattering during the AC Stark pulse and phase fluctuations of the 729 nm laser. The infidelity due to spontaneous scattering can be assumed to be equivalent to the observation in Section 5.2 because in both experiments the detuning was set to -2.7 GHz. According to the model in Section 5.2.3, the infidelity resulting from spontaneous scattering at a detuning of -2.7 GHz is predicted to be 0.009. Therefore, it can be concluded that the fidelity of the single-qubit y-rotation is limited to a maximum of $F_y = 0.991$. The infidelity due to phase fluctuations in the 729 nm laser cannot be directly compared because of the different angles and phases of the global rotations in the single-qubit y-rotation. The most dominant component to infidelity of the CNOT gate is the MS gate. The MS gate achieved a fidelity[2] of $F_{\text{MS}} = 0.947(6)$, as shown in Appendix C.1. Currently, there is insufficient understanding to fully explain the infidelity of the MS gate. The most convincing explanation thus far is the instability of the 729 nm laser. The upper bound of the CNOT gate fidelity is estimated by multiplying the fidelity estimate of each individual gate in the sequence in Figure 6.1. The assumed gate fidelities are not gate fidelities by definition. Instead, the fidelities partially quantify with which fidelity the gate prepares a particular state. Assuming ideal global rotations ($F = 1$) in the CNOT gate sequence, the fidelity of the single-qubit y-rotation ($F_y = 0.991$) and the MS gate ($F = 0.947(6)$) presented here, indicate that the upper limit of the CNOT gate fidelity is given by

$$F_{\text{CNOT}} = 0.991 \times 0.947(6) \times 1 \times 0.991 = 0.930(6) \tag{6.8}$$

The estimated fidelity of the CNOT gate is not significantly different from the measured average gate fidelity $\bar{F} = 0.88(2)$.

As presented in Section 2.3, the process fidelity and average gate fidelity are related through Equation 2.36. Given a process fidelity of $F_p = 0.76(2)$, an average gate fidelity of $\bar{F}_{\text{theo}} = 0.808(2)$ is expected. We measured an average gate fidelity of $\bar{F} = 0.88(2)$. The

---

[2]The fidelity is not a gate fidelity by definition, but the state fidelity with which the MS gate can prepare a maximally entangled state.

experimental results show a 8(2)% discrepancy between the expected and the measured average gate fidelity which is statistically significant ($> 3\sigma$). In reference [80], the authors also encounter a discrepancy between process and average gate fidelity. They calculate the process fidelity defined in Equation 2.34 resulting in $F_p = 0.87$. No error is calculated. From this, they expect an average gate fidelity of $\bar{F} = 0.90$. However, their experimental data yields an actual average gate fidelity of $\bar{F} = 0.96(3)$. The values are statistically consistent in their case. They propose an approach of calculating the process fidelity „directly from a 71-element subspace of the tomographic data" [80]. With this method, the authors are able to match the obtained values of process and average gate fidelity more closely. The method is not described in detail and no theoretical references are given. Based on the limited information provided in the paper, for our experiment it is suspected that the discrepancy is due to imperfect preparation of the input states and analysis of the output states which are directly related to the fluctuations of the 729 nm laser. Further investigations are planned once the problems with the fluctuations of the laser are overcome with a planned new laser system.

6.4. Preparation of entangled states in a decoherence-free subspace

In our experimental setup the coherence time of a qubit is to a large amount limited by dephasing due to magnetic field and laser fluctuations that couple equally to all ions trapped. Considering a two-ion string in an environment that has the same coupling to both ions, a co-trapped ion can be used to encode a single-qubit state into a decoherence-free subspace (DFS) formed by entangled states, which protects the single-qubit state from collective dephasing, as discussed in Section 2.5. This section aims to characterise the decay with time of the fidelity of entangled states in the DFS that are prepared using the CNOT gate. Consequently, the fidelity decay as a function of time is used to determine the effective lifetime of the states. In particular, the entangled Bell state $|\psi^+\rangle = 1/\sqrt{2}(|SD\rangle + |DS\rangle)$ which is one of the basis states that is used to span a two-dimensional decoherence-free Hilbert space, is characterised. In Section 6.4.1, the lifetime of the state $|\psi^+\rangle$ is measured and compared with the fundamental limit imposed by the lifetime of the $3^2D_{5/2}$ manifold due to spontaneous emission. In Section 6.4.2 it is demonstrated that encoding the Bell state in the ground state manifold $4^2S_{1/2}$ significantly enhances the lifetime.

6.4.1. Lifetime in a decoherence-free subspace

The experimental sequence to measure the lifetime of the Bell state

$$|\psi^+\rangle = U_{\mathrm{CNOT}} |+D\rangle = \frac{1}{\sqrt{2}}(|SD\rangle + |DS\rangle), \tag{6.9}$$

where U_{CNOT} is the unitary matrix of the CNOT gate (Equation 2.22), is shown in Figure 6.6. The input states of control and target qubit are $|+\rangle$ and $|D\rangle$. The experimentally prepared output state $\rho_{\mathrm{out}}(T)$, which ideally equals $|\psi^+\rangle \langle \psi^+|$, is fully characterised via
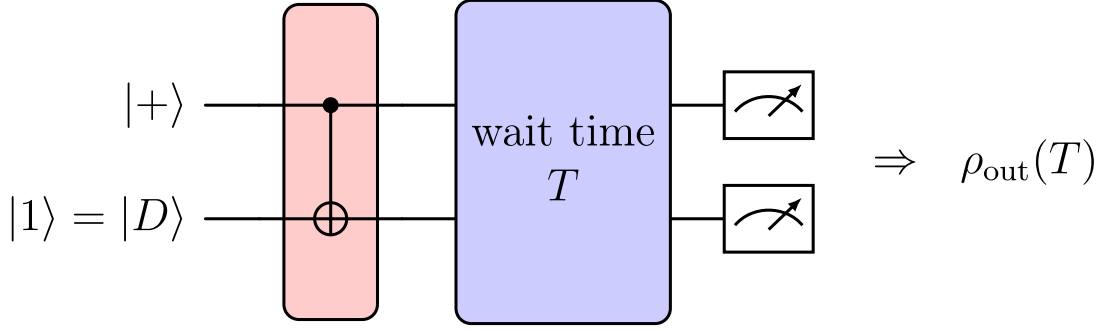
Figure 6.6.: Experimental sequence to measure the lifetime of the entangled Bell state $|\psi^+\rangle$ given in Equation 6.9. The state $|\psi^+\rangle$ is prepared by applying the CNOT gate to the input state $|+, D\rangle$. A variable wait time T is introduced after the state preparation. The output state $\rho_{\text{out}}(T)$ is measured after the wait time.

QST for various wait times T. The fidelity F between the measured quantum state and the ideal state $|\psi^+\rangle\langle\psi^+|$ is calculated according to Equation 2.14 for no wait time $T = 0$. Within the wait time, any magnetic field gradient across the two-ion string leads to a linear evolution over time of the relative phase $\alpha(T) = \Delta E T/\hbar$ between $|SD\rangle$ and $|DS\rangle$ [38], where ΔE is the difference between the energy splitting of the two ions. The Bell state $|\psi^+\rangle$ evolves as:

$$|\psi^\alpha\rangle = \frac{1}{\sqrt{2}}\big(|SD\rangle + e^{i\alpha(T)}|DS\rangle\big). \tag{6.10}$$

To account for the phase evolution, the fidelity for non-zero wait times is calculated as the maximum overlap between the experimentally observed density matrix $\rho_{\text{out}}(T)$ and the state $|\psi^\alpha\rangle$, such that

$$F = \max_\alpha\big(\langle\psi^\alpha|\rho_{\text{out}}(T)|\psi^\alpha\rangle\big). \tag{6.11}$$

Figure 6.7 displays the reconstructed density matrix $\rho_{\text{out}}(T = 0)$ for zero wait time. The density matrix $\rho_{\text{out}}(T = 1\,\text{s})$ after a wait time of $T = 1\,\text{s}$ is presented in Figure 6.8. The state fidelity of the two reconstructed states drops within the wait time of $T = 1\,\text{s}$ from 0.88(1) to 0.41(4). The errors of the fidelities are calculate from Monte-Carlo sampling. To verify that the state is still entangled after a wait time of 1 s, the concurrence was calculated according to Equation 2.29. The concurrence for the reconstructed state $\rho_{\text{out}}(T = 1\,\text{s})$ is $C = 0.39(9)^3$, which is statistically above zero and indicates that the state is still entangled. Comparing the density matrices in Figure 6.7 and Figure 6.8 clearly shows that after 1 s, the population in the ground state $|S\rangle$ significantly increased, which is attributed to spontaneous scattering from the $|D\rangle$ state to the ground state. To confirm that the measured fidelity decay is a result of the fundamental lifetime limit $\tau_D = 1.168(7)\,\text{s}$ [43] of the $3^2D_{5/2}$ manifold, the state fidelity is measured for two additional wait times which are $T = 100\,\text{ms}$ and $T = 500\,\text{ms}$. The density matrices for these wait times are not shown. The measured fidelity as a function of wait time is presented in Figure 6.9 and compared with a model that is described below.

---

[3]The concurrence is calculated for each density matrix from the Monte Carlo simulation. The standard deviation of the sample is given here as the error of the concurrence. A possible asymmetry of the distribution [66], i.e. if the distribution is not centred around the value $C = 0.39(9)$, is not taken into account.
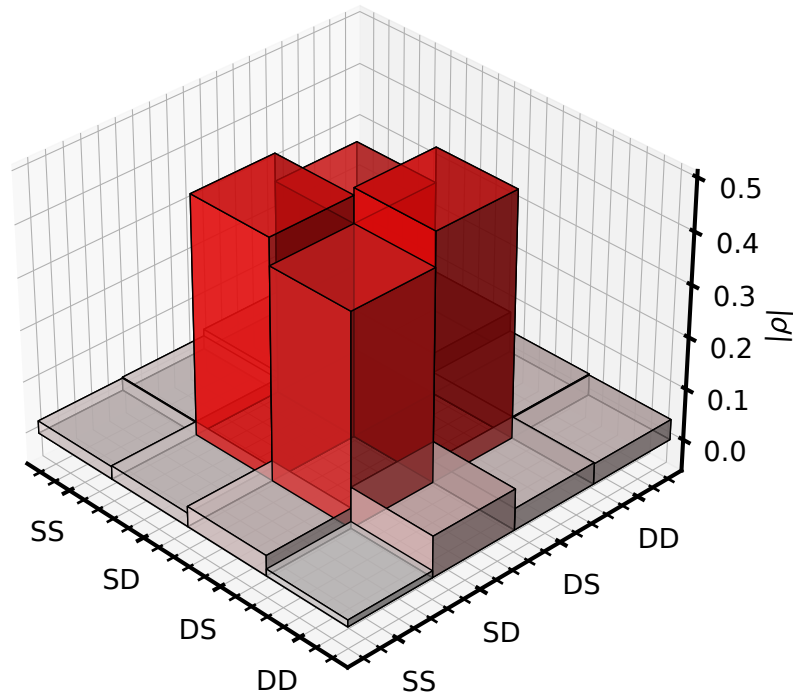
Figure 6.7.: Absolute values of the reconstructed density matrix of the output state $\rho_{\text{out}}(T = 0)$ measured using the sequence shown in Figure 6.6. The state fidelity $F = 0.88(1)$ is obtained with the ideal state $|\psi^+\rangle \langle \psi^+|$ according to Equation 6.9.
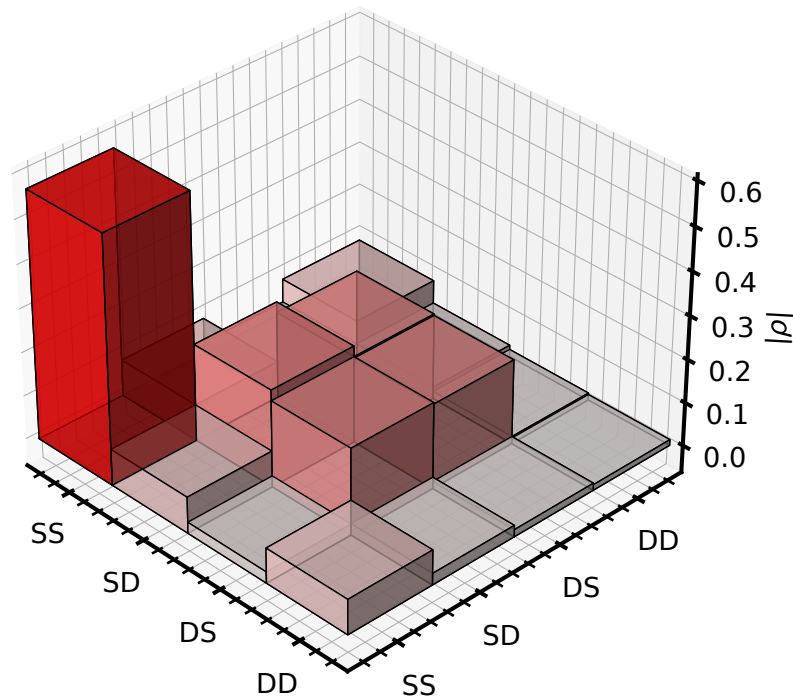

Figure 6.8.: Absolute values of the reconstructed density matrix $\rho_{\text{out}}(T = 1\,\text{s})$. The state fidelity with the ideal is $F = 0.41(4)$ according to Equation 6.11.

Modelling spontaneous scattering in a two-level atom coupled to the vacuum

The model is based on the master equation formalism presented in Section 5.1.2, but is greatly simplified compared to the five-level system approach presented so far. The model presented here describes the effect of spontaneous scattering in a two-level system, consisting of $|S\rangle$ and $|D\rangle$, that is coupled to vacuum. In particular, there is no laser-ion interaction involved in the model. The fidelity F_{sim} of the state $|\psi^+\rangle$ is predicted by the model for a various wait times T. The simulation code is subdivided as follows.

1. **Initialisation**: The density matrix of the initial state is defined as the experimentally observed density matrix $\rho_{\text{out}}(T = 0\,\text{s})$ for no wait time.

2. **Time evolution**: The Hamiltonian $H = \mathbb{1}_4$, which is a 4×4 identity matrix, is defined. The definition of the Hamiltonian is consistent with the assumption that there are no interactions within the DFS (a magnetic field gradient does cause the state to evolve, but does not change the state fidelity with any given maximally entangled state). The Lindblad operator $L = \sqrt{\gamma_{DS}}\,|D\rangle\langle S|$ is defined by the total scattering rate $\gamma_{DS} = 1/2\tau_D$, with $\tau_D = 1.168(1)\,\text{s}$ [43] of the $3^2D_{5/2}$ manifold. The time evolved states $\rho_{\text{sim}}(T)$ are computed up to $1\,\text{s}$ using the *mesolve* module of the Python package *QuTiP*. Further details on this approach were already presented in Section 5.1.2.

3. **Fidelity calculation**: The state fidelity F_{sim} of the time evolved states $\rho_{\text{sim}}(T)$ is calculated with the ideal state $|\psi^+\rangle\langle\psi^+|$, according to Equation 2.14.
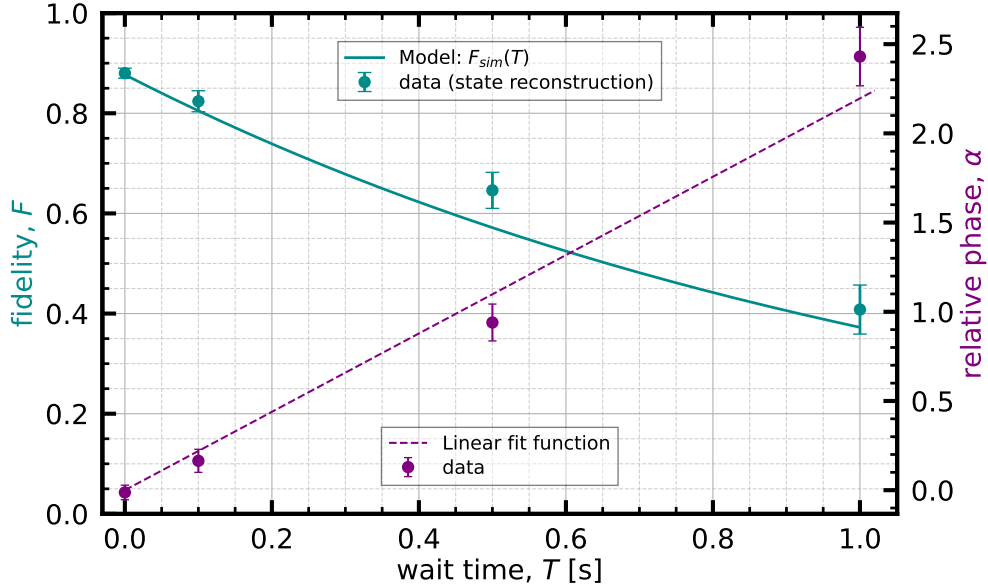

Figure 6.9.: Fidelity decay and relative phase of the Bell state given in Equation 6.11, observed in the experiment using the sequence presented in Figure 6.6 as a function of wait time T. Cyan circles with error bars show fidelity data. The cyan line shows a model described in the main text. The data point at $T = 0.5\,\text{s}$ wait time is in agreement with the model in a 2σ-interval. The relative phase data is shown as purple circles with error bars. A linear fit function is statistically consistent with the data. Errors are attributed to fidelities and phases by Monte Carlo simulation of the data.

The only free parameters in the simulation to model the state fidelity are the initial density matrix, which is obtained experimentally from QST, and the lifetime of the $3^2D_{5/2}$ manifold. No further calibration parameters are required. In Figure 6.9 the cyan line indicates the simulated fidelity F_{sim} predicted by the model as a function of wait time T. The model is statistically consistent with the data. The result (agreement of the data and the model) confirms that the lifetime of the experimentally prepared Bell state $|\psi^+\rangle$ is constrained by the lifetime of the $3^2D_{5/2}$ manifold. Therefore, the state is insensitive against collective dephasing upon the two-ion string and indeed serves as one of the basis states to span a DFS.

In Figure 6.9 the purple data points show the relative phase α. The phase is extracted from the coherences of the density matrices and errors are assigned from Monte Carlo simulation of the data[4]. The dashed purple line shows a linear fit (errors are included) to the data:

$$\alpha(T) = \frac{\Delta E}{\hbar} T, \tag{6.12}$$

where the slope of the fit function $\Delta E/\hbar$ is a free parameter that has been determined to be $2.2(2)\,\text{Hz}$. The linear model is statistically consistent with the data. The difference of the magnetic field between the ions in a two-ion string for an axial confinement of $\omega_z = 2\pi \times 1\,\text{MHz}$ and an ion separation of $5.74(4)\,\mu\text{m}$ was measured in a separate experiment to be $25(1)\,\mu\text{G}$, which corresponds to an energy difference of $\Delta E = h \times 70(3)\,\text{Hz}$ of the $|4^2S_{1/2}, m_j = -1/2\rangle$ to $|3^2D_{5/2}, m_j = -5/2\rangle$ transition [81] of the two ion-qubits. The corresponding magnetic field gradient across the two-ion string is $4.4(2)\,\text{G/m}$. The magnetic field gradient leads to a full 2π rotation of the state $|\psi^+\rangle$ every $14.3(6)\,\text{ms}$. We can use the energy difference $\Delta E = h \times 70(3)\,\text{Hz}$ to predict the relative phase α of the state $|\psi^+\rangle$ as a function of time

$$\alpha(T) = (2\pi \cdot \Delta E \cdot T) \mod 2\pi. \tag{6.13}$$

The calculation of the relative phase $\alpha(T)$ for the values of T used in the experiment results in a relative phase that is an integer multiple of 2π for all values. The wait times $T = \{0, 0.1, 0.5, 1\}\,\text{s}$ used in the experiment coincidentally align with the periodicity of the relative phase of $14.3(6)\,\text{ms}$, which was determined from the magnetic field gradient measured in the separate experiment. Hence, for the data that we took in the experiment, a relative phase $\alpha(T) = 0$ is expected for $T = \{0, 0.1, 0.5, 1\}\,\text{s}$. The data in Figure 6.9 is not statistically consistent with a relative phase of zero. Instead, the data shows a phase that increases linearly in time. However, the energy difference of $70\,\text{Hz}$ that is used in Equation 6.13 to calculate the relative phase, has an uncertainty of $3\,\text{Hz}$. The uncertainty of the energy difference ΔE yields a predicted relative phase uncertainty that increases in time, particularly for multiple 2π rotations of the state. It was not possible to determine the energy difference from a fit to the data shown in Figure 6.9 because the data is heavily under-sampled in time and full rotations of the state cannot be identified.

---

[4]The Gaussian phase distribution for each data set is approximately symmetrical around the phase value indicated in the figure.

6.4.2. Encoding the decoherence-free subspace in the ground state manifold

The lifetime of the Bell state $|\psi^+\rangle$ can be significantly increased by encoding the decoherence-free subspace in the ground state manifold, such that

$$|\psi_{SS'}^+\rangle = \frac{1}{\sqrt{2}}(|SS'\rangle + |S'S\rangle), \tag{6.14}$$

where $|S\rangle = |4^2S_{1/2}, m_j = +1/2\rangle$ and $|S'\rangle = |4^2S_{1/2}, m_j = -1/2\rangle$. The lifetime of $|\psi_{SS'}^+\rangle$ is not limited by decoherence due to spontaneous decay. To prove that the lifetime of the state $|\psi_{SS'}^+\rangle$ is increased compared to $|\psi^+\rangle$ (Equation 6.9), the same experiment as in Section 6.4.1 is conducted but with mapping the state $|\psi^+\rangle$ to the ground state manifold $|\psi_{SS'}^+\rangle$ before the wait time. For the mapping, three global rotations at 729 nm are used. The three pulses are indicated in the Figure 6.10. First, the population of $|D\rangle = |3^2D_{5/2}, m_j = -5/2\rangle$ is transferred to $|4^2S_{1/2}, m_j = -1/2\rangle$ by a 729 nm pulse. Then the population from $|4^2S_{1/2}, m_j = -1/2\rangle$ is transferred via $|3^2D_{5/2}, m_j = -3/2\rangle$ to $|4^2S_{1/2}, m_j = +1/2\rangle$. The operation of mapping to the ground state manifold is further defined as

$$R_{SS'} = R_3(\pi, 0)_{S+1/2}^{D-3/2} R_2(\pi, 0)_{D-3/2}^{S-1/2} R_1(\pi, 0)_{S-1/2}^{D-5/2}. \tag{6.15}$$

The state fidelity F is calculated according to Equation 6.11 with $|\psi^\alpha\rangle$ encoded in the ground state manifold, where the phase α is a free parameter that is optimised. The fidelity after $T = 1\,$s wait time for encoding the DFS in the ground state manifold is

$$F = 0.84(4). \tag{6.16}$$

Recall that the fidelity for zero wait time ($T = 0\,$s) for encoding the DFS in the logical qubit states $|S\rangle$ and $|D\rangle$ is $F = 0.88(1)$, as shown in Figure 6.7. There is no significant difference between the two values, indicating that there is no significant source of decoherence affecting the Bell state $|\psi_{SS'}^+\rangle$ within 1 s. As a result, the encoding in the ground state manifold offers the potential of providing a qubit memory with much longer lifetime than the one in the previous section.
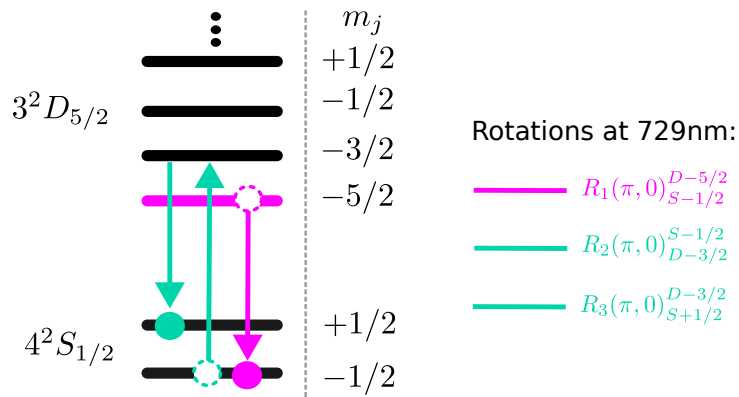

Figure 6.10.: Zeeman states of the ground state $4^2S_{1/2}$ and the exited state $3^2D_{5/2}$ manifold. Population in $|3^2D_{5/2}, m_j = -5/2\rangle$ is transferred to $|4^2S_{1/2}, m_j = -1/2\rangle$ by a rotation R_1 (pink arrow). Population in $|4^2S_{1/2}, m_j = -1/2\rangle$ is transferred via $|3^2D_{5/2}, m_j = -3/2\rangle$ to $|4^2S_{1/2}, m_j = +1/2\rangle$ by the two rotations R_2 and R_3 (cyan arrows).

6.5. Storing and retrieving a single-qubit state from a decoherence-free subspace

As an outlook, the DFS could be used in future experiments to store ion-photon entanglement. In particular, the state of a single-ion that is entangled with a photon after a bichromatic cavity-mediated Raman process could be protected from decoherence using a co-trapped ion and the CNOT gate to encode the ion-qubit state (after entangled with an emitted photon) in the DFS of the two-ion string. By applying the CNOT gate for a second time after a variable wait time, the qubit state could be retrieved from the DFS on demand, making it available for further quantum information processing. The experiment presented in this section focuses on characterising the process of storing an arbitrary single-qubit in a DFS spanned by the entangled basis states $|\psi^\pm\rangle$ (Equation 2.9 and 2.10) encoded in the ground state manifold of the ions. The process of mapping in (storing) and out (retrieving) of the DFS is realised by applying two sequential CNOT gates to an initial state with a wait time in between. In this section, the process of storing and retrieving is fully characterised by QPT yielding the process fidelity F_P.

6.5.1. Experimental details

The experimental sequence is presented in Figure 6.11. To perform QPT of the control qubit, we feed in four linearly independent input states for the control qubit to the sequence:

$$\rho = \{|S\rangle\langle S|, |D\rangle\langle D|, |+\rangle\langle +|, |+i\rangle\langle +i|\}. \tag{6.17}$$

The state of the target qubit is always $|D\rangle$ to map to the DFS spanned by $|\psi^\pm\rangle$ with the CNOT gate. The mapping to the DFS can be understood by considering the CNOT gate operation on an arbitrary single-qubit state $\alpha|S\rangle + \beta|D\rangle$, where $\alpha, \beta \in \mathbb{C}$, as control qubit, and the target qubit in $|D\rangle$:

$$U_{\mathrm{CNOT}}\left((\alpha|S\rangle + \beta|D\rangle) \otimes |D\rangle\right) \Rightarrow \alpha|SD\rangle + \beta|DS\rangle, \tag{6.18}$$

where U_{CNOT} is defined in Equation 2.22. After the first CNOT gate in the sequence shown in Figure 6.11, the prepared state is mapped to the ground state manifold by three global 729 nm laser pulses $R_{SS'}$ that are defined in Equation 6.15. After a wait time T, the mapping to the ground state manifold is reversed by $R_{SS'}^{-1}$. Next, a second CNOT gate is applied. Ideally, the second CNOT gate restores the initial states of control and target qubit such that $\rho = \rho'$ in Figure 6.11. The data is post-selected to project out the target qubit into the state $|D\rangle$. This post-selection means that all data for which the target qubit is not in $|D\rangle$ after the complete process in Figure 6.11 is not taken into account to reconstruct the single-qubit process matrix of storing and retrieving the control qubit from the DFS. The post-selection method allows for the removal of state preparation errors and any errors that change the state of the target qubit during the sequence. The process matrix χ_{exp} is calculated from the data obtained in the projected subspace of the control qubit. The entire experiment is repeated for the wait times $T = 0\,\mathrm{s}$ and $T = 500\,\mathrm{ms}$.
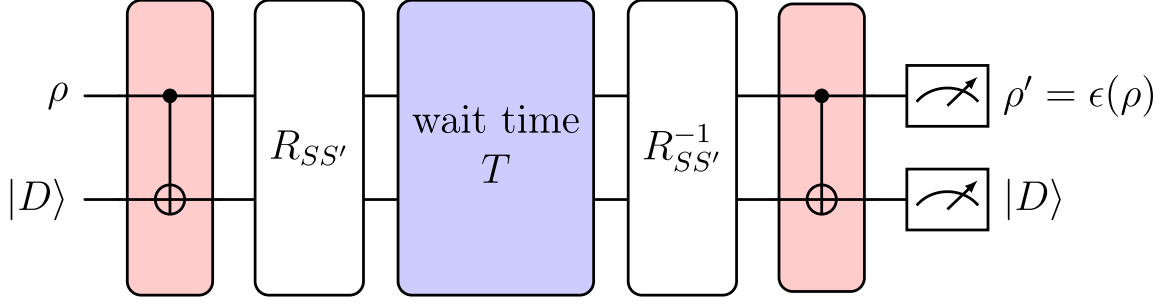
Figure 6.11.: Experimental sequence to store and retrieve a single-qubit state from a DFS spanned by entangled states. Two input states ρ (control qubit) and $|D\rangle$ (target qubit) are fed to a CNOT gate. The prepared state is mapped to the ground state manifold by applying the rotation $R_{SS'}$ defined in Equation 6.15. After the wait time T the mapping to the ground state manifold is reversed by $R_{SS'}^{-1}$. A second CNOT gate is applied. The output state is measured.

6.5.2. Result: Process tomography of encoding and retrieval

The process fidelity is now calculated with the ideal. In order to define the process fidelity reasonably, it must be taken into account that during the wait time, the prepared state acquires a relative phase due to the magnetic field gradient across the two-ion string in our ion trap [81], which was described in Section 6.4.1. As a result, when implemented in the lab, the process $\epsilon(\rho)$ of storing and retrieving the control qubit shown in Figure 6.11 is expected to be equal to a unitary rotation around the z-axis of the Bloch sphere

$$R_z(\theta) = e^{-i\frac{\theta}{2}\sigma_z}, \tag{6.19}$$

where θ is the rotation angle. The process fidelity F_p is therefore calculated with the expected process matrix $\chi_z(\theta)$ for the process of a unitary z-rotation of angle θ. The rotation angle is a free parameter, i.e. the process fidelity is determined by optimising θ in order to maximise F_p:

$$F_p = \max_\theta \big(\mathrm{tr}(\chi_{\exp}\chi_z(\theta))\big). \tag{6.20}$$

The rotation angle can also be calibrated from the magnetic field gradient in the trap. However, this calculation was not performed as part of this study. Figure 6.12 shows the process matrix for zero wait time ($T = 0\,\mathrm{s}$) yielding a process fidelity of $F_P = 0.92(2)$ with the ideal process matrix that is shown in Figure 2.3. Figure 6.13 shows the process matrix for a wait time of $T = 500\,\mathrm{ms}$ with a process fidelity of $F_p = 0.94(6)$. The process fidelity is calculated with a target process that is equal to a z-rotation by an angle $\theta = 1.6 \times \pi$. The ideal process matrix is not shown. No statistically significant difference between the process fidelity for no wait time and 500 ms wait time is obtained. The results show that storing a single-qubit state for 500 ms[5] in a decoherence-free subspace spanned by the basis states $|\psi^\pm\rangle$ and then retrieving the state is possible without any significant loss of coherence.

---

[5]Longer wait times were not investigated in the experiments due to limitations of the experimental control software.
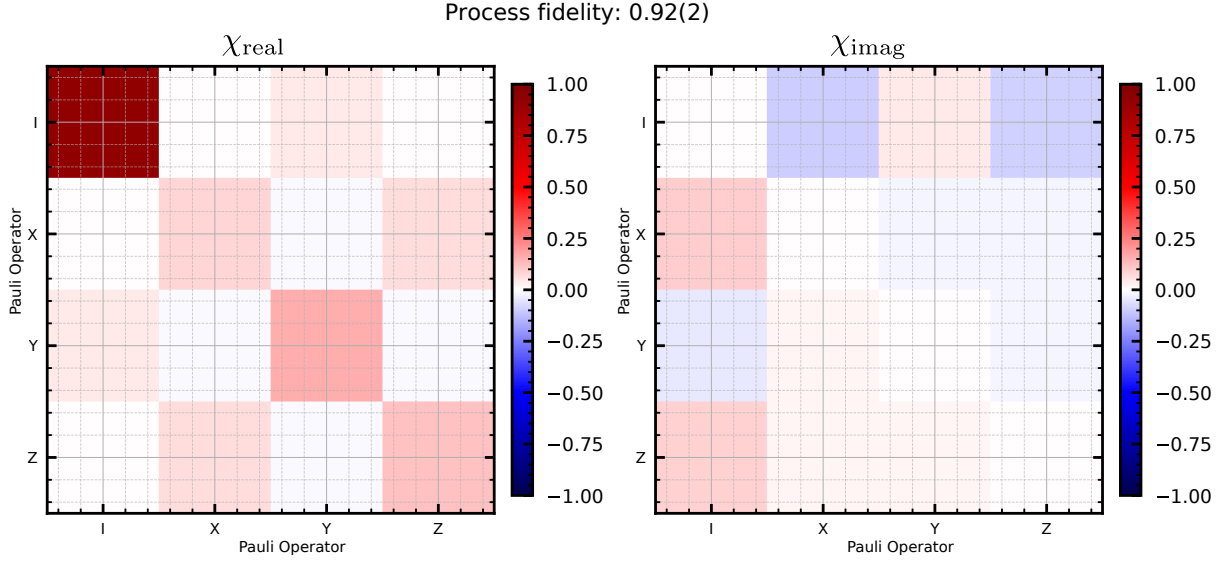
Process fidelity: 0.92(2)

Figure 6.12.: Process matrix in the Pauli operator basis for the process of storing and retrieving the control qubit in the sequence shown Figure 6.11 for zero wait time ($T = 0\,\mathrm{s}$). The real parts are shown on the left, the imaginary parts on the right. Details on the calculation of the process matrix are given in Section 6.5.1. The ideal process matrix, which is the identity operation, is shown in Figure 2.3.
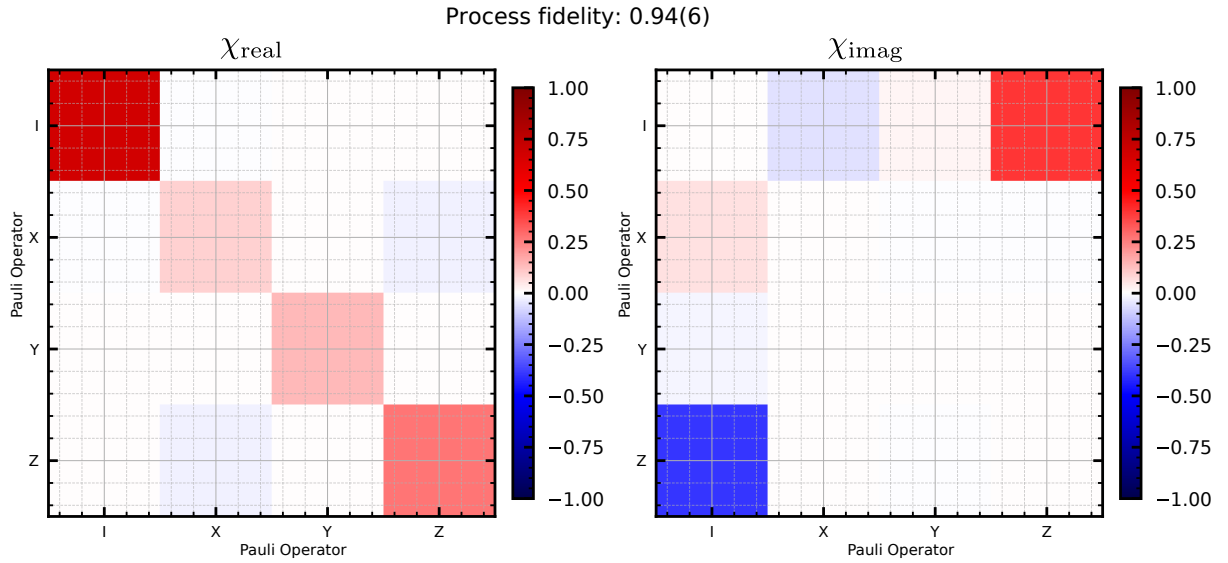
Process fidelity: 0.94(6)

Figure 6.13.: Process matrix from the same experiment as in the figure above with a wait time of $T = 500\,\mathrm{ms}$. The shown process has a process fidelity of 0.94(6) with a unitary process equal to a z-rotation with angle $\theta = 1.6 \times \pi$. Real parts are shown on the left, imaginary parts right. The ZI- and IZ-elements of the imaginary parts arise from the z-rotation. The ideal process matrix is not shown.

7. Conclusion and outlook

The following two goals were pursued in this master's thesis: first, the completion of a universal gate set, and second, the use of the universal gate set to implement and fully characterise a decoherence-free quantum memory. While the first goal enables universal quantum processing at the local trapped-ion quantum network node, the second goal is a step towards a long-lived quantum memory for storing ion-photon entanglement for several seconds and therefore to generate and store entanglement between remote locations. Both goals are essential requirements for a quantum network.

To achieve the first goal of this thesis, an optical setup was built, which is presented in Chapter 4. The setup uses two acousto-optic modulators to detune laser light at 393 nm by -2.6 GHz. The light signal is superimposed on the existing addressing beam path that Marco Canteri [19] set up as part of his master's thesis to address individual ions within a multi-ion string. The detuning Δ of -2.6 GHz is sufficiently large ($\Delta \gg \Omega$) with respect to the Rabi frequency Ω of the $4^2S_{1/2}$ to $4^2P_{3/2}$ transition used in the experiment, such that when the detuned light is applied to an ion-string, the AC Stark effect is dominant. The availability of far detuned 393 nm laser light to address single-ions with an ion string enables the implementation of single-ion focussed phase rotations via the AC Stark effect. Together with the existing capability of global qubit rotations and an MS gate at 729 nm, introduced in Chapter 3, the single-qubit phase gates form a universal gate set in our experimental setup.

Chapter 5 proves that far detuned 393 nm laser light, generated in the newly established optical setup, can be used to implement single-qubit gates. As a first test, AC Stark flops were measured on a single-ion within a four-ion string. The observed damping rate of the AC Stark flops can be explained by a model that includes spontaneous scattering, determined by the finite detuning of the AC Stark pulses and the specific laser geometry in the trapped-ion quantum network, intensity fluctuations of AC Stark pulses at 393 nm, and phase fluctuations of the 729 nm laser. After demonstrating a thorough understanding of the observed AC Stark flops data, it was shown that a single-qubit z-flip can be achieved with a fidelity of 0.975(10) for a detuning of -2.7 GHz. The z-flip is indirectly measured by embedding a 180° phase rotation of an approximately equal superposition of the qubit states in a Ramsey experiment, and therefore appears in the data as a single-qubit bit-flip. The studies in Chapter 5 identify and quantify the currently limiting factors in the quality of the single-qubit phase gates.

In the final results, which are presented in Chapter 6, the work towards a long-lived quantum memory is presented. As a first step towards the realisation of a decoherence-free quantum memory, formed by entangled states of two co-trapped ions, a CNOT gate was implemented and characterised by quantum process tomography, yielding an average gate fidelity of 88(2) %. In the next step, the entangled state $1/\sqrt{2}(|SD\rangle + |DS\rangle)$ was prepared using the CNOT gate and reconstructed by quantum state tomography after various wait

times. It was observed that the state fidelity decayed from 88(1)% for no wait time to 41(4)% for 1 s wait time. By comparing the data of the state fidelity decay to a model, it was demonstrated that the decoherence of the state can be explained by the finite lifetime of the metastable $3^2 D_{5/2}$ qubit-state. The lifetime of the Bell state was then significantly enhanced by mapping it immediately after the preparation to the ground state manifold $1/\sqrt{2}(|SS'\rangle + |S'S\rangle)$, resulting in a state fidelity of 84(4)% after 1 s. Based on this knowledge, a final experiment was conducted to fully characterise a decoherence-free quantum memory for a storage time of 500 ms. The process of storing for 500 ms and retrieving a single-qubit state from the decoherence-free quantum memory yields a process fidelity of 94(6)% with the expected unitary. This last experiment represents a promising approach for storing ion-photon entanglement for 500 ms or longer in future experiments.

Thus far, this work has demonstrated the storage of a single ion-qubit in a decoherence-free quantum memory. An obvious extension of this approach is to use the memory to store ion-photon entanglement, which is a step towards enhancing the storage time of remote entanglement. For that, the control qubit in the sequence shown in Figure 6.11 would first be entangled with a photon by driving a cavity-mediated Raman transition to generate ion-photon entanglement. The state of the ion is then protected from decoherence in the memory while the photon travels a distance. The ultimate aim of the upcoming experiments is to store ion-photon entanglement for several tens of seconds in order to establish entanglement over a distance of 800 km by employing quantum repeaters [66].

Bibliography

[1] C. Monroe and J. Kim, "Scaling the ion trap quantum processor," *Science*, vol. 339, no. 6124, pp. 1164–1169, 2013.

[2] S. Pirandola, U. L. Andersen, L. Banchi, M. Berta, D. Bunandar, R. Colbeck, D. Englund, T. Gehring, C. Lupo, C. Ottaviani, *et al.*, "Advances in quantum cryptography," *Advances in optics and photonics*, vol. 12, no. 4, pp. 1012–1236, 2020.

[3] J. F. Smith III, "Enhanced sensing and communication via quantum networks," in *Radar Sensor Technology XXI*, vol. 10188, pp. 188–203, 2017.

[4] H. J. Kimble, "The quantum internet," *Nature*, vol. 453, no. 7198, pp. 1023–1030, 2008.

[5] D. P. DiVincenzo, "Two-bit gates are universal for quantum computation," *Physical Review A*, vol. 51, no. 2, p. 1015, 1995.

[6] M. Ruf, N. H. Wan, H. Choi, D. Englund, and R. Hanson, "Quantum networks based on color centers in diamond," *Journal of Applied Physics*, vol. 130, no. 7, 2021.

[7] J. P. Covey, H. Weinfurter, and H. Bernien, "Quantum networks with neutral atom processing nodes," *npj Quantum Information*, vol. 9, no. 1, p. 90, 2023.

[8] Y. Wang, M. Um, J. Zhang, S. An, M. Lyu, J.-N. Zhang, L.-M. Duan, D. Yum, and K. Kim, "Single-qubit quantum memory exceeding ten-minute coherence time," *Nature Photonics*, vol. 11, no. 10, pp. 646–650, 2017.

[9] C. D. Bruzewicz, J. Chiaverini, R. McConnell, and J. M. Sage, "Trapped-ion quantum computing: Progress and challenges," *Applied Physics Reviews*, vol. 6, no. 2, 2019.

[10] N. Friis, O. Marty, C. Maier, C. Hempel, M. Holzäpfel, P. Jurcevic, M. B. Plenio, M. Huber, C. F. Roos, R. Blatt, *et al.*, "Observation of entangled states of a fully controlled 20-qubit system," *Physical Review X*, vol. 8, no. 2, p. 021012, 2018.

[11] M. Meraner, A. Mazloom, V. Krutyanskiy, V. Krcmarsky, J. Schupp, D. Fioretto, P. Sekatski, T. Northup, N. Sangouard, and B. Lanyon, "Indistinguishable photons from a trapped-ion quantum network node," *Physical Review A*, vol. 102, no. 5, p. 052614, 2020.

[12] J. Schupp, V. Krcmarsky, V. Krutyanskiy, M. Meraner, T. Northup, and B. Lanyon, "Interface between trapped-ion qubits and traveling photons with close-to-optimal efficiency," *PRX quantum*, vol. 2, no. 2, p. 020331, 2021.

[13] V. Krutyanskiy, M. Meraner, J. Schupp, V. Krcmarsky, H. Hainzer, and B. P. Lanyon, "Light-matter entanglement over 50 km of optical fibre," *npj Quantum Information*, vol. 5, no. 1, p. 72, 2019.

[14] D. L. Moehring, P. Maunz, S. Olmschenk, K. C. Younge, D. N. Matsukevich, L.-M. Duan, and C. Monroe, "Entanglement of single-atom quantum bits at a distance," *Nature*, vol. 449, no. 7158, pp. 68–71, 2007.

[15] V. Krutyanskiy, M. Galli, V. Krcmarsky, S. Baier, D. Fioretto, Y. Pu, A. Mazloom, P. Sekatski, M. Canteri, M. Teller, *et al.*, "Entanglement of trapped-ion qubits separated by 230 meters," *Physical Review Letters*, vol. 130, no. 5, p. 050803, 2023.

[16] T. Ruster, C. T. Schmiegelow, H. Kaufmann, C. Warschburger, F. Schmidt-Kaler, and U. G. Poschinger, "A long-lived Zeeman trapped-ion qubit," *Applied Physics B*, vol. 122, no. 10, p. 254, 2016.

[17] D. Kielpinski, V. Meyer, M. Rowe, C. A. Sackett, W. M. Itano, C. Monroe, and D. J. Wineland, "A decoherence-free quantum memory using trapped ions," *Science*, vol. 291, no. 5506, pp. 1013–1015, 2001.

[18] M. A. Nielsen and I. L. Chuang, "Quantum computation and quantum information," *Phys. Today*, vol. 54, no. 2, p. 60, 2001.

[19] M. Canteri, "Single-atom-focused laser for photon generation and qubit control," Master's thesis, University of Innsbruck, 2020.

[20] A. Stute, B. Casabone, P. Schindler, T. Monz, P. Schmidt, B. Brandstätter, T. Northup, and R. Blatt, "Tunable ion–photon entanglement in an optical cavity," *Nature*, vol. 485, no. 7399, pp. 482–485, 2012.

[21] C. Hempel, *Digital quantum simulation, Schrödinger cat state spectroscopy and setting up a linear ion trap.* PhD thesis, University of Innsbruck, 2014.

[22] N. Gisin and H. Bechmann-Pasquinucci, "Bell inequality, Bell states and maximally entangled states for n qubits," *Physics Letters A*, vol. 246, no. 1-2, pp. 1–6, 1998.

[23] U. Fano, "Description of states in quantum mechanics by density matrix and operator techniques," *Reviews of modern physics*, vol. 29, no. 1, p. 74, 1957.

[24] R. Jozsa, "Fidelity for mixed quantum states," *Journal of modern optics*, vol. 41, no. 12, pp. 2315–2323, 1994.

[25] M. Enríquez, I. Wintrowicz, and K. Życzkowski, "Maximally entangled multipartite states: a brief survey," in *Journal of Physics: Conference Series*, vol. 698, p. 012003, IOP Publishing, 2016.

[26] B. Palais, R. Palais, and S. Rodi, "A disorienting look at Euler's theorem on the axis of a rotation," *The American Mathematical Monthly*, vol. 116, no. 10, pp. 892–909, 2009.

[27] A. Sørensen and K. Mølmer, "Ion trap quantum computer with bichromatic light," *Fortschritte der Physik: Progress of Physics*, vol. 48, no. 9-11, pp. 811–821, 2000.

[28] O. Gamel, "Entangled bloch spheres: Bloch matrix and two-qubit state space," *Physical Review A*, vol. 93, no. 6, p. 062320, 2016.

[29] W. K. Wootters, "Entanglement of formation and concurrence.," *Quantum Inf. Comput.*, vol. 1, no. 1, pp. 27–44, 2001.

[30] J. Yuen-Zhou, J. J. Krich, I. Kassal, A. S. Johnson, and A. Aspuru-Guzik, "The process matrix and how to determine it: quantum process tomography," *Ultrafast Spectroscopy*, pp. 2053–2563, 2014.

[31] S. T. Merkel, J. M. Gambetta, J. A. Smolin, S. Poletto, A. D. Córcoles, B. R. Johnson, C. A. Ryan, and M. Steffen, "Self-consistent quantum process tomography," *Physical Review A*, vol. 87, no. 6, p. 062119, 2013.

[32] M. Branderhorst, J. Nunn, I. Walmsley, and R. Kosut, "Simplified quantum process tomography," *New Journal of Physics*, vol. 11, no. 11, p. 115010, 2009.

[33] M. Mohseni, A. T. Rezakhani, and D. A. Lidar, "Quantum-process tomography: Resource analysis of different strategies," *Physical Review A*, vol. 77, no. 3, p. 032322, 2008.

[34] A. Anis and A. Lvovsky, "Maximum-likelihood coherent-state quantum process tomography," *New Journal of Physics*, vol. 14, no. 10, p. 105021, 2012.

[35] M. A. Nielsen, "A simple formula for the average gate fidelity of a quantum dynamical operation," *Physics Letters A*, vol. 303, no. 4, pp. 249–252, 2002.

[36] R. Grimm, M. Weidemüller, and Y. B. Ovchinnikov, "Optical dipole traps for neutral atoms," in *Advances in atomic, molecular, and optical physics*, vol. 42, pp. 95–170, Elsevier, 2000.

[37] H. Häffner, C. F. Roos, and R. Blatt, "Quantum computing with trapped ions," *Physics reports*, vol. 469, no. 4, pp. 155–203, 2008.

[38] H. Häffner, F. Schmidt-Kaler, W. Hänsel, C. Roos, T. Körber, M. Chwalla, M. Riebe, J. Benhelm, U. Rapol, C. Becher, *et al.*, "Robust entanglement," *Applied Physics B*, vol. 81, pp. 151–153, 2005.

[39] T. Monz, K. Kim, A. Villar, P. Schindler, M. Chwalla, M. Riebe, C. F. Roos, H. Häffner, W. Hänsel, M. Hennrich, *et al.*, "Realization of universal ion-trap quantum computation with decoherence-free qubits," *Physical review letters*, vol. 103, no. 20, p. 200503, 2009.

[40] D. A. Lidar, "Review of decoherence-free subspaces, noiseless subsystems, and dynamical decoupling," *Quantum information and computation for chemistry*, pp. 295–354, 2014.

[41] J. Schupp, *Interface between trapped-ion qubits and travelling photons with close-to-optimal efficiency.* PhD thesis, University of Innsbruck, 2022.

[42] J. Jin and D. Church, "Precision lifetimes for the ^{40}Ca$^+$ $4p^2P$ levels: experiment challenges theory at the 1% level," *Physical review letters*, vol. 70, no. 21, p. 3213, 1993.

[43] P. Barton, C. Donald, D. Lucas, D. Stevens, A. Steane, and D. Stacey, "Measurement of the lifetime of the $3d^2D_{5/2}$ state in ^{40}Ca$^+$," *Physical Review A*, vol. 62, no. 3, 2000.

[44] *NIST Atomic Spectra Database.* `https://physics.nist.gov/PhysRefData/ASD/lines_form.html`.

[45] A. J. Daley, M. M. Boyd, J. Ye, and P. Zoller, "Quantum computing with alkaline-earth-metal atoms," *Physical review letters*, vol. 101, no. 17, p. 170504, 2008.

[46] N. Kjærgaard, L. Hornekær, A. Thommesen, Z. Videsen, and M. Drewsen, "Isotope selective loading of an ion trap using resonance-enhanced two-photon ionization," *Applied Physics B*, vol. 71, pp. 207–210, 2000.

[47] C. Schuck, M. Almendros, F. Rohde, M. Hennrich, and J. Eschner, "Two-color photoionization of calcium using SHG and LED light," *Applied Physics B*, vol. 100, pp. 765–771, 2010.

[48] D. Leibfried, R. Blatt, C. Monroe, and D. Wineland, "Quantum dynamics of single trapped ions," *Reviews of Modern Physics*, vol. 75, no. 1, p. 281, 2003.

[49] D. J. Wineland and W. M. Itano, "Laser cooling of atoms," *Physical Review A*, vol. 20, no. 4, p. 1521, 1979.

[50] C. Roos, T. Zeiger, H. Rohde, H. Nägerl, J. Eschner, D. Leibfried, F. Schmidt-Kaler, and R. Blatt, "Quantum state engineering on an optical transition and decoherence in a paul trap," *Physical Review Letters*, vol. 83, no. 23, p. 4713, 1999.

[51] J. Eschner, G. Morigi, F. Schmidt-Kaler, and R. Blatt, "Laser cooling of trapped ions," *JOSA B*, vol. 20, no. 5, pp. 1003–1015, 2003.

[52] H. Hainzer, "Laser locking for trapped-ion quantum networks," Master's thesis, University of Innsbruck, 2018.

[53] C. F. Roos, *Controlling the quantum state of trapped ions.* PhD thesis, University of Innsbruck, 2000.

[54] E. W. Weber, "Optical pumping of ions," *Physics Reports*, vol. 32, no. 3, pp. 123–167, 1977.

[55] M. Ramm, T. Pruttivarasin, M. Kokish, I. Talukdar, and H. Häffner, "Precision measurement method for branching fractions of excited $P_{1/2}$ states applied to ^{40}Ca$^+$," *Physical review letters*, vol. 111, no. 2, p. 023004, 2013.

[56] D. Stevens, J. Brochard, and A. Steane, "Simple experimental methods for trapped-ion quantum processors," *Physical Review A*, vol. 58, no. 4, p. 2750, 1998.

Bibliography

[57] A. Myerson, D. Szwer, S. Webster, D. Allcock, M. Curtis, G. Imreh, J. Sherman, D. Stacey, A. Steane, and D. Lucas, "High-fidelity readout of trapped-ion qubits," *Physical Review Letters*, vol. 100, no. 20, p. 200502, 2008.

[58] W. M. Itano, J. C. Bergquist, J. J. Bollinger, J. Gilligan, D. Heinzen, F. Moore, M. Raizen, and D. J. Wineland, "Quantum projection noise: Population fluctuations in two-level systems," *Physical Review A*, vol. 47, no. 5, p. 3554, 1993.

[59] K. Mølmer and A. Sørensen, "Multiparticle entanglement of hot trapped ions," *Physical Review Letters*, vol. 82, no. 9, p. 1835, 1999.

[60] F. Schmidt-Kaler, H. Häffner, M. Riebe, S. Gulde, G. P. Lancaster, T. Deuschle, C. Becher, C. F. Roos, J. Eschner, and R. Blatt, "Realization of the Cirac-Zoller controlled-NOT quantum gate," *Nature*, vol. 422, no. 6930, pp. 408–411, 2003.

[61] G. Kirchmair, J. Benhelm, F. Zähringer, R. Gerritsma, C. F. Roos, and R. Blatt, "Deterministic entanglement of ions in thermal states of motion," *New Journal of Physics*, vol. 11, no. 2, p. 023002, 2009.

[62] D. J. Wineland, C. Monroe, W. M. Itano, D. Leibfried, B. E. King, and D. M. Meekhof, "Experimental issues in coherent quantum-state manipulation of trapped atomic ions," *Journal of research of the National Institute of Standards and Technology*, vol. 103, no. 3, p. 259, 1998.

[63] A. Sørensen and K. Mølmer, "Entanglement and quantum computation with ions in thermal motion," *Physical Review A*, vol. 62, no. 2, p. 022311, 2000.

[64] C. F. Roos, "Ion trap quantum gates with amplitude-modulated laser beams," *New Journal of Physics*, vol. 10, no. 1, p. 013002, 2008.

[65] J. Helgert, "Radio frequency control of a trapped-ionquantum network node," Master's thesis, University of Innsbruck, 2024.

[66] V. Krutyanskiy, M. Canteri, M. Meraner, J. Bate, V. Krcmarsky, J. Schupp, N. Sangouard, and B. Lanyon, "A telecom-wavelength quantum repeater node based on a trapped-ion processor," *arXiv preprint arXiv:2210.05418*, 2022.

[67] *Schäfter+ Kirchhoff, Fibre collimator, 60FC-M12-33.* `https://www.sukhamburg.com/`.

[68] *Photonic fibers (Model LMA-PM-10-UV): Numerical aperture 0.033, Email conversation Marco Canteri and Customer Support (NKT Photonics), 01. September 2022.*

[69] *AD9915, Data sheet.* `https://www.analog.com/media/en/technical-documentation/data-sheets/ad9915.pdf`.

[70] *Photodiode PDA36A(-EC).* `https://www.thorlabs.com/thorproduct.cfm?partnumber=PDA36A-EC`.

[71] R. Gerritsma, G. Kirchmair, F. Zähringer, J. Benhelm, R. Blatt, and C. Roos, "Precision measurement of the branching fractions of the $4p^2P_{3/2}$ decay of Ca II," *The European Physical Journal D*, vol. 50, pp. 13–19, 2008.

[72] *QuTip, Quantum Toolbox in Python.* `https://qutip.org/`.

[73] *QuTiP, mesolve.* `https://qutip.org/docs/4.0.2/modules/qutip/mesolve.html`.

[74] D. Gottesman, "An introduction to quantum error correction and fault-tolerant quantum computation," in *Quantum information science and its contributions to mathematics, Proceedings of Symposia in Applied Mathematics*, vol. 68, pp. 13–58, 2010.

[75] L. Gerster, F. Martínez-García, P. Hrmo, M. W. van Mourik, B. Wilhelm, D. Vodola, M. Müller, R. Blatt, P. Schindler, and T. Monz, "Experimental bayesian calibration of trapped-ion entangling operations," *PRX Quantum*, vol. 3, no. 2, p. 020350, 2022.

[76] F. Martínez-García, L. Gerster, D. Vodola, P. Hrmo, T. Monz, P. Schindler, and M. Müller, "Analytical and experimental study of center-line miscalibrations in Mølmer-Sørensen gates," *Physical Review A*, vol. 105, no. 3, p. 032437, 2022.

[77] A. Fedorov, L. Steffen, M. Baur, M. P. da Silva, and A. Wallraff, "Implementation of a Toffoli gate with superconducting circuits," *Nature*, vol. 481, no. 7380, pp. 170–172, 2012.

[78] *Open source library: Forest-Benchmarking.* `https://forest-benchmarking.readthedocs.io/en/latest/index.html`.

[79] G. C. Knee, E. Bolduc, J. Leach, and E. M. Gauger, "Quantum process tomography via completely positive and trace-preserving projection," *Physical Review A*, vol. 98, no. 6, p. 062336, 2018.

[80] J. L. O'Brien, G. J. Pryde, A. Gilchrist, D. F. V. James, N. K. Langford, T. C. Ralph, and A. G. White, "Quantum process tomography of a controlled-NOT gate," *Phys. Rev. Lett.*, vol. 93, p. 080502, Aug 2004. `https://link.aps.org/doi/10.1103/PhysRevLett.93.080502`.

[81] J. Bate, *Labblog post from 16.10.2023 "Gradient magnetic field cancellation".* Distributed Quantum Systems group.

[82] T. Monz, P. Schindler, J. T. Barreiro, M. Chwalla, D. Nigg, W. A. Coish, M. Harlander, W. Hänsel, M. Hennrich, and R. Blatt, "14-qubit entanglement: Creation and coherence," *Physical Review Letters*, vol. 106, no. 13, p. 130506, 2011.

A. Supplemental material: Chapter 4

A.1. Acousto-optic frequency shifters: Brimrose

AO Frequency Shifter
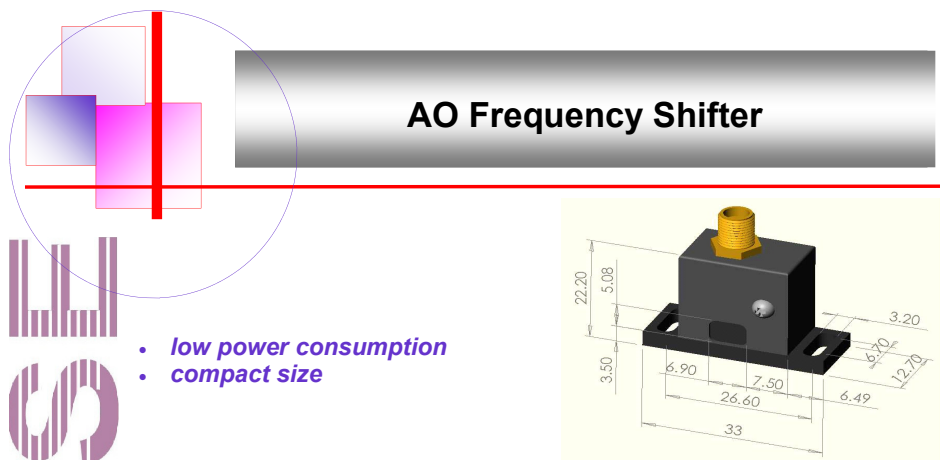
- *low power consumption*
- *compact size*

MODEL # TEF-1000-300-393
Specifications:

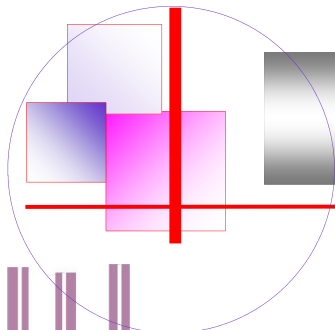|	
Wavelength of Operation	393 nm
Optical Power Density	20 W/mm^2
Carrier Frequencies*	1000 MHz
Frequency Bandwidth (3 dB)	300 MHz
Active Aperture	0.075 mm
Bragg Angle	47 mrad
Separation Angle	94 mrad
Acoustic Velocity	4.2 E+3 m/s
Maximum RF Power	1.0 W
Optical Transmission	95%
Diffraction Efficiency	~40%
Input Impedance	50 ohms
V.S.W.R.	2.1:1
Optical Polarization	linear
Case Type	air-cooled

Brimrose Corporation of America
19 Loveton Circle
Hunt Valley Loveton Center
Baltimore, Maryland 21152-9201 USA

PHONE: 410 - 472 7070
FAX: 410 - 472 7960
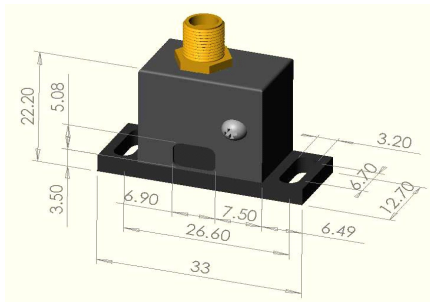EMAIL: office@brimrose.com

www.brimrose.com

V1a97

AO Frequency Shifter

- *low power consumption*
- *compact size*
- *high frequency*

MODEL # TEF-600-400-393
Specifications:

Wavelength of Operation	393 nm
Optical Input Power	45 mW max.
Carrier Frequencies*	600 MHz
Bandwidth (3 dB)	400 MHz
Active Aperture	0.075 mm
Bragg Angle	28 mrad
Separation Angle	56 mrad
Acoustic Velocity	4.2 E+3 m/s
Maximum RF Power	1.0 W
Optical Transmission	95%
Diffraction Efficiency	~40-50%
Input Impedance	50 ohms
V.S.W.R.	2.1:1
Optical Polarization	linear
Case Type	air-cooled
RF Connector	SMA

* - the required optical polarization is parallel to the sound direction (horizontal)

B. Supplemental material: Chapter 5

B.1. Calibration: Model 1

The simulation of Model 1 requires various input parameters, as described in Section 5.1.2. While the scattering rates are taken from the literature [42], certain parameters, such as the Rabi frequency Ω, are calibrated using the data from AC Stark flops from Section 5.1.1. The data in Figure 5.2 are fitted to the function:

$$P_D(\tau) = A \cdot \left(1 + \exp^{-\gamma\tau} \cos(\delta_{\mathrm{AC}}\tau - \delta_0)\right). \tag{B.1}$$

Equation B.1 is based on the theoretically expected probability, Equation 5.1, for the experiment presented in Section 5.1.1. The function contains A as a free parameter so that the amplitude of the oscillations can deviate from 1. It additionally takes into account the exponential damping of the oscillation, which is evident in the data, by including the term $\exp^{-\gamma\tau}$, where γ, the damping rate, is a free parameter. The data in Figure 5.2 show that the excitation probability P_D at time $\tau = 0$ is slightly different from zero, so the function includes another free parameter: δ_0. The frequency of the oscillation of the excitation probability $P_D(\tau)$ directly yields the AC Stark shift δ_{AC}. The Python module *curve_fit* from the package *SciPy optimize* is used for curve fitting. The fit is weighted with the errors of the data points. In order to ensure physically meaningful results, i.e. to take into account that the probability P_D must not be greater than 1, the free parameter A in Equation B.1 is given an upper limit of 0.5. The fitting parameters and the corresponding errors are listed in the table B.1.

Parameter	Value
A	0.492(2)
γ	$0.0064(2)\,\mu\mathrm{s}^{-1}$
δ_{AC}	$0.4292(3)\,\mathrm{MHz}$
δ_0	$-3.33(2)$

Table B.1.: Fit parameters.

The Rabi frequency Ω of the $|4^2S_{1/2}, m_j = -1/2\rangle$ to $|4^2P_{3/2}, m_j = -3/2\rangle$ transition, that is required as input parameter in Model 1, is calculated as

$$\Omega = \sqrt{4|\Delta|\delta_{\mathrm{AC}}} \tag{B.2}$$

where $\Delta = -2.74(1)\,\mathrm{GHz}$ and $\delta_{\mathrm{AC}} = 0.4292(3)\,\mathrm{MHz}$. The result is $\Omega = 68.6(2)\,\mathrm{MHz}$. In Figure 5.2 it can be seen that the excitation probability $P_D(\tau)$ does not start at zero as

ideally expected. Instead, there is a time offset τ_0 that is not equal to zero. To obtain Model 1 results that match the data, the time offset is calculated by solving the equation $P_D(\tau_0) = 0$. The result is $\tau_0 = -0.3\,\mu$s. The result of Model 1, when plotted together with the data, is shifted in time by an amount of τ_0.

B.2. Calibration: 729-phase fluctuations

Figure 5.3 presents the data for unaddressed ions in the experiment presented in the sequence shown in Figure 5.1 for a wait time $T = 200\,\mu$s. In Section 5.1.4 it is claimed that the data is consistent with the predictions of a model that includes phase fluctuations of the 729 nm laser. The data in Figure 5.3 is compared with a model to determine the parameters of the model that are consistent with the data. The simulation first initialises an empty list to store the results. This is followed by a main loop with a number of repetitions that equals the number of data points in Figure 5.3. Each repetition of the loop consists of the following steps:

1. A quantum state ρ_0 is initialised by applying a unitary operator $R(\pi/2, 0)$, which represents a global rotation according to Equation 3.2, to the predefined state $|S\rangle$ yielding

$$\rho_0 = \frac{1}{2}\big(\,|S\rangle\langle S| + |S\rangle\langle D| + |D\rangle\langle S| + |D\rangle\langle D|\,\big). \tag{B.3}$$

2. A hundred random phases, $\phi_{2,k}$ with $k = 0, 1, .., 100$, are generated from a Gaussian distribution with a mean $\phi = \pi$ and a standard deviation $\delta\phi = 0.094 \cdot \phi$. The sample size 100 represents the number of cycles in the experiment. The phases are stored in a list.

3. A second loop is implemented to calculated the excitation probability P_D for each step of the main loop. This inner loop iterates over the 100 generated random phases. It consists of the following steps.

   a) A global rotation $R(\pi/2, \phi_{2,k})$ is generated with a fixed rotation angle of $\theta = \pi/2$ and a sampled phase $\phi = \phi_{2,k}$ out of the predefined list of phases.

   b) The global rotation $R(\pi/2, \phi_{2,k})$ is applied to the state ρ_0 yielding the state ρ_f.

   c) The expectation value P_D of the operator $|D\rangle\langle D|$ is calculated for the state ρ_f. This ends the inner loop.

4. After the inner loop completes (for 100 random phases), the average expectation value $\overline{P_D}$ obtained for the different random phases is calculated. This value is appended to the empty list to store the results.

Figure B.1 presents the result of the simulation. The result is presented with errors bars for 100 cycles given by quantum projection noise according to Section 3.2. The average value of the excitation probability $P_D =$ is 0.021(1) with standard error which is statistically consistent with the average excitation probability of all three ions in Figure 5.3. The result is that 9.4 % phase fluctuations are consistent with the data in Figure 5.3 for a wait time $T = 200\,\mu$s between the two 729-laser pulses.
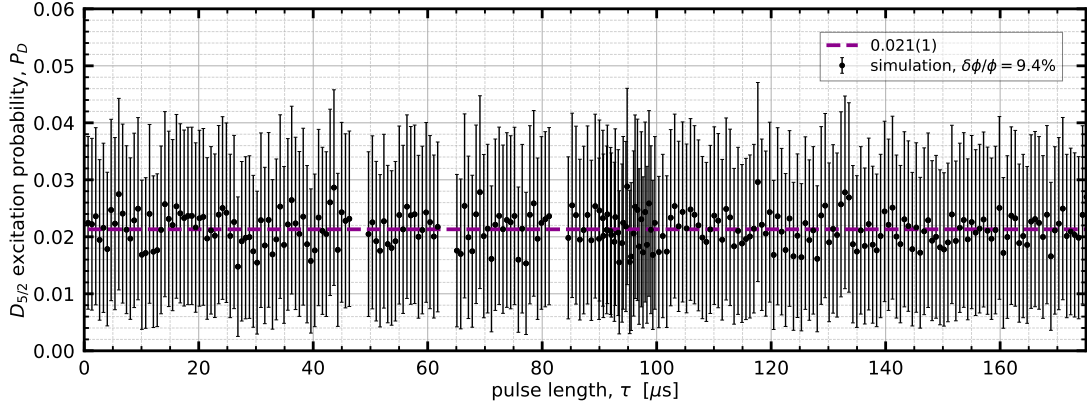
Figure B.1.: Simulation result (black dots with error bars) assuming 9.4% phase fluctuations in the $729\,\mathrm{nm}$ laser for modelling the data in Figure 5.3. The dashed purple line shows the average excitation probability. In Figure 5.3, some data points that are known to be due to melting of ion-string are not shown. These points were also removed in the simulation here, resulting in irregular distances between the points.

C. Supplemental material: Chapter 6

C.1. Quality of the MS gate

The quality of the MS gate is assessed by determining the fidelity with which the gate prepares the maximally entangled state

$$|\phi^+\rangle = \frac{1}{\sqrt{2}} = \big(|00\rangle + |11\rangle\big), \tag{C.1}$$

where $|0\rangle = |4^2S_{1/2}, m_j = -1/2\rangle$ and $|1\rangle = |3^2D_{5/2}, m_j = -5/2\rangle$. The state fidelity was estimated by measuring parity oscillations and populations of the state in Equation C.1, following the approach outlined in reference [82]. In particular, the fidelity estimate provided here pertains solely to our ability to prepare the state $|\phi^+\rangle$ using the MS gate and should not be considered a gate fidelity by definition. A precise calculation of the gate fidelity requires quantum process tomography or randomised benchmarking. In the experiment, the state $|\phi^+\rangle$ is prepared N times and the ion-qubit states are read out by electron shelving. The fluorescence signal is detected with a photo-multiplier tube (PMT). The conditional probabilities $p_{ij} = \{p_{00}, p_{11}\}$ which are the diagonal elements of the density matrix $|\phi^+\rangle \langle\phi^+|$, are calculated, where i, j are indices for the states of ion-qubit i, j. Figure C.1 shows the $|\phi^+\rangle$-populations as a function of N. The $|\phi^+\rangle$-populations are calculated as the average probability over N of finding the state in $|00\rangle$ or $|11\rangle$:

$$P = p_{00} + p_{11} = 0.954(4). \tag{C.2}$$

The coherences C of the density matrix are determined by measuring parity oscillations defined in reference [82]. The parity oscillations are presented in Figure C.2. C is given by the amplitude of the oscillations:

$$C = 0.93(1). \tag{C.3}$$

The MS gate fidelity is estimated as the weighted average of P and C, yielding
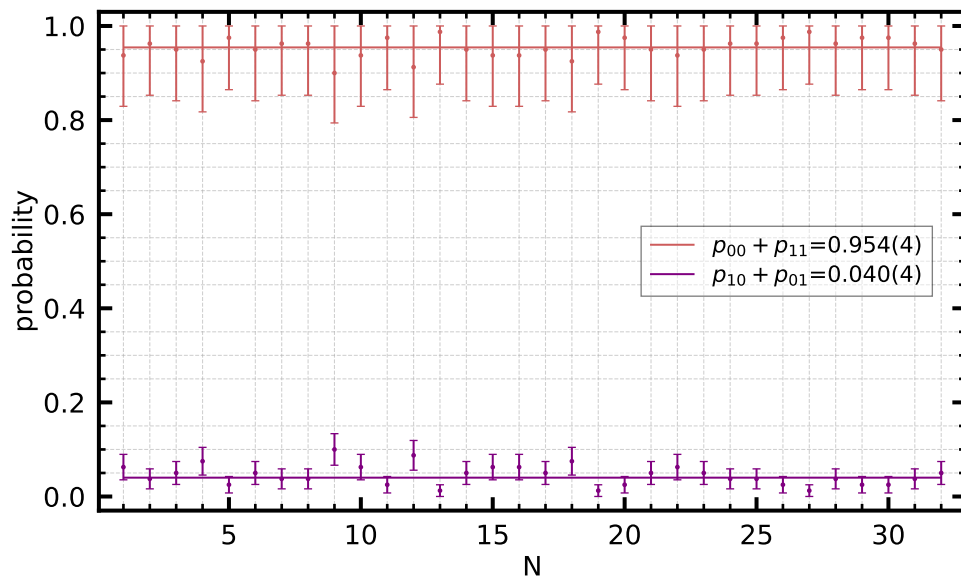
$$F = 0.947(6). \tag{C.4}$$

Figure C.1.: Populations of the state $|\phi^+\rangle$ defined in Equation C.1 that was prepared using the MS gate.
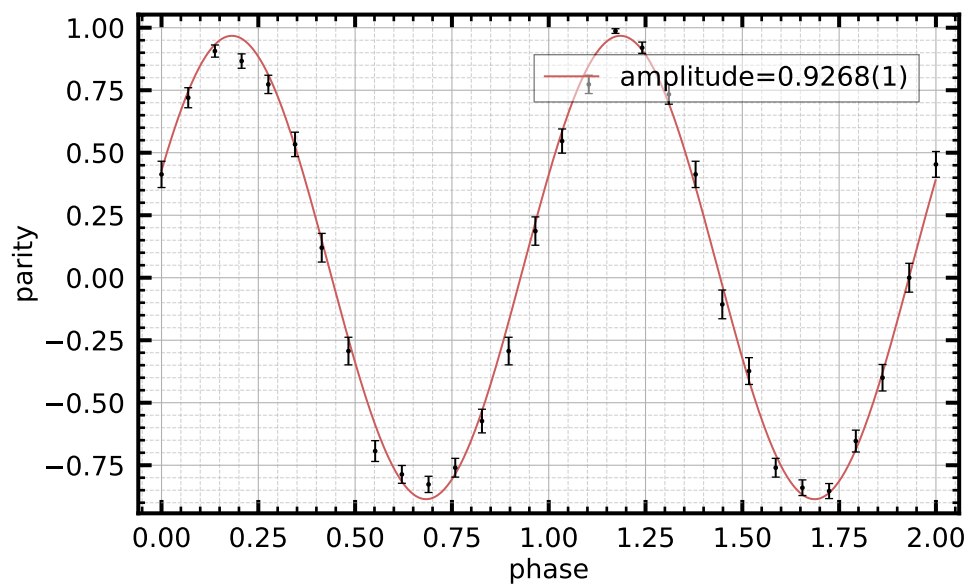

Figure C.2.: Parity oscillations defined in reference [82] of the state $|\phi^+\rangle$ that was prepared using the MS gate.